Large-scale Metal Additive Manufacturing: A Holistic Review of the State of the Art and Challenges

Thomas Lehmann☆[a], Dylan Rose☆[b], Ehsan Ranjbar[c], Morteza Ghasri-Khouzani[a], Mahdi Tavakoli[c], Hani Henein[b], Tonya Wolfe[d], Ahmed Jawad Qureshi[a,1,*]

[a] *Department of Mechanical Engineering, University of Alberta, Edmonton, AB, Canada*
[b] *Department of Chemical and Materials Engineering, University of Alberta, Edmonton, AB, Canada*
[c] *Department of Electrical and Computer Engineering, University of Alberta, Edmonton, AB, Canada*
[d] *InnoTech Alberta, Edmonton, AB, Canada*

Abstract

Additive Manufacturing (AM) has the potential to completely reshape the manufacturing space by removing the geometrical constraints of commercial manufacturing and reducing component lead time, especially for large-scale parts. Coupling robotic systems with direct energy deposition (DED) additive manufacturing techniques allow for support-free printing of parts where part sizes are scalable from sub-meter to multi-meter sizes. This paper offers a holistic review of large-scale robotic additive manufacturing, beginning with an introduction to AM, followed by the different DED techniques, the compatible materials, and their typical as-built microstructures. Next, the multitude of robotic build platforms that extend the deposition from the standard 2.5 degrees of freedom (DOF) to 6 and 8 DOF are discussed. With this context, the decomposition and slicing of the computerized model will be described, and the challenges of planning the deposition trajectory with be discussed. The different modalities to monitor and control the deposition in an attempt to meet the geometrical and performance specifications are outlined and discussed. A wide range of metals and alloys have been reported and evaluated for large-scale AM parts. These include steels, Ti, Al, Mg, Cu, Ni, Co-Cr, and W alloys. Different post-processing steps, including heat treatments, are discussed, along with their microstructures. The paper finally addresses the authors' perspective on the future of the field and the largest knowledge gaps that need to be filled before the commercial implementation of robotic AM.

Keywords: Additive manufacturing, large scale, gas metal arc welding, laser-based direct energy deposition

Highlighting legend:
Reviewer #1, Reviewer #2

1. Introduction

Additive Manufacturing (AM), also known as 3D printing, uses computer-aided design (CAD) to build objects layer by layer [1]. This contrasts a significant portion of traditional manufacturing, which uses casting, sintering, or removing unwanted material from an ingot using machining. [2]. AM is still in its infancy, but the projected possibilities will drastically change the manufacturing space. One of the proven advantages of AM compared to conventional manufacturing is the lack of shape constraints on components. This allows for complex geometries to be constructed, where conventional manufacturing would require the joining of multiple pieces to create the same part [3]. Geometrical freedom has the potential to reduce component lead time, cost (fabrication of cast not needed, lower energy consumption, material cost), material waste, energy usage, carbon footprint, and drastically reduce the need for post-processing [4].

The industrial applications of AM range from aerospace to the energy sector to healthcare. The ultimate goal is to have on-site access to this technology, eliminating the need for stockpiles of replacement parts.Although AM research is currently also conducted in the construction sector [5], the focus of this paper is on metal AM. According to ISO standard 17296-2, 7 process categories currently exist, including vat photopolymerization, material jetting, binder jetting, powder bed fusion, material extrusion, direct energy deposition, and sheet lamination [6]. A large portion of the research and commercial development of metal AM systems has been on powder bed fusion (PBF) [7, 8, 9]. In these machines, a laser is scanned over a fine layer of powder, fusing it together. The build substrate drops down according to the layer thickness, and the powder is redistributed using a roller or scraper, and the laser fuses the newly distributed powder to the previously deposited material. This

☆Thomas Lehmann and Dylan Rose contributed equally to the manuscript.
*Corresponding author
Email addresses: lehmann@ualberta.ca (Thomas Lehmann☆), drose1@ualberta.ca (Dylan Rose☆), ehsan@ualberta.ca (Ehsan Ranjbar), ghasrikh@ualberta.ca (Morteza Ghasri-Khouzani), mahdi.tavakoli@ualberta.ca (Mahdi Tavakoli), hhenein@ualberta.ca (Hani Henein), Tonya.Wolfe@innotechalberta.ca (Tonya Wolfe), ajqureshi@ualberta.ca (Ahmed Jawad Qureshi)
[1] *Address:* 10-361 Donadeo Innovation Centre for Engineering, 9211-116 Street NW, Edmonton, AB, Canada, T6G 1H9

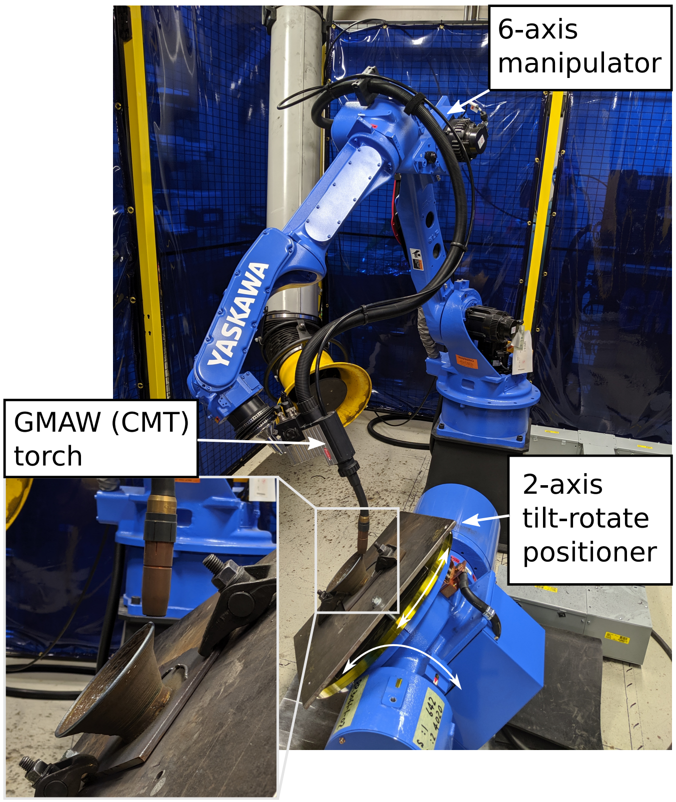

Figure 1: An example of a large-scale robotic AM fabrication platform using a wire and arc welding system for metal deposition.

process repeats until the part is complete. These platforms are intrinsically limited to 2.5 Degrees of Freedom (DOF), where each layer is printed on a 2-dimensional plane [10, 11]. A limitation of 2.5 DOF is the need for support structures on overhanging features of more than 30-40°, where 0° is perpendicular to the build plate. It should be noted that the degree of overhang before manufacturing defects begin to form is a function of the thermophysical properties of the molten material being printed [12, 13, 14, 15]. This introduces complex designing, planning, and post-processing to remove the supports, adding significant material cost due to added support material (waste material) and labour cost caused by the required removal of the support material.

There is garnering interest in expanding the DOF of AM systems to allow for the manipulation of the part in-situ.. This would eliminate the need for support structures [16, 17, 18, 19]. The increase in DOF is achieved via the integration of robotic manipulators and positioners (see Figure 1). The manipulators can then house various direct energy deposition (DED) modalities such as: gas metal arc welding (GMAW), gas tungsten arc welding (GTAW), laser-based direct energy deposition (LDED), and plasma arc transfer welding(PTAW), enabling multi-directional deposition [20, 21, 22, 23]. A depiction of this is shown in Figure 1, where the part's orientation has changed to compensate for the overhanging angle. Combining these systems can theoretically eliminate the size restrictions of the parts that can be built using AM. This sparks considerable interest from not only the energy sector but shipping, mining, and any industry that requires large-scale parts. The complexity of these parts is not due to stringent geometrical tolerances but is restricted by the sheer size of the components [24]. One rendition of this is the combination of additive and subtractive manufacturing, which takes the free formability of AM and combines it with the surface finish capabilities of machining. This is known as hybrid manufacturing [25, 26]. Researchers have been developing path planning programs for these types of systems, but the combination of the two processes drastically increases cost compared to pure AM processes because of longer fabrication times, and would not be suitable for large scale applications in the current state [27, 28, 29, 30, 31, 32, 33].

The current objective of large-scale additive manufacturing is to use 7- and 8-axis robotic serial manipulator systems, and in-situ monitoring and control systems, to eliminate the need for subtractive measures and supporting structures [18, 36, 37, 38, 16, 39]. The different technologies to achieve this have been implemented in various other applications but have not yet been integrated into a holistic process. Various companies have implemented commercial large-scale robotic AM, including: Relativity Space [40], MX3D [41], MER corporation, AML3D [42], and AMFG [43]. Two examples of large-scale components fabricated via robotic AM are shown in Figure 2. However, their methodologies have not been published and will not be considered in this work.

With the increase in commercialization of additive manufacturing systems, and the implementation of additively manufactured parts into various industrial applications, it is critical to developing standards to qualify and certify the entirety of the process, from feedstock to finished part. This ensures the same repeatable quality and performance of additive manufactured parts, as those seen in the commercial manufacturing space. Furthermore, it is important that the development of these systems conform to the strict environmental, health, and safety regulations currently in place. As engineers, it is imperative that the safety of the public is the top priority. The codes and standards pertaining to the qualification and certification of DED AM are shown in Table 1. It should be noted that many of these standards are still under development, highlighting the challenges the various standard committees have with developing strict qualifications for DED AM.

This paper aims to identify the state-of-the-art technologies and how they relate to large-scale additive manufacturing and the interdisciplinary engineering challenges that this process encompasses. For this work, large-scale AM constitutes the ability to fabricate a part with a volume of 1 m^3. The current state of research highlights the lack of collaboration between engineering disciplines and the connections that lie between different research bodies. The majority of other published literature reviews only review a sub-set of the various research bodies and sub-topics of large-scale robotic AM, whereas this work reviews these independent research findings and attempts to highlight the relationships between them. Most of the research discussed herein encompasses laboratory-scale coupons and not specifically large-scale parts. However, it is speculated

(a) (b)

Figure 2: Examples of companies adopting the large-scale robotic AM technology with (a) a rocket nozzle fabricated by Relativity Space, Inc. [34] and (b) a component of a serial manipulator fabricated by MX3D [35].

that many of the contributions made will be transferable beyond the lab.

The structure of this paper is as follows. The first sections will discuss the various DED technologies to provide context to the complexity of the manufacturing systems. This will transition to the different stages of the AM workflow, shown in Figure 3, where stage 1 is pre-process planning, stage 2 is printing/deposition, and stage 3 is post-processing. Stage 1 encompasses the decomposition of the part into sub-volumes, the cross-sectional slicing of said subvolumes, and the conversion of the sliced layers to a tool path and deposition strategy based on the deposition system being used. Although not directly addressed by the publications, the thermo-physical properties, and the thermal properties will dictate the optimal deposition strategy to reduce residual stresses, deposition defects, and microstructural anisotropy. This will vary depending on the material being deposited. Stage 2 corresponds to the monitoring and control of the deposition and extracting the valuable information from the various sensors, which are used to adjust the operating parameters of the system in-situ. The development of this stage is critical to automating large-scale AM, making it commercially viable for on-site manufacturing by non-specialized personnel and potentially eliminating the need for stage 3. An important consideration is optimizing the thermal cycles to achieve the microstructure and corresponding mechanical properties required for the parts application. Stage 3 deals with the post-processing required for the part to meet metallurgical, geometrical, and performance specifications required for in-service use. Each stage corresponds to separate chronological sections of this paper, where each constituent of that stage and its current state in regards to large-scale additive manufacturing will be discussed. The paper will conclude with the author's perspectives on the challenges that must be overcome to make large-scale AM a commercially viable manufacturing option.

2. Metal deposition technologies

The main metal deposition technologies found in large-scale AM are: Gas Metal Arc Welding (GMAW), Gas Tungsten Arc Welding (GTAW), Plasma Transferred Arc Welding (PTAW), and Laser-based direct energy deposition (LDED). A detailed illustration of these deposition technologies can be seen in Figure 4. These systems are most readily used due to the ease of integration with the current multi-axis systems or have previously been used on robotic systems in industries such as automotive manufacturing. One advantageous characteristic with these modalities is higher heat inputs, which enables higher deposition rates, accelerating the printing process. This is an essential factor for large-scale AM to reduce the lead time for part production. However, one caveat to higher heat input is higher thermal stresses and heat accumulation, resulting in large amounts of material undergoing complex thermal cycling and anisotropic microstructures [44, 45, 46]. Furthermore, the material feedstock for DED is typically wire, or powder-based, which offers the ability to alter both deposition rate and composition based on the mechanical specifications of that localized area [47, 48, 49]. Changing the composition could range from going from one material to another or changing the volume loading of reinforcement particles in a metal matrix compos-

Table 1: Some of the existing and under development codes and standards pertaining to additive manufacturing. It should be noted that this is not an exhaustive list, but provides insight on the magnitude and breadth of standards being developed for DED AM.

Identifier	Description
ISO 17296-(1-4)	Additive manufacturing – General principles (Active standard)
ISO/ASTM 52901:2017	Additive manufacturing – General principles – Requirements for purchased AM parts (active standard)
ISO/ASTM 52907:2019	Additive manufacturing – Feedstock materials – Methods to characterize metal powders (active standard)
ISO/ASTM 52902 - 19	Additive manufacturing – Test artifacts – Geometric capability assessment of additive manufacturing systems (active standard)
ASTM F3413 - 19	Guide for Additive Manufacturing – Design – Directed Energy Deposition (active standard)
ASTM F3049 - 14	Standard Guide for Characterizing Properties of Metal Powders Used for Additive Manufacturing Processes (active standard)
ASTM F3187 - 16	Standard Guide for Directed Energy Deposition of Metals (active standard)
AMS7027	Electron Beam Directed Energy Deposition-Wire Additive Manufacturing Process (EB-DED-Wire) (active standard)
AMS7010	Wire Fed Laser Directed Energy Deposition Additive Manufacturing Process (L-DED-wire) (active standard)
AMS7005	Wire Fed Plasma Arc Directed Energy Deposition Additive Manufacturing Process (active standard)
AMS7004	Titanium Alloy Preforms from Plasma Arc Directed Energy Deposition Additive Manufacturing on Substrate Ti-6Al-4V Stress Relieved (active standard)
ASTM F3187-16	Standard Guide for Directed Energy Deposition of Metals, 2016 (active standard)
ASTM WK69730	New Specification for Additive Manufacturing – Wire for Directed Energy Deposition (DED) Processes in Additive Manufacturing (under development)
ISO/ASTM AWI TR 52905	Additive manufacturing of metals – Non-destructive testing and evaluation – Defect detection in parts (under development)
ISO/ASTM CD 52926-4	Additive manufacturing of metals – Qualification principles – Part 4: Qualification of machine operators for DED-LB (under development)
ISO/ASTM CD 52926-5	Additive manufacturing of metals – Qualification principles – Part 5: Qualification of machine operators for DED-Arc (under development)
AMS7037	Steel, Corrosion and Heat-Resistant, Powder for Additive Manufacturing 17Cr - 13Ni - 2.5Mo (316L) (under development)

ite. This functional gradient could allow for customized spatial mechanical properties of areas that require them while also reducing the material cost of manufacturing. In this section, the following technologies will be discussed: GMAW, PTAW, and LDED. This will include the fundamentals of the operation and the mechanisms of deposition. This will be followed by the common material feedstocks and the as-deposited microstructures that are typically found. The range of processing parameters for each deposition technology based on whether the feedstock is powder or wire are shown in Table 2 and Table 3, respectively. The values listed in the tables are the minima and maxima for each parameter recorded in the literature. Additionally, authors whose parameters fall within the range are given. It should be noted that lamination AM and cold-spray AM are also capable of creating large-scale parts. Lamination AM is currently not compatible with multi-axis robotic systems, eliminating it from consideration. Cold-spray AM is compatible with robotic systems but lacks the ability to create complex parts without special equipment, and significant post-processing [50, 51, 52]. Thus, it was not considered in this work.

2.1. *Gas metal/tungsten arc welding*

In gas metal arc welding, an arc is struck between a substrate and a consumable wire electrode that is fed through the welding torch, where it is melted and deposited onto the substrate. The molten material is protected from moisture and oxidation through the use of shielding gases, which are typically a combination of inert (Ar) and active (CO_2). The shielding gas varies things like the stability of the arc, metal transfer, and penetration of the weld and is tailored to the material being deposited. The wire is continuously fed as the welding torch is translated in the geometry of the weld or AM part. The consumable electrode is either a solid wire or a cored wire, with a powdered interior in various ferrous and non-ferrous compositions. The current is directly proportional to the deposition rate but inversely proportional to the electrode extension, which is the distance between the end of the wire guide and the tip of the electrode, shown in Figure 4(a). The arc voltage is a means of electrically quantifying the physical length of the arc and can be affected by many factors, including: electrode composition and size, shielding gas composition, electrode extension, and the length of the welding cable [53]. The deposition rate for

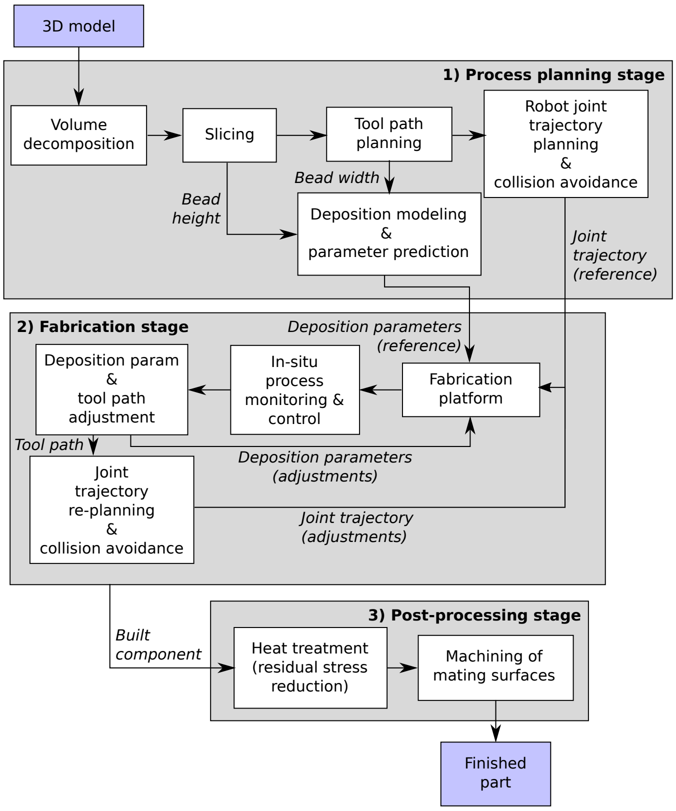

Figure 3: The robotic large-scale metal AM process workflow.

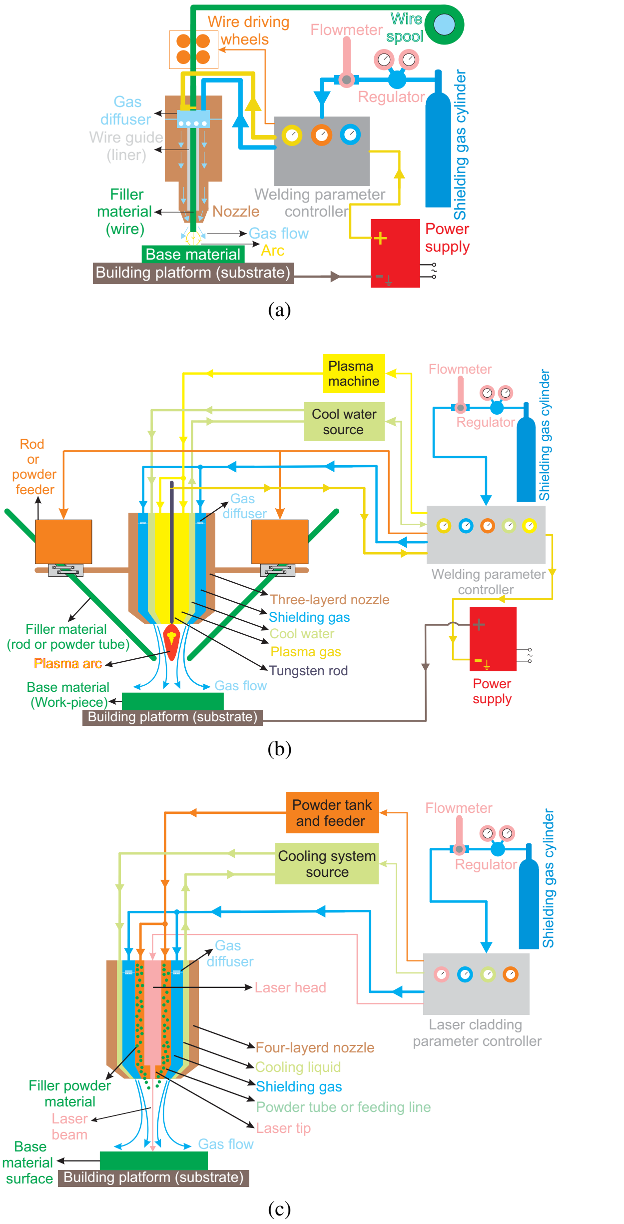

Figure 4: Various AM DED technologies; (a) GMAW, (b) PTAW, and (c) LDED.

GMAW in terms of AM is material dependent, but is in the range of 15-160 g/min [54, 55, 56].

Three traditional transfer modes are commonly used with the GMAW process, which are: spray, globular, and short circuiting [57]. Cold metal transfer (CMT) is a modified subsidiary of short circuiting, where the mechanical movement of the wire electrode is synchronized with the electrical control parameters [58]. Instead of increasing the current during the short circuit phase, the current is dropped, extinguishing the arc and limiting the amount of thermal energy transferred to the deposit [59]. The electrode is then retracted, pinching the molten material, depositing it into the melt pool. The current is then increased to reignite the arc, and the process repeats [60]. The decrease in thermal energy transfer reduces the heat accumulation in multi-layer deposits, which can be characterized by the finer grain structures when compared to continuous welding techniques [58, 61]. This can be seen in Figure 5 [62], where the lower heat input and heat accumulation is characterized by the finer grain structure. Furthermore, the pulsing of the arc has been shown to sever dendrite arms, increasing the heterogeneous nucleation sites, further refining the microstructure [63, 64]. It also drastically reduces the dilution of previously deposited material, reducing the amount of material being melted with each pass and possibly reducing the number of thermal cycles [60, 65]. Thus, these reasons make CMT the most viable option for wire and arc additive manufacturing (WAAM). It should be noted that although there is a reduction in heat input and thermal cycles compared to continuous welding, WAAM deposits still suffer from heat accumulation, cracking, porosity, delamination, and anisotropic microstructures. [66] The first study of using GMAW for AM was conducted by Dickens *et al.*, who tried to expand the realm of 3D welding from large pressure vessels, to more complex geometries [67].

Gas Tungsten Arc Welding is similar to the GMAW process, but the arc is struck between a non-consumable tungsten electrode and the workpiece. A filler metal can be fed manually or mechanically into the arc, where it melts and is deposited onto the substrate. Multiple filler metals can be fed simultaneously to increase the deposition rate and allow for the customization of the material being deposited. Inert shielding gasses (typically Ar or He) protect the melt from oxidation while also af-

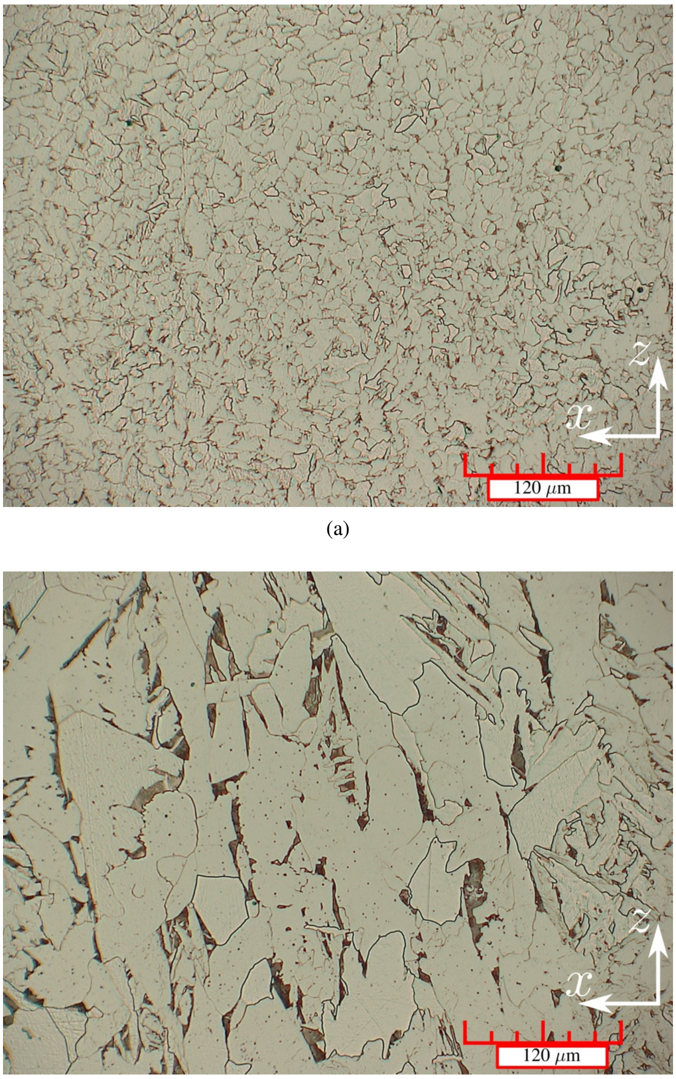

(a)

(b)

Figure 5: Microstructure variations from the WAAM deposition of AWS ER70S-6 where (a) shows the finer grain structure of a deposit with low heat input and low amounts of heat accumulation, and (b) show the grain structure with high heat input and large amount of heat accumulation [62].

fecting weld bead geometry. The polarity of the system can be altered from DC to AC if the material being deposited is prone to forming passive films [68]. The microstructure and mechanical properties of AM deposits are highly dependent on the material feeding orientation [69, 70]. Some of the materials that have been deposited include: TiAl [71], Fe-FeAl functionally graded material [72], FeAl [73], Ti64 [74, 75, 76, 77], Al [78], and Ni alloys [79].

GMAW and GTAW offer a cost-effective means of AM, with techniques that are already common industrial practice. The ease of integration with robotic control and gantry systems, coupled with the high deposition rates, makes these technologies enticing for large-scale additive manufacturing [80]. However, some complications reside when using a welding heat source for AM. Distortion and residual stresses are common side effects of the concentrated heat flux generated from an arc [81]. Inconsistent bead geometries can lead to poor surface finish, and dimensional accuracy [82]. Research has predominately been on GMAW, which is speculated to be due to the added complexity of integrating a wire feeding system with the robotic system. Ensuring the feeding angle is constant during deposition would increase the difficulty of path planning and building strategies. The continuous heat input experienced during GTAW could cause increased heat accumulation, resulting in manufacturing defects such as the slumping of different features. Furthermore, GMAW's ability to easily strike and extinguish an arc increase the thermal control during the build by extinguishing the arc after each pass to allow for the part to cool. The tungsten electrode in GTAW also requires frequent sharpening to maintain arc characteristics, decreasing the production rate of large-scale parts.

2.2. *Plasma Transferred Arc*

Plasma transferred arc utilizes a non-consumable tungsten electrode, similar to that seen in GTAW; however, there are some stark differences between the processes as can be viewed in Figure 4(b). Generally, there are two inert gas inlets: the plasma and shielding gas. The gasses used in this process (such as Ar) are chosen due to their low ionization potential, making it easier to strike an arc between the electrode and the substrate. The flow of the plasma gas allows the arc to be self-sustaining, while the shielding gas protects the melt from the surrounding environment [83]. The plasma is constricted by a nozzle, changing the arc shape from the traditional bell shape to columnar, increasing the energy density [84]. The feeding material can either be wire, or powdered materials, allowing for a large degree of compositions and functionally graded parts. The deposition rate is the highest of the welding techniques are 33-166g/min [83]. Some of the materials that are being explored with PTA for additive manufacturing are: Ni alloys [85, 86, 87, 88], Ni-WC [89], Ti [90], functionally graded Fe-Ni [91, 92], and stainless steel alloys [93, 94].

2.3. *Laser-based direct energy deposition*

Laser-based DED techniques share the basic principles with the aforementioned plasma-based methods, where the main difference lies in the energy source. For laser systems, a series of lenses are used to focus a laser beam to melt the desired material [95]. The laser source can vary depending on the particular application. CO_2 lasers are better suited for low precision, simpler geometries, where an Nd-YAG laser is better suited for finer, complex geometries [96]. The feed material for laser DED can be powder, wire, or a combination of the two, depending on the application. A schematic of a typical laser system is shown in Figure 4(c). The deposition rate can be up to 25 g/min with varying deposition efficiencies depending on the components geometry [97]. Both heat sources share a Gaussian energy distribution, with the highest temperatures in the center of the melt. However, the heat flux provided by a laser source is upwards of $1kW/mm^2$ with a 2mm diameter spot size [98, 99, 100], while a plasma provides upwards of $60W/mm^2$ over 16mm diameter spot size [83, 101]. Another critical distinction is the safety precautions that workers must abide by during laser DED. To strike an arc, the workpiece must be electrically grounded and can only be sustained within a certain stand-off distance. Commercial lasers do not have any of these pre-requisites, meaning they can theoretically be directed at any surface. Additionally, a laser can be reflected by certain metallic surfaces that can damage facilities or personnel. Thus, proper control measures must be implemented to ensure the safety of anyone working with this equipment.

2.4. Materials

In all AM techniques, the feedstock metals can be in the form of wire or micron-size powder. Powder metals are typically much more expensive than their wire counterparts, but offers material compositions that are not able to be drawn into a wire. An example of this are higher reinforcement loaded MMC's and intermetallics, where the inherent brittle nature of these materials make it un-suitable for wire applications [212]. However, the deposition efficiency of wire fed systems are beyond what is possible with powder [213]. Moreover, storage of metal powders requires significantly more safety precaution than that of metal wires and the higher surface area to volume ratio makes them more susceptible to oxidation [214]. The quality of the feedstock is of utmost importance, as porosity in the feedstock powders has been shown to drastically increase the porosity of the printed part[143]. Poor surface quality and diameter variances of wire feedstock can trap moisture and hydrocarbon residue during the deposition process, resulting in porosity in the final deposit [215, 216, 217, 218] This section of the report will outline the common materials and the as-built microstructures found in the above mentioned AM techniques, as shown in Table 2 and Table 3. The variation in mechanical properties of AM deposits will be compared to conventional manufacturing where applicable, and the microstructural justification for differences will be discussed. The order of materials is as follows: first steels will be discussed, followed by titanium, aluminum, nickel, magnesium, copper, cobalt-chrome, and tungsten alloys. It should be noted that there has been work done on energetic materials, typically in the form of metal-polymer composites. However, the printing modalities for these materials are currently limited to those suited for polymer materials and were deemed out of the scope of this paper. The topics discussed in Section 3 and Section 4 can be applied to the deposition of energetic materials, specifically those that utilize a deposition nozzle like direct writing, fused deposition modelling and photopolymerization [219].

2.4.1. Steels

Steels are extensively used in various industrial sectors due to their high strength, good toughness, and low cost. There has been extensive work on the AM of steels, especially with WAAM. Some honourable mentions include: ER70S-6 [150, 148, 220, 151], 304 SS [148, 221, 149, 176], 308L SS [152, 193, 177, 153], and AISI 420 SS [154].

In the case of 316L austenitic stainless steel, LDED fabricated parts were reported to exhibit a higher hardness, yield stress, and tensile strength with lower elongation than their wrought counterparts [105]. These differences in mechanical properties were attributed to the finer cellular arm spacing of the LDED manufactured steel compared with the wrought one [105]. The grain structure of LDED fabricated 316L stainless steel is highly dependent on process parameters, where grains become coarser by increasing power density and decreasing scan speed [102]. The 316L stainless steel fabricated by GMAW-AM was reported to have greater hardness and UTS, but a lower elongation than the wrought steel [155]. Microstructure and mechanical properties of the GMAW-AM fabricated 316L stainless steel depend on arc mode. A finer grain size (and consequently a higher strength and hardness) is achieved when spray transfer mode is replaced with short-circuiting transfer mode [155]. This is explained by the lower heat input of the short-circuiting than the spray transfer more, which leads to a faster cooling rate [155].

Another common steel grade in AM is 17-4 PH martensitic stainless steel. However, the majority of the work has been on powder bed methods [222, 223, 224, 225, 226, 227], as opposed to DED [228, 229, 103, 56, 156, 143]. High cooling rates associated with the selected AM processes limit transformation of δ-ferrite to γ-austenite at high temperatures so that some amounts of δ-ferrite remain at room temperature. AM fabricated 17-4 PH stainless steels commonly exhibit a dendritic microstructure with interdendritic δ-ferrite in a lath martensitic matrix [103, 56, 156]. It has been shown that proper shielding must be implemented with PTA-AM of 17-4 to prevent interlayer oxidation during fabrication[143]. Caballero *et al.* [156] fabricated 17-4 PH stainless steel from a wire feedstock using a GMAW-AM technique. They reported that decreasing the heat input to the system increased the solidification rate and subsequently the amount of retained austenite in the as-built microstructure. Moreover, the as-built parts had lower yield stress and UTS than wrought 17-4 PH stainless steel. However, exposure to a solution and aging heat treatment increased their yield stress and UTS significantly to be comparable with those of the wrought alloy [156]. Adeyemi *et al.* [103] investigated the influence of laser power on the microstructure of LDED fabricated 17-4 PH stainless steel. They observed a coarse microstructure at a high laser power due to high laser intensity and consequently slower cooling rate [103]. In another study, Martina *et al.* [56] fabricated walls from 17-4 PH stainless steel wires using a GMAW-AM technique, a tandem torch. They reported a drop in strength and hardness of the deposited walls with an increase in wire feed speed, which was attributed to an increase in grain size [56].

Anisotropy of both microstructure and mechanical properties is significant in DED fabricated steel parts. The microstructural grains and dendrites are preferentially oriented along the build direction with the highest thermal gradient [106]. Thus, for the vertical orientation parts in which the build direction is parallel to the deformation direction, fewer grain boundaries exist compared to the horizontal orientation parts in which the tensile direction is perpendicular to the build direction. Since grain boundaries act as barriers to dislocation motion during the deformation, less dislocation accumulation occurs in the

Table 2: A listing of various powder fed deposition technologies and associated parameter based on the material being deposited. The values listed provide the maximum and minimum for each parameter and the authors who's parameters fall within those ranges.

Process	Material	Travel Speed (mm/s)	Heat Input (W)	Spot Size (mm)	Layer height (mm)	Material feed rate (g/min)
	Steels	2.5 [102] - 20 [103] Within range: [104, 102, 105, 106, 107, 108]	360 [107] - 2600 [103] Within range: [104, 106, 105, 108]	1.2 [108] - 2 [103]	0.25 [107] - 0.5 [108]	2 [108] - 20.4 [102] Within range: [104, 105, 103, 106, 102]
	Ti-6Al-4V	2 [109] - 17 [110] Within range: [111, 112, 113, 114, 115, 116, 117, 118, 119]	330 [117] - 7000 [113] Within range: [111, 109, 112, 114, 115, 116, 110, 118, 119]	0.3 [117] - 8.6 [114] Within range: [111, 112, 113, 116, 118, 109, 119]	0.3 [109] - 3 [113] Within range: [110, 114, 115]	1 [112] - 59 [119] Within range: [110, 111, 109, 112, 114, 115, 116, 118, 117, 113]
laser DED	Aluminium	6 [120] - 16 [121] Within range: [122, 123, 124, 125, 126]	120 [124] - 3600 [120] Within range: [122, 123, 125, 121, 126]	0.6 [125] - 3.5 [120] Within range: [123]	0.5 [120]	0.66 [124] - 23.2 [123] Within range: [122, 125, 126]
	Nickel (Inconel 625)	6.7 [127] - 25 [128] Within range: [129]	1500 [129] - 3000 [127] Within range: [128]	0.4 [129] - 3 [127] Within range: [128]		6 [127] - 33.3 [128] Within range: [129]
	Nickel (Inconel 718)	2 [130] - 26.6 [131] Within range: [132, 133, 134, 118, 135, 128, 136]	250 [130] - 4000 [131] Within range: [132, 133, 128, 118, 135, 136, 134]	0.8 [132] - 5 [131] Within range: [133, 134, 118, 128]	0.1 [130] - 0.5 [132]	1.2 [118] - 36.6 [131] Within range: [128, 133, 135, 134, 136]
	Co-Cr	5.5 [137] - 20 [138] Within range: [139, 140]	200 [139] - 410 [137] Within range: [140, 138]	0.25 [140] - 0.7 [139]	0.25 [139] - 0.5 [137]	0.57 [140] - 5 [138] Within range: [139]
	W	2 [141] - 5 [142]	200 [141] - 2000 [142]	0.6 [141] - 3 [142]	0.8 - 0.9 [141]	7 [141] - 8 [142]
PTA	Steels	1.3 - 1.7 [143]				25 - 35 [143]
	NiCrBSi	10 [89]	1100 [89]	4.7 [89]	0.75 [89]	20 [89]

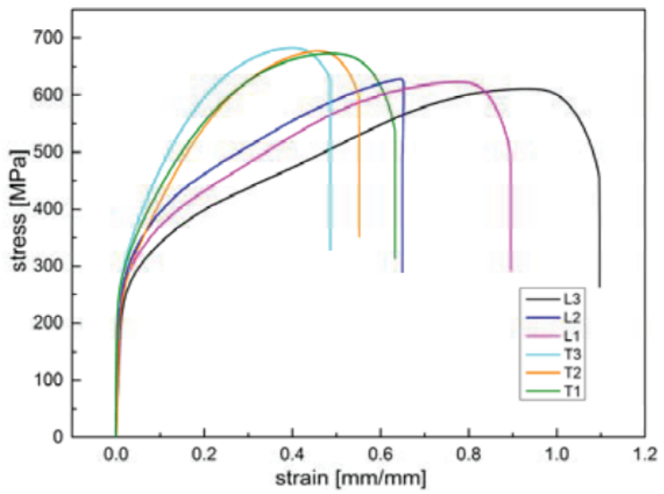

Figure 6: Tensile plots of WAAM fabricated 304L stainless steel for vertical orientation (L1, L2, and L3) and horizontal orientation (T1, T2, and T3) [176].

vertical orientation parts than horizontal orientation parts. Consequently, the vertical orientation parts exhibit a lower tensile strength but a higher elongation than the horizontal orientation parts. This anisotropy of the mechanical properties has been reported for the LDED fabricated 304L stainless steel [107], WAAM fabricated 304L stainless steel [176] LDED fabricated 316L stainless steels [108, 107, 106], WAAM fabricated 316L stainless steel [157], WAAM fabricated H13 tool steel [158], and WAAM fabricated 17-4 PH stainless steel [156].

For example, the influence of part orientation on the tensile behavior of WAAM fabricated 304L stainless steel is depicted in Figure 6 [176]. The vertical orientation parts (L1, L2, and L3) exhibited an average yield stress, UTS, and elongation of 231 MPa, 622 MPa, and 88.1%, respectively [176]. Horizontal orientation parts (T1, T2, and T3), however, were reported to have an average yield stress, UTS, and elongation of 235 MPa, 678 MPa, and 55.6%, respectively [176]. For most industrial applications, fabricated parts need to exhibit uniform mechanical properties. Thus, the anisotropy of the mechanical properties in the AM steel parts is a challenge. Several studies were conducted to solve this issue. Wu et al. [157] investigated the anisotropy of the mechanical properties in 316L stainless steel components fabricated by speed cold welding AM. They observed a pronounced reduction in the anisotropy by decreasing scan speed and increasing cooling time. This was attributed to the cooling rate reduction [157]. Wang et al. [158] reported that the mechanical properties of the WAAM fabricated

Table 3: A listing of various wire fed deposition technologies and associated parameter based on the material being deposited. The values listed provide the maximum and minimum for each parameter and the authors who's parameters fall within those ranges.

Process	Material	Travel Speed (mm/s)	Heat Input (W)	Spot Size (mm)	Layer height (mm)	Wire feed Speed (mm/s)
laser DED	Ti-6Al-4V	1.4 [144] - 10 [76] Within range: [145, 146]	1000 [146] - 3500 [76] Within range: [145, 144]	2.5 [144] - 5 [76] Within range: [145]	1 [76] - 1.28 [145]	30 [145] - 40 [76]
	Nickel (Inconel 718)		5000 [147]	1 [147]		
GMAW	Steels	2.5 [148] - 30 [149] Within range: [150, 151, 152, 153, 154, 155, 156, 157]	3500 [158] - 8400 [159]		0.5 - 2 [149]	28 [151] - 166 [159] Within range: [148, 150, 151, 153, 154, 155, 156, 157, 149]
	Ti-6Al-4V	1.5 [160] - 9.4 [58] Within range: [161, 162, 163]	1430 [160] - 12500 [162] Within range: [58]	6 [161] - 10 [160]	14 - 16 [160]	7.2 [160] - 142 [58] Within range: [162]
	Aluminium	6.13 [63] - 22 [164] Within range: [165]	3360 - 7360 [164]			100 [63] - 250 [164] Within range: [165]
	Nickel (Inconel 718)	6 [166] - 10 [167] Within range: 6.5 [168]		12.8 [167]	1.7 [167] - 2.8 [166]	10 [167] - 116.6 [166] Within range: 33.3 [168]
	Nickel (Inconel 625)	6.3 [169] - 10 [170]	2160 [170]			108 [170]
	Magnesium	3.3 - 16.6 [171] Within range: [172, 173]	400 - 1400 [171] Within range: 541 - 857 [172]	5 [172]	3 [172]	30 [172] - 200 [173]
	Copper alloys	6.6 [55] - 8.3 [174]	4620 [174] - 7424 [55]			117 [174]
	Co-Cr	2.1 [175]	1454 [175]		3.5 [175]	75 [175]
GTAW	Steels	2.92 [176] - 7 [177] Within range: [178]	1920 [178]			16.67 [176] - 58 [177] Within range: [178]
	Ti-6Al-4V	0.27 [64] - 6.7 [75] Within range: [179, 76, 177, 180, 181]	1320 [180] - 2200 [76]	5 [75] - 9.1 [76] Within range: [179, 180]	1 [76]	10 [75] - 128 [75] Within range: [177, 179, 76, 160, 180, 181, 64]
	Aluminum	3.3 [182] - 100 [183]				17 [182] - 160 [183]
	Nickel (Inconel 718)	5 [184]		10 [184] -16 [185]		25 [184]
	Magnesium	3.3 [186] - 5 [187, 188]			1.25 - 2.5 [186]	19.2 [187, 188] - 33.3 [186]
	Copper Alloys	1.6 [189]				21.6 [189]
	Co-Cr				1.1 [190]	16.6 [190]
	W	2 [191]				35 [191]
PTA	Steels	0.6 [192] - 2 [193]	350 [192] - 3510 [194]			9 [193] - 28 [192]
	Ti-6Al-4V	4 [195, 196]	2700 - 5400 [196]		1.5 [195, 196]	58 [195, 196]
	Nickel (Inconel 625)	21.6 [197]			1.2 [197]	3 [197]
EB	Ti-6Al-4V	2.4 [198] - 18 [198] Within range: [199, 200, 201, 202, 203, 204, 205, 206, 207, 208, 209]	690 [205] - 8500 [209] Within range: [199, 200, 201, 202, 203, 198, 206, 207, 208, 204]	1.2 [199]	1 [210]	14 [203] - 141 [198] Within range: [199, 202, 204, 206, 207, 208]
	Inconel 718	5 [211]	600 - 960 [211]			5.4 [211]

H13 steel became isotropic as a consequence of annealing at 830 C for 4 hours. In another study, Fu et al. [230] eliminated anisotropy of mechanical properties in a bainitic steel using a combination of WAAM and micro-rolling. This hybrid technique's fully equiaxed grain structure resulted in the isotropic mechanical properties [230].

2.4.2. Titanium Alloys

Titanium alloys are widely used in the aerospace industry due to their high strength-to-weight ratio [231]. The allotropic nature of titanium alloys, in addition to high-temperature thermal cycles associated with AM techniques, allows for various microstructures, and consequently, mechanical properties [232]. Moreover, titanium components with complex geometries cannot be easily fabricated using conventional manufacturing techniques due to titanium alloys' poor machinability. The low thermal conductivity of Ti results in poor thermal dissipation during machining, leading to poor surface quality, accuracy and reduces machining tool life [233]. These factors make titanium alloys an attractive candidate for AM. Ti-6Al-4V (Ti64) alloy contains an allotropic microstructure of hcp α- and bcc β-phases, and is the most widely AM-fabricated alloy among all metallic alloys [209, 179, 180, 76, 181, 114, 115]. AM-fabricated Ti-6Al-4V alloys exhibit higher strength but lower ductility than conventional manufacturing techniques such as casting and forging [196, 116]. This can be explained by the formation of α'-martensite due to the high cooling rates associated with the selected AM techniques. The ductility of AM-fabricated Ti-6Al-4V components can be enhanced by applying heat treatments at the cost of reducing the overall strength of the material [162, 117]. Zhai *et al.* used a high-power laser to fabricate Ti-6Al-4V components, resulting in an as-built UTS and elongation of 1042 MPa and 7%, respectively [117]. Similar mechanical properties were reported for the Ti-6Al-4V alloy fabricated by GMAW [162] and pulsed plasma arc AM [196]. These findings can be explained by the similarity in their microstructures, where fine acicular α'-martensite with a small amount of $\alpha+\beta$ lamellae was observed [196, 162, 117]. In the case of LDED, when the laser power decreased from 780 W to 330 W, the mixed microstructure of α'-martensite and $\alpha+\beta$ lamellae was replaced with a fully martensitic microstructure [117]. This was attributed to the acceleration of the cooling rate as a consequence of the decreased laser power. The microstructure change led to a UTS enhancement from 1042 MPa to 1103 MPa, but an elongation drop from 7% to 4% [117].

Columnar grains and strong crystallographic texture of β <001> along the build direction in DED fabricated titanium alloys lead to an anisotropic microstructure [234, 235]. The anisotropy of the microstructure causes anisotropy of mechanical properties. In general, horizontally built parts exhibit higher yield stress and UTS but lower elongation than vertically built parts. This behavior has been observed for LDED fabricated Ti-6Al-4V alloy [236], LDED fabricated TC21 alloy [237], LDED fabricated TA15 alloy [238] and WAAM fabricated Ti-6Al-4V alloy [74]. Anisotropic mechanical properties can be eliminated by obtaining an equiaxed grain structure with a random crystallographic orientation. Such a microstructure can be achieved by using interpass rolling between deposited layers [181], adding grain refining elements during AM [239], changing process parameters (for example, increasing powder feed rate and lowering laser energy density) [240], and applying post-process heat treatments [241]. These procedures can extend the application of DED fabricated titanium alloys into components that are required to exhibit uniform mechanical properties in all directions.

2.4.3. Aluminum Alloys

Aluminum alloys are the most extensively used non-ferrous metallic alloys in engineering components due to their high strength, low density, good ductility, and high corrosion resistance. Additive manufacturing of aluminum alloys is more challenging than steels and titanium alloys due to their high thermal conductivity. Therefore, the power of the different heat sources needs to be increased during AM to prevent quick heat dissipation [63, 242]. This is especially prevalent when the heat source is a laser beam because aluminum alloys have a high reflectivity [122]. The optics train can be damaged from the reflected laser, which can be counteracted by introducing a minor z-axis tilt to the laser head [242]. The increased power of heat sources can lead to the evaporation of some alloying elements such as zinc and magnesium during manufacturing, resulting in porosity due to gas entrapment [243, 244]. This limits the range of aluminum alloys that can be fabricated by AM. Aluminum also forms a strong passive oxide layer on the feedstock material, reducing the wettability of the melt during fabrication [245]. The presence of a large solidification range is another factor limiting AM of aluminum alloys. The segregation of alloying elements during solidification decreases the melting temperature of the grain boundaries, creating a liquid film. The thermal stresses induced by the high thermal expansion of Al can cause intergranular rupture of the grain boundaries, resulting in hot cracking [183, 164, 246]. The addition of silicon has been shown to reduce the susceptibility of hot cracking by reducing the solidification range, enhancing fluidity, and decreasing the thermal expansion coefficient [247, 244]. Moreover, it forms a fine low melting eutectic structure that can backfill cracks and increase the grain boundary area, preventing crack growth [244]. Among aluminum alloys, AlSi10Mg is the most extensively AM-fabricated alloy [248, 249, 123, 120, 125], although others like Al 5356 [250, 251, 252, 253] and Al 4043 [254, 255, 256, 257] have also been studied. The alloy is a hypoeutectic Al-Si alloy with a composition close to eutectic. The presence of a small amount of magnesium ($\approx$ 1 wt. %) makes this alloy age-hardenable through Mg_2Si precipitation. The mechanical properties of AlSi10Mg alloy mainly depend on the morphology and size of the eutectic phase. The slower cooling rate in casting results in a larger cell structure with large intercellular Si particles. The larger Si particles act as crack initiation sites that can propagate easily through larger celled structures leading to low strength, and poor ductility [258, 259, 260]. However, AM techniques with high solidification rates can refine the eutectic phase and consequently enhance the alloy mechanical properties [249, 121].

2.4.4. *Nickel Alloys*

Nickel alloys are extensively applied in gas turbine engines, nuclear reactors, rocket engines, submarines, and space vehicles owing to their high strength and oxidation resistance at elevated temperatures [168]. Various nickel alloys have been used in the selected AM techniques including Inconel 625 (In625) [261, 128, 262], NiCrBSi alloy [89], Inconel 718 (In718) [147, 263] and Ni-Fe-V [264, 265] alloy. AM-fabricated Inconel 718 typically yields a dendritic structure of FCC γ, with the segregation of Nb and Mo to the interdendritic regions, characterized by the formation of Laves phase $((Ni,Cr,Fe)_2(Nb,Mo,Ti))$ [168, 167, 185]. The presence of the Laves phase suppresses the formation of γ" (Ni_3Nb), the main contributor to In 718 superior mechanical performance, by depleting the matrix of Nb [132]. The fast cooling rates associated with AM, lead to a finer microstructure and less segregation than that of cast Inconel 718, resulting in comparable or slightly superior mechanical properties [130, 184]. The lack of precipitation strengthening and the defect accumulation during deposition leaves as-built AM deposits with inferior properties compared to wrought Inconel 718. This is remedied through heat treatment or hot isostatic pressing (HIP) [133, 134, 166]. Inconel 625 superalloys fabricated by a pulsed plasma arc (PPA) AM exhibited a yield stress, UTS, and elongation of 438 MPa, 721 MPa, and 49%, respectively [197]. Similar mechanical properties were reported for the same superalloy manufactured by a GMAW-AM technique [169]. These mechanical properties are greater than those of the as-cast Inconel 625 superalloy. This can be explained by finer dendrites and precipitates observed in the microstructure of AM built Inconel 625 superalloy [197, 169]. However, yield stress and UTS of Inconel 625 fabricated by PTA-AM or GMAW-AM are not as high as those of the wrought Inconel 625. This can be attributed to the fine equiaxed grain structure of the wrought superalloy. The LDED built Inconel 625 superalloy was reported to have higher yield stress (540 MPa) but a lower UTS (690 MPa) and elongation (36%) than the wrought superalloy [127].

2.4.5. *Magnesium Alloys*

Magnesium alloys are the lightest engineering metal available with an approximate density of 1.74 g/cm3, which is significantly lower than that of steels, titanium alloys, and aluminum alloys[266]. Although the application of magnesium alloys has been limited owing to their low corrosion resistance and poor mechanical properties, their biocompatibility and elastic modulus comparable with human bones make these alloys an attractive candidate for biomedical applications [267]. Moreover, magnesium alloys are widely used to fabricate dissolvable downhole tools, where a high specific strength and corrosion rate are required [268]. Fabrication of magnesium alloys through forming processes such as forging and extrusion has been limited due to their limited active slip systems at room temperature, and high oxidation rate at elevated temperatures [269]. Furthermore, the casting of magnesium alloys does not allow for the fabrication of parts with complex geometries or the fine microstructures required to achieve good mechanical properties. Thus, AM techniques are being explored to target unique microstructures and high performance in magnesium alloys. Guo et al. [187] fabricated single pass multi-layer walls from AZ80M alloy wires using a GTAW-AM method. The as-built microstructure mainly comprised α-Mg and β-Mg17Al12 with small amounts of Al2Y phase [187]. This phase assemblage is typical for wrought AZ80M magnesium alloys. Mechanical properties of the GTAW-AM fabricated AZ80M alloy [187] were insignificantly different from those of a wrought sample. In another study, Guo et al. [186] fabricated full-dense components from AZ31 alloy wires using the GTAW-AM technique, where various pulse frequencies (from 1 Hz to 500 Hz) were employed. The finest grain structure and consequently greatest mechanical properties were achieved when the pulse frequency was either 5 Hz or 10 Hz [186]. A GMAW-AM process has also been used to manufacture components from AZ31B alloy wires [171]. Both size and volume fraction of pores in the as-built parts [171] were reported to be dramatically lower than those of pores in die-cast magnesium alloys. The GMAW-AM fabricated AZ31B alloy exhibited a higher elongation but lower yield stress than its wrought counterpart [171]. However, the UTS of the GMAW-AM fabricated AZ31B alloy was comparable to that of the wrought one [171].

2.4.6. *Copper Alloys*

Copper and copper alloys are widely used for manufacturing heat sinks, electrical wires, tooling inserts, busbars, cooling components, and electric motors due to their high electrical and thermal conductivity. Additive manufacturing allows the fabrication of complex geometries made from copper, such as internal cooling channels, while reducing the required material and shortening the manufacturing cycle. However, poor dimensional accuracy and significant porosity were observed in the AM-fabricated copper parts [270]. These problems are attributed to the rapid heat dissipation during AM resulting from the high thermal conductivity of copper. Thus, limited research has been conducted using the selected AM techniques to fabricate Cu components [174, 189, 55]. Dong et al. [189] fabricated a Cu-9 at. % Al parts using GTAW-AM, where separate pure Cu and Al wires were fed into a melt pool. The rapid solidification associated with GTAW-AM resulted in a microstructure predominately consisting of Cu_9Al_4 and $CuAl_2$ intermetallics in the as-built condition [189]. Homogenization heat treatment of the as-built parts reduced the amount of the intermetallic phases and enhanced yield stress, UTS, and elongation [189]. In another study, Shen et al. fabricated a Cu-Ni-Al part using a multi-axis GMAW-AM technique and compared it with the same part made from conventional casting. The AM-fabricated microstructure contained a lower volume fraction of K-phase precipitates but higher amounts of intermetallic phases than the as-cast one. This was attributed to the suppression of the eutectoid reaction by the high cooling rate associated with the GMAW-AM process [174].

2.4.7. *Cobalt-Chrome Alloys*

Cobalt-chromium alloys exhibit excellent wear resistance, high-temperature hardness, corrosion resistance, and biocompatibility. They are extensively used in cutting tools, gas turbines, combustion engines, surgical prosthesis, and machine gun barrels. However, their high hardness and low thermal conductivity quickly increase their temperature during cutting, making these alloys very difficult to machine. Thus, AM can be a good candidate for manufacturing Co-Cr parts. The AM-fabricated microstructure is mainly composed of Co-matrix dendrites and inter-dendritic eutectic, similar to the as-cast microstructure. However, both the dendritic branches and eutectic structure of the AM components are significantly finer than those of cast ones [137, 140, 190]. This can be explained by the significantly higher cooling rates of the selected AM techniques compared to casting. As a result of the finer solidification structure of the AM parts, the inter-dendritic eutectic carbides mostly have a lamellar morphology [137, 140, 190]. This contrasts the coarse blocky eutectic carbides typically observed in the cast microstructure [190]. This explains the higher hardness, yield stress, and UTS of the AM parts compared to their cast counterparts [190]. However, compared with wrought Co-Cr alloys, the AM-fabricated Co-Cr alloys exhibit a comparable volume fraction of carbides and hardness value [140]. Moreover, the wear resistance of AM parts under dry sand/rubber wheel test conditions was reported to be less than that of the wrought ones [140]. This is attributed to the lamellar carbides of the AM deposit creating a continuous network that is easily removed during the wear test [140]. Mechanical properties and corrosion resistance of as-deposited AM Co-Cr alloys can be enhanced by performing post-processing heat treatments. The best combination of hardness, wear resistance, and corrosion resistance was reported to be achieved when the as-fabricated component is subjected to solutionizing heat treatment without being aged [138].

2.4.8. *Tungsten Alloys*

Tungsten and its alloys are widely used in many high-temperature applications such as collimators, arc welding electrodes, rocket nozzles, and heating elements in high-temperature furnaces owing to their high melting point, low thermal expansion coefficient, high tensile strength, and good creep resistance. However, their low ductility at room temperature and high ductile-to-brittle transition temperature (DBTT) limit their ability to be fabricated. Powder metallurgy (PM) techniques are commonly used to fabricate W components. However, parts with complex geometries are challenging to manufacture by PM techniques due to the limitation in mold/die geometry. Moreover, porosity is a common defect in PM-fabricated parts due to the high melting point of tungsten alloys. Thus, AM can be considered a promising candidate for the fabrication of fully dense W components with complex geometries. Marinelli et al. [191] fabricated defect-free parts from pure W wires by a GTAW-AM technique using a front wire feeding approach. Both the grain structure and the number of structural defects (such as gas-trapped pores, keyholes, and lack of fusion) were reported to be highly dependent on the orientation of the wire feeding [191]. In another study, Zhong et al. [142] used an LDED technique to fabricate a collimation component from pure W and W-Ni powder. No cracks or pores were observed in the microstructure of the as-deposited parts [142]. Both tensile strength and elongation of LDED W-Ni alloys are enhanced by the addition of Fe, and Co [141].

2.4.9. *Defects*

This section will focus on the defects found in Ti-6Al-4V deposits across the different deposition technologies due to the lack of correlation between defects and the material or deposition system. The defects found are typically anisotropic microstructure [111, 113, 76, 199], porosity [110, 236, 206], thermal residual stress [161, 210, 111], lack of fusion [109, 202] and cracking [163]. These defects were found in LDED [110, 111, 113, 236, 109, 144, 145, 76], GMAW [163, 161, 160], GTAW [76], PTA [195, 196], and EB [199, 201, 202, 210, 203, 206, 208] deposits. Eliminating these defects is a challenge that will need to be overcome before the full commercialization of AM, especially for large-scale parts. Some of the remedies being explored are HIPing [115, 271, 272, 134, 199, 202, 273], hot rolling [180, 181], shot peening [135, 274], and cold working [275].

3. Fabrication platforms

This section introduces various considered fabrication platforms for the AM techniques discussed in Section 2, that were commonly found in the literature. For the context of this paper, an AM fabrication platform was considered as any actuated mechanical platform capable of carrying, translating, and potentially re-orienting a deposition system–such as a laser cladding head or a GMAW torch–with the desired accuracy. Alternatively, the system can be designed to translate and re-orient the substrate plate onto which components are printed or a combination of both re-orientation of the substrate plate and translation of the deposition system. The platform can be programmed to carry out deposition trajectories, including the complete integration of the deposition system, where parameters can be adjusted, and deposition can be activated and deactivated.

Various system types are reviewed in this section, and their suitability towards scalable, support-less, large-scale metal AM are assessed. Table 4 lists the platform types covered in this section and the advantages and disadvantages. Support-less printing is the aforementioned ability of a platform to re-orient a component during fabrication sufficiently to enable multi-directional deposition, which allows for support-less printing through re-alignment of the print direction with the gravity vector. The scope of the reviewed systems in this section is limited to systems capable of multi-directional deposition. It should be noted that the materials for each referenced publication are listed in Table 5. However, Mg, Cu, Co-Cr, and tungsten alloys were not mentioned in any of the referenced works and will not be included.

Multiple groups of researchers–Anzalone *et al.* [280], Nilsiam *et al.* [281], and Lu *et al.* [282]–introduced open-source fabrication platforms where the substrate plate is actuated by a parallel mechanism, which allows for 5 degrees of freedom (DOF) motion enabling multi-directional deposition. The substrate plate can be translated in all three directions (x,y, and z

Table 4: A summary and comparison of various fabrication platform types.

Platform type	DOF (dep. head)	DOF (build plate)	Advantages	Disadvantages	References
5-axis CNC	3 trans.	2 orient.	- Existing process planning methods - Good transitional technology - High component mass	- Limited scaleability - Deposition system limited to translation - Relatively expensive	[22, 23, 276, 277, 278, 279]
Parallel mechanism	0	3 trans., 2 orient.	- Cost-effective	- Limited scaleability - Limited build plate orientation angles - Limited component mass	[280, 281, 282]
Serial manipulator carrying build plate	0	3 trans., 3 orient.	- High-DOF build plate	- Limited scaleability - Deposition system limited to translation - Limited component mass	[283, 284]
6-axis ser. manip. and 2-axis positioner	3 trans., 3 orient.	2 orient.	- Deposition system orientation can be changed - Scaleable - High component mass	- Relatively expensive	[18, 36, 37, 16, 38]

Table 5: Sample of materials used in the various pieces of work discussed in Section 3

Steel	Ti	Al	Ni	Non-metals	Not Mentioned
[16, 22, 23, 36, 37] [278, 280, 282, 276, 277]	[278]	[278, 281, 285]	[278]	[283, 284, 286]	[18, 39, 279]

planes) and rotated about the two horizontal coordinates. The rotational capabilities are, however, not utilized when fabricating sample components with the proposed systems. In each system, the deposition system (a GMAW torch) is rigidly mounted above the actuated substrate plate. The system proposed by Anzalone *et al.* is shown in Figure 7b. Each of the systems is highly cost-effective at the proposed scale and type of hardware used. However, these systems have a limited build volume and re-orientation angles, making them ill-suited for larger parts. Another limitation is the limit of payload scaleability as the build plate's actuation system carries the full weight of the build.

Another system found in the literature capable of 5-axis AM is standard CNC milling systems retrofitted with a deposition system such as a GMAW or an LDED cladding head, introduced in Section 2.1 and Section 2.3 respectively. CNC milling machines have existing process planning and computer-aided manufacturing (CAM) infrastructure that can be integrated with these deposition systems, making them a popular industrial choice. This established pipeline of technology will be important in streamlining commercial 5-axis AM systems, especially for components of a limited size. Panchagnula *et al.* mounted a GMAW torch on the side of their CNC milling system's tool spindle, allowing the torch to be moved in three translational dimensions. Furthermore, the CNC milling system is equipped with a 2-axis positioner (see Section 7a), enabling the substrate plate to be tilted and rotated. The combined total of 5 DOF allows for multi-directional deposition and, therefore, the fabrication of support-less components [22, 23]. A further 5-axis metal AM platform, where a CNC milling system was retrofitted with a laser cladding system was introduced by Tabernero *et al.* and Calleja *et al.* [276, 277], with similar capabilities as Panchagnula *et al.*

In addition to the above-listed 5-axis platforms, there are also commercialized 5-axis hybrid platforms for metal AM available such as the Mazak INTEGREX i-400 AM [278] and the DMG Mori LASERTEC 65 3D hybrid [279]. Each of these two platforms is equipped with an LDED deposition system and a tool spindle. A component is first fabricated, or a feature is added to an existing component through AM. The finished component or feature is then finalized by milling the surfaces to an accurate size. This combination of additive and subtractive manufacturing is gaining popularity in the industry due to the lack of geometrical constraints of AM coupled with the surface tolerances offered by subtractive manufacturing. This offers unique capabilities that are currently not achievable with either technology alone.

Another platform that can potentially be utilized for metal

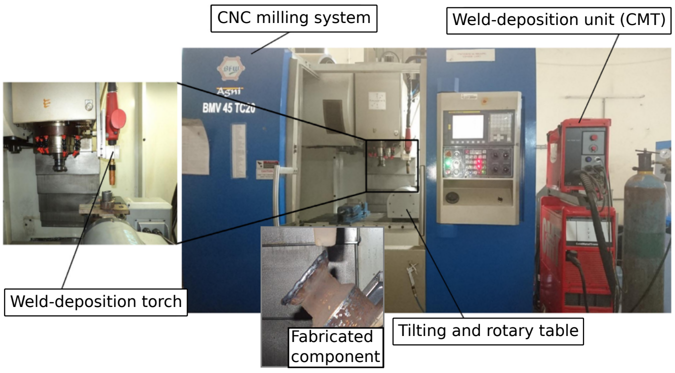

(a)

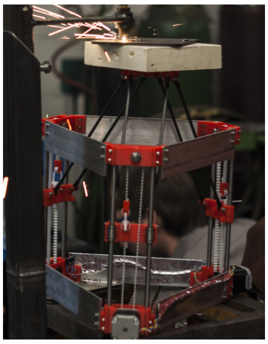

(b)

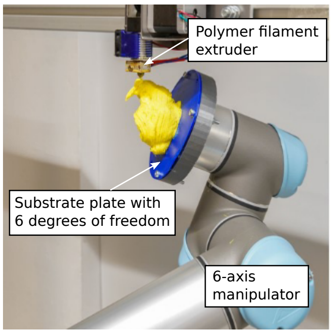

(c)

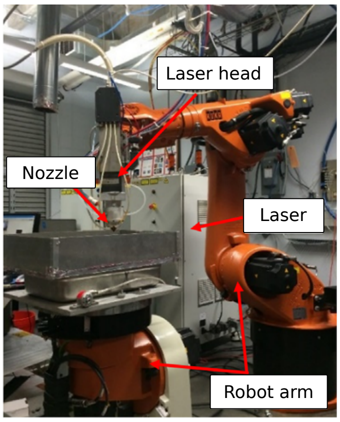

(d)

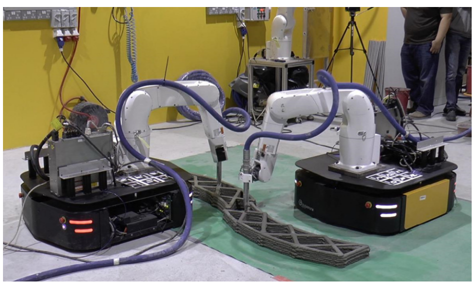

(e)

Figure 7: Examples of AM platforms with multi-directional deposition capabilities. (a) A 5-axis WAAM platform [23], (b) a parallel-mechanism-based WAAM system [280], (c) a 6-axis robotic polymer AM platform [284], (d) an 8-axis robotic LDED platform [16], (e) a collaborative multi-manipulator platform [286].

AM was first introduced by Wu *et al.* and Dai *et al.* and is shown in Figure 7c. The platform consists of a 6-axis serial manipulator and a rigidly mounted deposition system above the manipulator. The substrate plate is mounted on the tool flange of the manipulator and can be moved in 6 DOF, allowing for multi-directional deposition [283, 284]. While both Wu and Dai *et al.* utilized polymer extruders as a deposition system, simple modifications could render it to be compatible with the metal deposition systems introduced in Section 2. One inherent limitation of this proposition is that the size of the component is constrained to the maximum payload of the manipulator, possibly limiting the scalability to large metallic parts. [18, 36, 37, 38, 16, 39]

A better-suited metal AM fabrication platform uses a large-scale serial manipulator to carry the deposition system (6 DOF), while the components are fabricated on a two-axis positioner (2 DOF) such that the overall systems offers 8 DOF. These systems have various advantages over the reviewed parallel, 5-axis gantry-based, and 6-axis manipulator-based platforms. An advantage compared to 5-axis systems is that the deposition head's orientation can be changed in all three rotational directions when a 6-axis manipulator carries the deposition system. This capability to change the orientation also facilitates tangential continuity, allowing for smoother surface finishes and optimizing the feeding angle of material into the melt pool while maintaining alignment with the gravity vector for multi-directional deposition. During GMAW-based deposition, for example, specific drag or pull angles can help achieve the desired bead geometry. Another significant advantage, which has been appreciated since the 1980s for welding complex, curved contours is the redundancy of the 8-axis manipulator and positioner combination. Redundancy in the context of a kinematic system is when more degrees of freedom are available than are required to complete the desired task. Thus, redundancy implies kinematic advantages such as enhanced relative reachability and dexterity between fabricated components and deposition systems.

The coordinated motion between manipulator and positioner offers the following advantages: reduction of execution time, added flexibility in motion optimization and collision avoidance, maximization of the manipulator workspace, and the ability to track smooth corners using smooth paths [287]. Generally speaking, manipulator/positioner combinations have been used for welding applications for over 30 years. Therefore, using these platforms for DED deposition is a natural extension of robotics research, where prior research can be utilized seamlessly.

The first example of using an 8 DOF system for DED was proposed by Dwivedi *et al.*, where radial components were fabricated using multi-directional deposition. The authors used a powder-based LDED system for metal deposition [18] mounted on the manipulator's tool flange. Ding *et al.* [36, 37, 16] (see Figure 7d) and Zheng *et al.* [38] proposed equivalent platforms also using powder-based LDED as deposition systems. Ding *et al.* explored the augmentation of a 6-axis manipulator with a 2-axis positioner, totaling 8 DOF for multi-directional deposition, as shown in Figure 7d. The author eliminated the need for support structures while fabricating a propeller, which consisted of a core volume (a shaft) and radially overhanging features (propeller blades). Such a component is difficult to manufacture using conventional subtractive manufacturing [16]. Platforms utilizing arc-welding-based deposition technologies have been less explored in combination with 8-axis motion platforms than LDED-based deposition. Such a platform was used by Ma *et al.* for experimental trials with Aluminium [39]. Moreover, in a collaborative effort between the University of Alberta and InnoTech Alberta in Edmonton, Canada, a robotic large-scale WAAM platform–as shown in Figure 1–has been put in use by the authors of this work and initial research on parameter identification towards the optimization of deposition parameters is currently being conducted [62]. An interesting extension for robotic large-scale metal AM is the use of multiple mobilized manipulators, each carrying a deposition system. Research on such a platform in the area of civil engineering for fabrication of concrete components using AM has been conducted by Zhang *et al.* The researchers propose a platform consisting of two 6-axis manipulators, each mobilized by a holonomic mobile platform where a concrete deposition nozzle is mounted on each manipulator's tool flange (see Figure 7e). A holonomic mobile platform can translate in any direction (sideways or forward) without the need to change the orientation of the platform, which means that the manipulators can reach any location within the fabrication space at an optimum duration and trajectory. Zhang *et al.* identified that the most significant advantage of this platform is the ability to fabricate components larger than the reach of one manipulator. The mobility aspect of the platform extends the reach of each manipulator, significantly enhancing the scalability and duration of fabrication. The extent of the scalability can be enhanced by increasing the number of mobile manipulators to the system. Some of the associated research challenges are robot localization, multi-robot coordination (e.g., swarm intelligence) and collision-free motion planning, and robot placement accuracy and optimization [286]. While Zhang *et al.*'s proposed platform is not capable of multi-directional deposition, a multi-manipulator platform can also be augmented with a large-scale multi-axis positioning system in order to facilitate multi-directional deposition.

4. Process planning

Process planning refers to converting a 3D model of a component to an optimal manufacturing strategy prior to fabrication. An integral part of this strategy for multi-directional large-scale AM is avoiding support structures as commonly required for 2.5 DOF AM. Depending on the geometric complexity of the overhanging features, the 3D model is decomposed into sub-volumes typically consisting of a core volume and multiple overhanging features. These are then sliced into cross-sectional layers, followed by the generation of an optimized deposition tool path for each layer. An example of such a process planning sequence is shown in Figure 8 [16]. This example shows the decomposition of a propeller where a clear separation between core volume (shaft) and the overhanging features (propeller blades) can be found. For many other components, however, this separation is less obvious or nonexistent (see Figure 9).

After slicing is complete, a deposition tool path is computed that fills the required areas of each layer with material. Using a numerical model, the bead geometry (bead width and height) required to fill the layer to a predetermined height is correlated to a set of deposition system parameters, including the material feed rate, deposition system speed, and dwell times. The magnitudes of these parameter values depend on the material and deposition technology being used. This information is then provided to the fabrication platform, theoretically allowing for unsupervised deposition.

In order to fully exploit the possible advantages of large-scale robotic AM, the systems and algorithms for the automated process planning of near net shape components need to be capable of decomposing complex volumes into sub-volumes. Additionally, the algorithm must account for the multi-directional and non-planar slicing of these volumes, and the tool path and robot joint trajectory planning, including collision avoidance [288]. The substantial work that has been done towards this objective will be discussed herein. First, state of the art in volume decomposition and slicing will be reviewed (Section 4.1), followed by the established tool path generation methods for planar layers, as many of these tool path generation strategies constitute a basis for further research on tool path planning for non-planar layers. Finally, some open-source software frameworks for robot joint trajectory planning and collision avoidance are reviewed in Section 4.3. It should be noted that all of the materials that were used in the reviewed studies have been summarized in Table 6; however, Co-Cr and W were not included.

4.1. *Volume decomposition & slicing for multi-directional deposition*

Some of the first researchers to recognize the need for an advanced process planning framework capable of decomposition and multi-directional slicing of complex 3D models with overhangs were Sing, and Dutta [17]. The objective of their proposed method was to improve the surface accuracy and reduce the support volume through multi-directional deposition. The decomposition sequence is as follows:

1. choose a build direction; by default along the component's Z direction to avoid collision of the deposition head with the table,
2. identify and decompose overhanging features (often referred to as "unbuildable structures" in the literature) in build direction,
3. determine the build direction for each sub-volume, and
4. sequence and slice each sub-volume along its computed build direction.

At the core of the approach is a recursive volume decomposition scheme meaning that overhanging features within sub-volumes are also identified. The performance of the proposed process planning framework was shown on two example 3D models, but no components were fabricated. Dwivedi *et al.* proposed a framework for automated process planning for LDED [18].

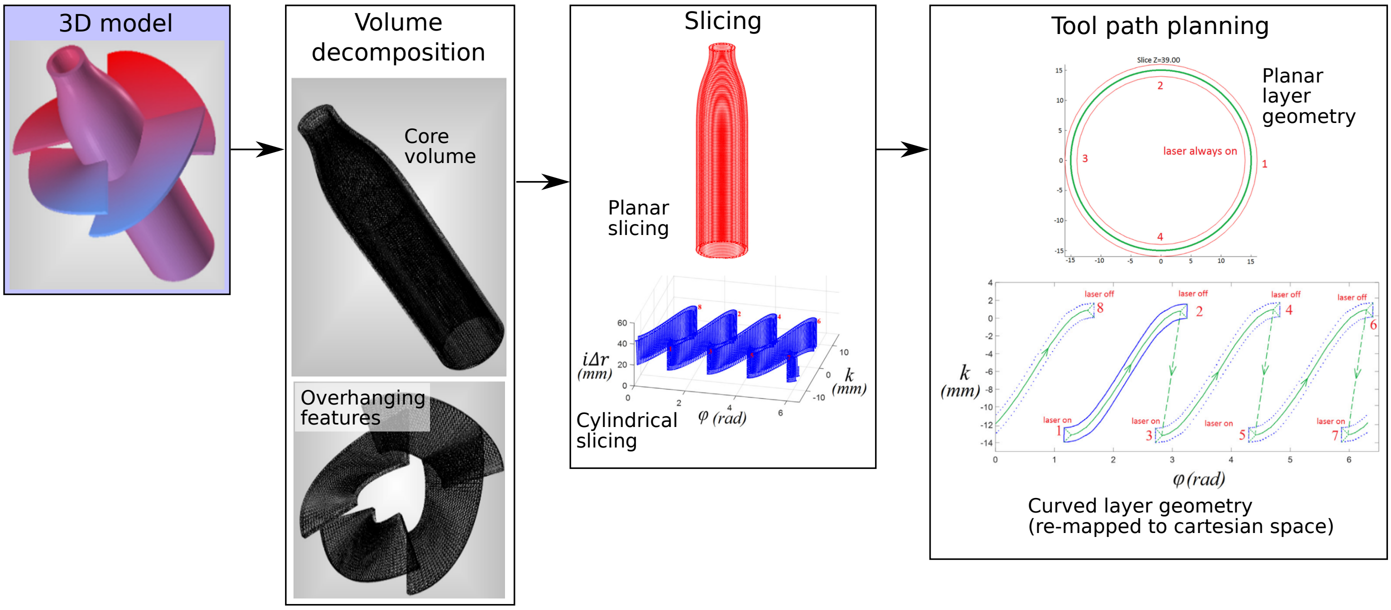

Figure 8: An example of a process planning sequence on a 3D model of a propeller including volume decomposition, slicing and path planning of each sub-volume. (Image source: [16])

Table 6: Materials used in the various pieces of work discussed in Section 4

Steel	Ti	Al	Ni	Mg	Non-metals	Not Mentioned
[16, 289, 290, 291, 292, 47, 49] [293, 294, 19, 48, 295, 39]	[293]	[293]	[293]	[293]	[288, 283, 284, 296, 24] [297, 298, 299, 300]	[39, 17, 18, 17, 301, 289, 302, 303, 304] [305, 306, 307, 308, 309, 310]

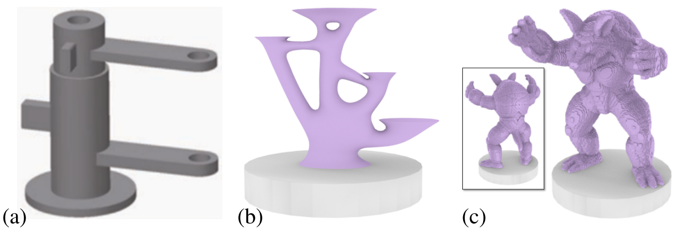

Figure 9: Examples of 3D models of varying complexity with a) a radial component with easily separable overhangs [289], b) and c) more complex components with less clearly separable overhangs [284].

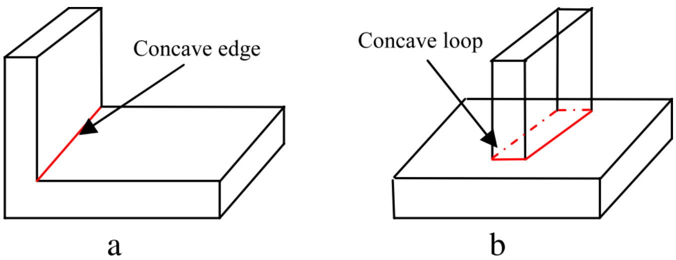

Figure 10: Schematic representations of a) a concave edge and b) a concave loop as defined in [290]. (Image source: [290])

The process planning framework is based on first-order logic and a knowledge base consisting of rule and fact attributes represented by a semantic tree structure. The authors of the study successfully verified their framework on a radial component consisting of 5 helical blades. Ruan *et al.* proposed a method using the centroid axis of a component to compute the deposition direction to produce collision-free slicing directions for multi-directional deposition [291]. The basic tasks are defined as

1. centroid axis computation and formation, and
2. collision-free multi-axis slicing based on the centroid axis.

The detection of change in build direction–and therefore slicing direction–is based on the degree of shift from the centroid axis. The slicing algorithm can produce layers of non-uniform thickness, thus requiring the deposition system to be capable of producing beads of varying geometry. The algorithm was verified on a 3D model of a hinge with overhangs on a multi-axis LDED fabrication platform. Ren *et al.* identified limitations with the previous centroid-axis-based decomposition algorithms for certain corner cases of axis-symmetric overhanging structures where no shift in the centroid axis occurs. Thus, an algorithm combining the centroid axis-based and boundary-based decomposition methods–where concave edges and loops marking the interface between core volume and overhanging feature (see Figure 10)–of the type as previously proposed by Singh and Dutta [17] was introduced [290]. Furthermore, the authors pro-

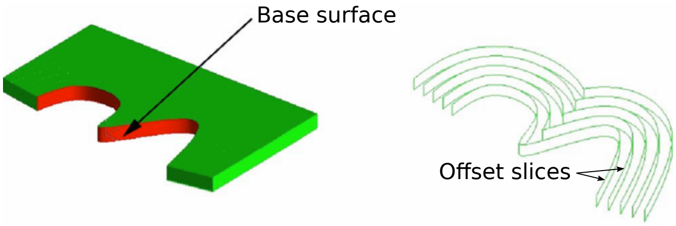

Figure 11: The concept of offset slices as introduced by Singh and Dutta [301]. The offset slices follow the contour of the non-planar base surface where each offset slice is equidistant to the previous one. (Image source: [301])

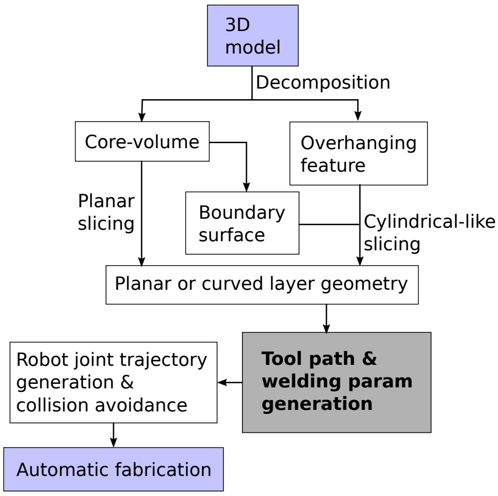

Figure 12: Flowchart of an example process plan similar to the one devised by Ding *et al.* for propeller fabrication [16].

posed a method for representing layers of non-uniform thickness by further decomposing the non-uniform layer into uniform sub-layers of a smaller cross-section than the parent layer. The algorithm was verified by fabricating a turbine wheel with a conical shaft and winged blades on an LDED platform.

In order to further improve non-planar interfaces between a core volume and overhanging feature, Singh and Dutta further extended their previous work on multi-directional deposition [17], by introducing so-called offset slices, which are essentially non-planar layers [301]. The concept of offset slices is illustrated in Figure 11. If the base surface is non-planar, which is frequently the case for radial components with overhanging features, the build quality of the overhanging features can be significantly improved when each layer follows the same contour as the core volume and subsequently the previous layer.

In order to simplify process planning and fabrication of special cases of components with overhanging features containing holes (see Figure 9a), Ding *et al.* proposed a framework that fills all holes and protrusions within the 3D model prior to decomposition [289]. The volume decomposition itself is boundary-based, whereas, with previous algorithms, concave loops and edges are detected. After decomposition, each sub-volume is sliced into planar layers according to the identified build direction. The framework was not verified experimentally. Furthermore, due to the hole-filling operation prior to decomposition, additional post-processing is required to drill the holes.

Ding *et al.* introduced a process planning framework for radial components such as propellers or impellers [16], shown in Figure 12. The decomposition algorithm is based on silhouette edges, as first introduced by Singh and Dutta [17], and Dwivedi *et al.* [292]. The algorithm is similar to previously proposed boundary-based algorithms as it looks for concave edges and loops on the core volume. Slicing is divided into two steps (see Figure 8):

1. planar slicing of the core volume, typically a cylindrical volume for radial components and
2. mapping of the overhanging feature's curved geometry from a cylindrical to a cartesian coordinate system to allow for a planar representation of each curved layer, similar to the principles proposed by Singh and Dutta [301].

The process planning framework was verified on a 8-DOF robot LDED platform (see Figure 7d) by fabricating the propeller model shown in Figure 8.

It should be noted that all of the frameworks for process planning reviewed up to this point can only process components where the overhanging features are sharp concave edges or concave loops (see Figure 10), meaning that they are distinguishable from the core volume. The works reviewed in the following, however, propose process planning algorithms and frameworks designed for volumes with non-sharp edges that are more difficult to decompose (see Figure 9b and Figure 9c). Wu *et al.* introduced an advanced volume decomposition algorithm capable of processing volumes that are not composed of a distinguishable core and overhanging volumes (see Figure 13a) [283]. The decomposition algorithm consists of 3 major steps as illustrated in Figure 13:

1. *Coarse decomposition*: A skeleton is generated based on a mean-curvature flow algorithm (see Figure 13b) followed by the computation of a distance metric–the shape diameter function (SDF)–between volume boundary and skeleton (see Figure 13c) and partitioning the mesh using the distance metric based on [302]. The partitioning algorithm identifies significant differences in the SDF and creates a boundary plane where the change occurs. When considering the bunny model, a significant change in SDF can be found at the bunny's neck, ears, and tail.
2. *Sequence planning*: A graph is constructed that defines the preliminary build sequence–nodes are the sub-volumes–and the print orientation for each sub-volume is determined (see Figure 13d). The preliminary build sequence is $A \to B \to C \to D \to E$
3. *Constrained fine tuning*: The decomposition is refined and re-configured to satisfy manufacturing constraints (see Figure 13e and Figure 13f). For example, the bunny tail as labelled B in Figure 13d can not be manufactured with the platform shown in Figure 7c due to inaccessibility. It, therefore, needs to be merged with A. In addition, $A*$ needs to be separated into H and K since the belly of the rabbit is an overhanging feature.

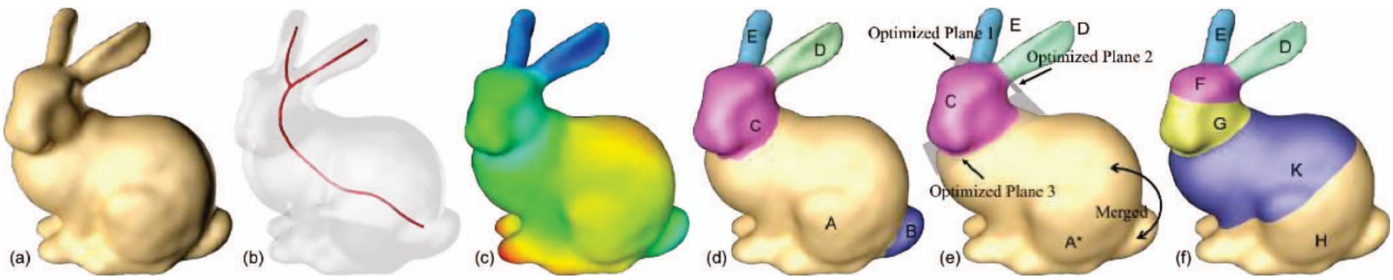

Figure 13: The volume decomposition algorithm proposed by Wu *et al.* [283] with a) the input 3D model, b) the extracted skeleton, c) the shape diameter metric (distance of every point to skeleton), d) the result of initial decomposition and sequence planning, e) after merging (B into A), and f) the final result after fine decomposition to ensure manufacturability. (Image source: [283])

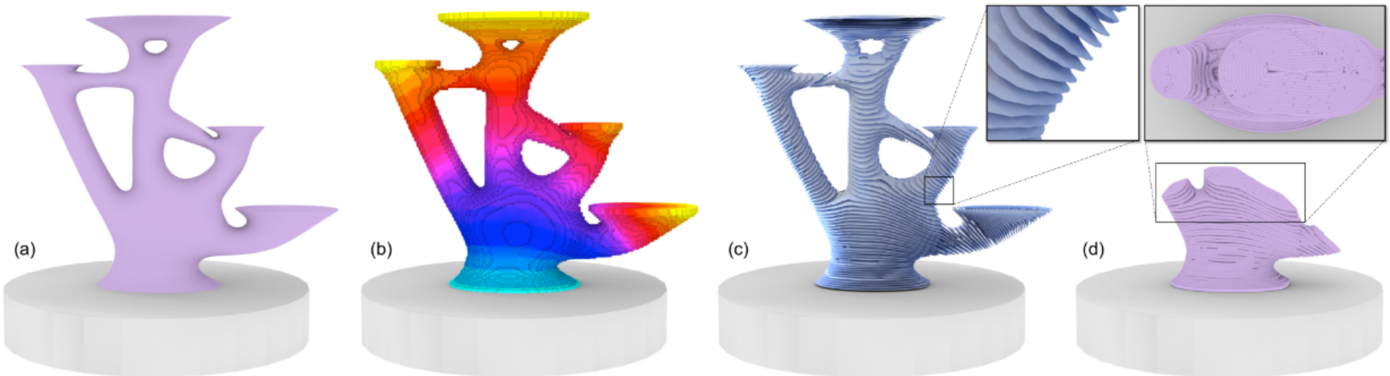

Figure 14: The volume decomposition algorithm proposed by Dai *et al.* [284] with a) the input 3D model, b) after voxel discretization and voxel sequencing where the color scheme represents the fabrication sequence by layer, c) generated curved layers based on (b), and d) a detailed view on a computed tool path. (Image source: [284])

The decomposition algorithm was verified experimentally on a robotic AM platform equivalent to the one shown in Figure 7c.

One limitation of Wu *et al.*s work is that it relies on planar layers, which imposes constraints on the manufacturability of more complex components (see Figure 9c). Dai *et al.* proposed a novel method utilizing curved layer decomposition relying on dimensionality reduction [284]. The algorithm is separated into the following steps as illustrated in Figure 14:

1. Discretization of the input model into a voxel grid–a discretization into small cubes–where the voxel dimensions are determined by the deposition system's resolution (Figure 14b). This is done to reduce the computational load on the following steps since the volume decomposition of the input model is posed as a global search problem.
2. Sequencing of the voxels to obtain a sequence of voxel accumulation representing the flow of fabrication. By iterating over all voxels, satisfying manufacturing constraints can be significantly simplified. The color scheme shown in Figure 14b represents the voxel sequencing by layer.
3. Computation of each curved layer while avoiding voxel aliasing (see Figure 14c).
4. Computation of a tool path for each layer using the method introduced by Zhao *et al.* and based on Fermat spirals [296] (see Figure 14d).

This algorithm was also verified experimentally on a robotic AM platform equivalent to the one shown in Figure 7c. The limitations of the algorithm identified by the authors include the reliability of thin-feature deposition, fabrication errors due to the used hardware, and voids in the filling patterns of the tool path planning algorithm.

Despite the limitations of the frameworks and algorithms proposed by Wu *et al.* and Dai *et al.*, their works contain important contributions to process planning of complex models with significant adoption potential to metal AM.

4.2. *Tool path planning*

Once the component has been decomposed and sliced into cross-sectional layers, the optimal path to accurately deposit the material within the boundaries of the cross-section is computed. This process is known as tool path planning. An optimized deposition path planning strategy results in dense parts with minimized residual stress, free of any porosity, better control of anisotropic microstructures, mitigation and minimization of heat accumulation, geometrical accuracy, and a smooth surface finish [24]. In order to develop an optimal deposition path planning strategy, features that are unique to the various kinematic systems and deposition technologies (consistency of deposition, motion delay, dynamics, lag) need to be considered.

Notably, the varying delays and inaccuracies in deposition system motion (especially for larger systems with increased mass) and material deposition (material feeding, melting) that are difficult to predict can cause unwanted variations on the rate of deposition and therefore complicate path planning significantly [47]. Inter-layer dwell time, start-stop minimization, smooth directional changes, as well as minimization of weld path crossovers, are some of the commonly adopted strategies to mitigate these complications [47, 49, 293]. Towards the development of an optimized path planning strategy, Ding *et al.* identified various requirements for WAAM such as geometrical accuracy, minimization of start-stop points, minimization of rapid directional changes caused by sharp corners in every tool-path pass, and simplicity allowing for fast implementation [47].

Ding *et al.* reviewed various path planning methods with respect to their suitability for WAAM, using the above-mentioned evaluation criteria. Among the reviewed path planning algorithms are: Raster [303], Zigzag [304, 305], Contour [306, 307, 308], Spiral [297, 309], Fractal Space Filling Curve [298, 310], Continuous [310, 299, 300] and Hybrid (Combination of contour and zig-zag) [294, 19]. However, Raster (see 15a), Zig-zag (see 15b), Contour (see 15c), Fractal (see 15e) and Spiral (see 15f) should be entirely avoided for metal AM due to the many issues listed by Ding *et al.* [47]. Raster and Zig-zag suffer from poor outline accuracy due to discretization errors on non-parallel edges. Contour generates many disconnected closed curves, therefore violating the requirement to minimize start-stop points. Fractal Space Filling Curve involves many path direction change motions, violating the requirement to minimize rapid directional changes. Finally, the Spiral method is only suitable for unique geometrical models that are convex [47]. Hence, these methods will not be reviewed in detail in this section.

The Hybrid method (see Figure 15h) is a combination of the Contour and Zig-zag methods in that first, the contour of the layer boundary is traversed followed by filling the interior of the layer with the Zig-zag and Contour method (see 15d). As this method combines the advantages of the Zig-zag and Contour methods, it is particularly promising for WAAM as it meets both the geometrical accuracy and surface quality. According to Ding *et al.*, the Hybrid method is still insufficient due to the increased amount of tool-path passes and tool-path elements [47].

Ding *et al.* therefore proposed a novel tool path planning method intended to address the limitations of the previously proposed methods [47] and to conform with the aforementioned requirements: geometrical accuracy, minimization of start-stop points, minimization of rapid directional changes, and simplicity of implementation. The method is henceforth referred to as Convex Polygon Generation (CPG, see Figure 15i). In order to generate a set of simpler convex or monotone sub-polygons, and to simplify the implementation of path generation for each sub-polygon, a polygon decomposition algorithm first decomposes each 2D slice via a *divide-and-conquer* strategy. Then the Hybrid path planning method is used for tool path generation due to the aforementioned advantages of this planning method. After tool paths are generated for each sub-polygon, the sub-paths from each sub-polygon are connected into a closed curve that spans the entire layer, thus minimizing start-stop points [47]. This algorithm extends the Hybrid path planning method to polygons with an arbitrary complexity through convex polygon decomposition. As this method, however, also utilizes the Zig-zag method for space-filling, voids can still occur [47, 49].

To address the issue of voids while retaining geometrical accuracy, Ding *et al.* proposed a method based on Medial Axis Transformation (MAT), or also referred to as skeletonization, as depicted in Figure 15j [48]. MAT was first proposed by Blum to describe shapes [311] by generating tool paths in a contour-like fashion from the center outwards along a skeleton to the boundary of the geometry. First, the skeleton or the branch lines are generated, followed by the generation of loops representing the tool paths at a given step-over distance, which is the distance between passes representing the resolution of the deposition system [48]. With this method, the occurrence of voids is minimized. However, there are some disadvantages, such as start- and stop points and discontinuities at the geometry boundaries and deposition beyond the geometry boundaries [49]. While these deficits can be mitigated by post-process milling, they essentially limit the MAT path planning method to hybrid manufacturing.

Further iterating on their previous work with the objective of addressing the deficits raised with MAT, Ding *et al.* proposed adaptive MAT [49]. The difference being that the tool-path elements are designed so that the contour of the geometry boundary is followed and discontinuous path segments are minimized (see Figure 15k). Benefits of adaptive MAT include the capability of generating continuous tool-path elements and following the geometry contour, void-free layers, good geometrical accuracy, and thus minimal post-milling, and suitability for thin-wall structures. For adaptive MAT to produce void-free deposition, the bead geometry must be able to be varied in-situ. To facilitate bead geometry adjustment, Ding *et al.* developed a Neural-network-based model that takes the desired bead geometry as an input and outputs welding parameters that significantly influence the bead geometry. Moreover, the adaptive MAT algorithm is experimentally validated using the proposed deposition model [295].

In summary, some of the variants of Contour-based algorithms such as Hybrid, CPG, and adaptive MAT are preferred over raster or pure Zig-zag algorithms since they are more suitable for thin wall structures and allow for improved geometric accuracy, void-free deposition, and minimization of start-stop discontinuities in tool paths. Among the more suitable tool path planning methods, adaptive MAT is preferable from the aspects of void-freeness and accuracy if in-situ bead geometry adjustments are possible or feasible for a given deposition system.

A further tool path planning method specifically designed for the particular case of thin-walled structures with varying thickness was proposed by Ma *et al.* [39]. Adjustment of the wall width is achieved through a weaving trajectory where the weaving amplitude is the same as the width of the thin wall. After computing the skeleton of the polygon, the centerline is then obtained (see Figure 15l), which constitutes an approximation of the polygon's median axis. During deposition, the torch weaves about the centerline in a triangular way, as illustrated

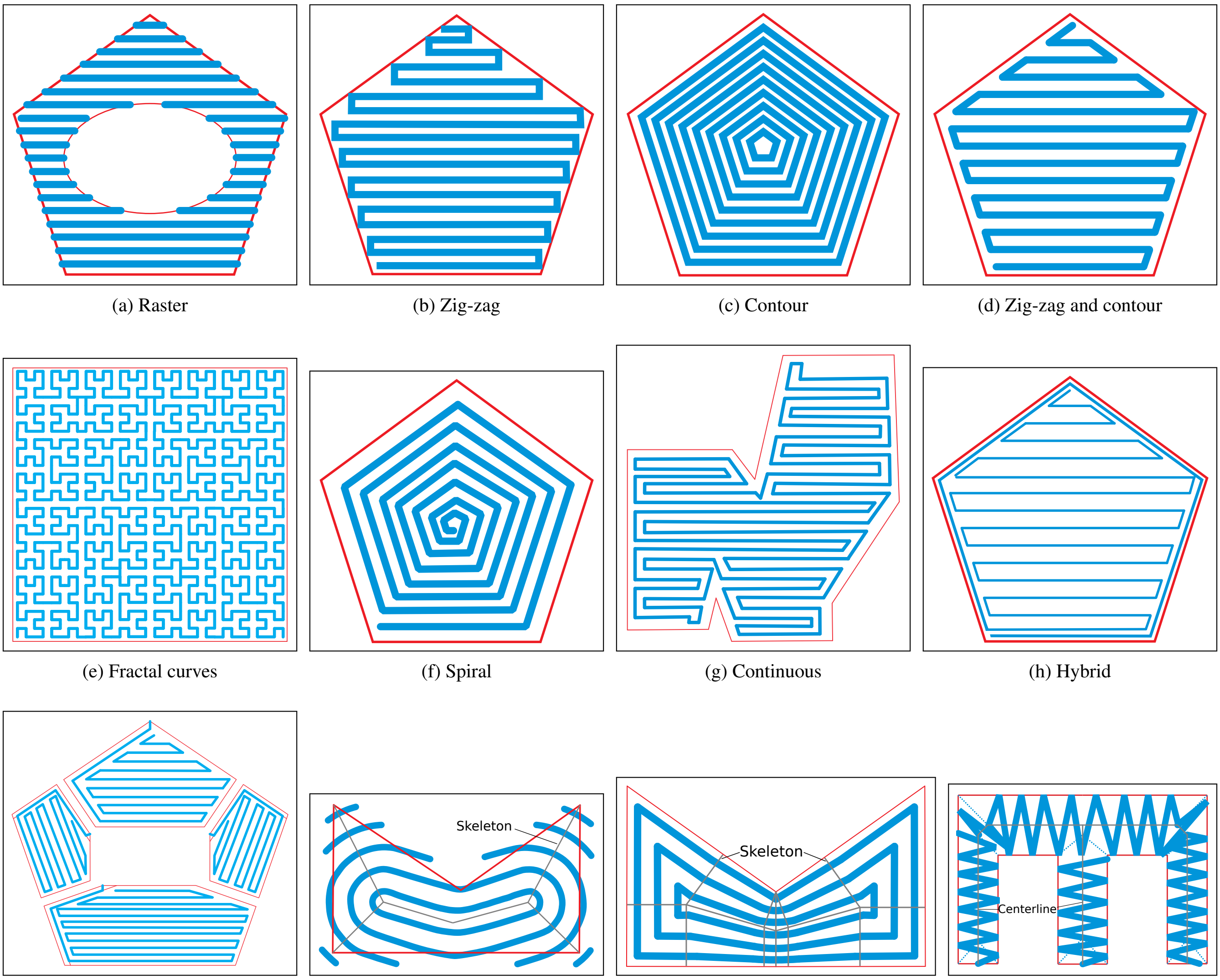

(a) Raster (b) Zig-zag (c) Contour (d) Zig-zag and contour

(e) Fractal curves (f) Spiral (g) Continuous (h) Hybrid

(i) CPG (j) MAT (k) Adaptive MAT (l) Straight skeleton and weaving

Figure 15: Different path planning methods: (a) Raster, (b) Zig-zag, (c) Contour, (d) Zig-zag and contour, (e) Fractal curves, (f) Spiral, (g) Continuous, (h) Hybrid, (i) CPG, (j) MAT, (k) Adaptive MAT, and (l) Straight skeleton and weaving deposition strategy.

in Figure 15l. The authors of the study successfully fabricated multiple thin-walled components with gradually varying wall thickness through this weaving technique.

4.3. *Software frameworks for robotics hardware interfacing & trajectory planning*

As can be seen from this section, process planning is an integral part of robotic metal AM and involves many algorithms and software components. The cascade of complex software needs to interface and exchange information efficiently to provide robust performance while simultaneously providing flexibility, modularity, and reusability to integrate new algorithms and software in a research environment. For robotic research platforms, the used software frameworks facilitating novel research need to be as open as possible. This enables maximum flexibility and customization for each software component across research groups within the toolchain and facilitates the integration of custom hardware (HW).

A popular open-source software framework and middleware providing such a software ecosystem for advanced robotics research is the Robot Operating System (ROS). ROS is leveraged for wide varieties of robotics research and provides structured messaging between software components, robot-specific tools and libraries, various visualization and convenience tools, HW abstraction, low-level device control, and tools and libraries for obtaining, building, writing, and executing code (see [312]). ROS, therefore, simplifies and facilitates robotics research and software development significantly. The ROS software package MoveIt!, for example, provides interfaces to sophisticated path planners for free-space motion and inverse kinematics solvers for industrial robot arms such as the one shown in Figure 1.

In recent years, multiple open-source software frameworks have been developed within the ROS ecosystem for the planning of complex cartesian trajectories with an emphasis on industrial robotics applications such as welding, routing, milling, deburring, and grinding. In 2015, Edwards *et al.* introduced a path planning software package called *Descartes* for semi-constrainted cartesian trajectory planning [313]. The software takes a 6-DOF cartesian trajectory that can be under-defined and is generated for any industrial application. Under-defined means, for example, that there is no rotational constraint on the rotation about the vertical axis of a welding torch. This enlarges the inverse kinematics solution space such that there are more options for the joint trajectory planner to avoid collisions.

Armstrong introduced a further cartesian path planning stack (collection of packages) called *Tesseract* for complex industrial motion planning applications with flexibility and modularity in mind [314]. The stack offers features such as fully and semi-constraint cartesian motion planning and free space planning. A significant advantage of this package, particularly towards multi-directional deposition, is its capability to plan collision-free trajectories between two moving coordinate frames, therefore enabling planning of coordinated motion between a positioner and manipulator (see Figure 1).

While there is currently an open-source robotic AM software framework available (ROS AM) [315], providing limited 2.5-DOF slicing capabilities, tool path visualization, and AM-specific message definitions, significant limitations exist. Besides being limited to 2.5-DOF AM, there is no generalized, hardware-agnostic, and computer-integrated interfacing with the hardware available since post-processors generate instructions written in a hardware-specific language that only allows for open-loop execution.

5. In-situ process monitoring, modeling and control

Commercializing large-scale AM systems will require a high degree of self-regulation and automation to eliminate the need for highly skilled personnel to operate and monitor the fabrication process. To maintain compliance to mechanical, metallurgical, and geometrical specifications and design constraints, the bead geometry, layer geometry, weld pool temperature, and cooling rate need to be controlled in real-time as the component is fabricated (in-situ). A significant proponent of this is dictated through the optimization of the operating parameters based on the material system and the proposed tool path. Changes to the systems heat input (welding current/voltage, laser power), material feed rate, and deposition system travel speed can drastically alter the geometry of the bead of deposited material and ultimately the success of the manufacturing process. During the fabrication stage, sensors and optical systems can be used to monitor measurable aspects of the deposition and use this information as feedback to control the operating parameters of the fabrication platform. This allows for better adherence to the desired tool path generated during process planning while detecting and mitigating any defects created by non-ideal tool path planning (voids, gaps).

A basic control scheme for in-situ control of metal AM processes is shown in Figure 16. Process monitoring and control of the AM fabrication platform can be divided into three categories: condition monitoring, build monitoring, and environmental condition monitoring. The first category impacts the outcome of deposition and includes the power source (arc voltage and current, laser power, etc.) for heat input assessment, material feed rate and deposition head motion speed for deposition rate estimation and evaluation, and shielding gas flow for oxidation level determination. This is achieved using electrical sensors to monitor instantaneous voltage and current, mechanical sensors for positional and feed rate estimation, and flow sensors for various fluid flow rates. The second category includes observation of the following conditions: geometric shape, build temperature, cooling rate, heat accumulation, melt pool state, and inferred metallurgical considerations. The typical sensing modalities include:

1. Optical sensors for evaluation of bead and layer geometry (profilometer, 3D scanner, charged-coupled device (CCD) & complementary metal-oxide-semiconductor (CMOS) cameras),
2. thermal sensors (infrared (IR) camera, pyrometers & thermo-couples) for molten pool condition and temperature monitoring, and overall build temperature monitoring.

Calibration and validation experiments are imperative to ensuring the functionality of the various in-situ monitoring methods. This is especially important for thermal sensors like IR cameras, where electrical sensors measure the thermal energy emitted from an object and convert it to a temperature. The emissivity, which is the efficiency at which natural objects radiate heat, must be determined to ensure that the temperature measured by the IR sensor is correct [316]. This can be done in situ using an emissivity probe or post mortem by measuring the temperature with a different calibrated thermal sensor, and adjusting the emissivity value until the temperatures match. With emissivity being a function of both temperature and surface roughness, unless extreme care is taken to validate the temperatures measured by infrared sensors, these results should be taken as qualitative [316].

Structural defects (absence of fusion, porosity, and cracks) can be evaluated by acoustic signal propagation measurement inside the part or even radio-graphic reflections. The third category can entail arc image, O_2 concentration, and acoustic propagation in the working area [293, 47, 49]. It should be noted that only optical and thermal sensors will be discussed explicitly in this paper. One of the main problems with monitoring and control of automated arc welding is the fusion of all the data in association with machine, component, and environment, which are time-variant and nonlinear transduction quantities [69, 48, 70].

Some literature review works on in-situ sensing and control have previously been published. Tapia and Elwany reviewed multiple sensors primarily utilized to conduct studies on monitoring of metal-based AM [317]. Purtonen *et al.* also presented an overview of monitoring and control techniques used laser-based metal AM [318]. Everton *et al.* reviewed AM in-situ monitoring methods, research in the field of in-situ analysis for AM processes, and state-of-the-art for major process control technologies of metal AM [319]. They remarked that monitoring has been done mostly for process understanding rather than

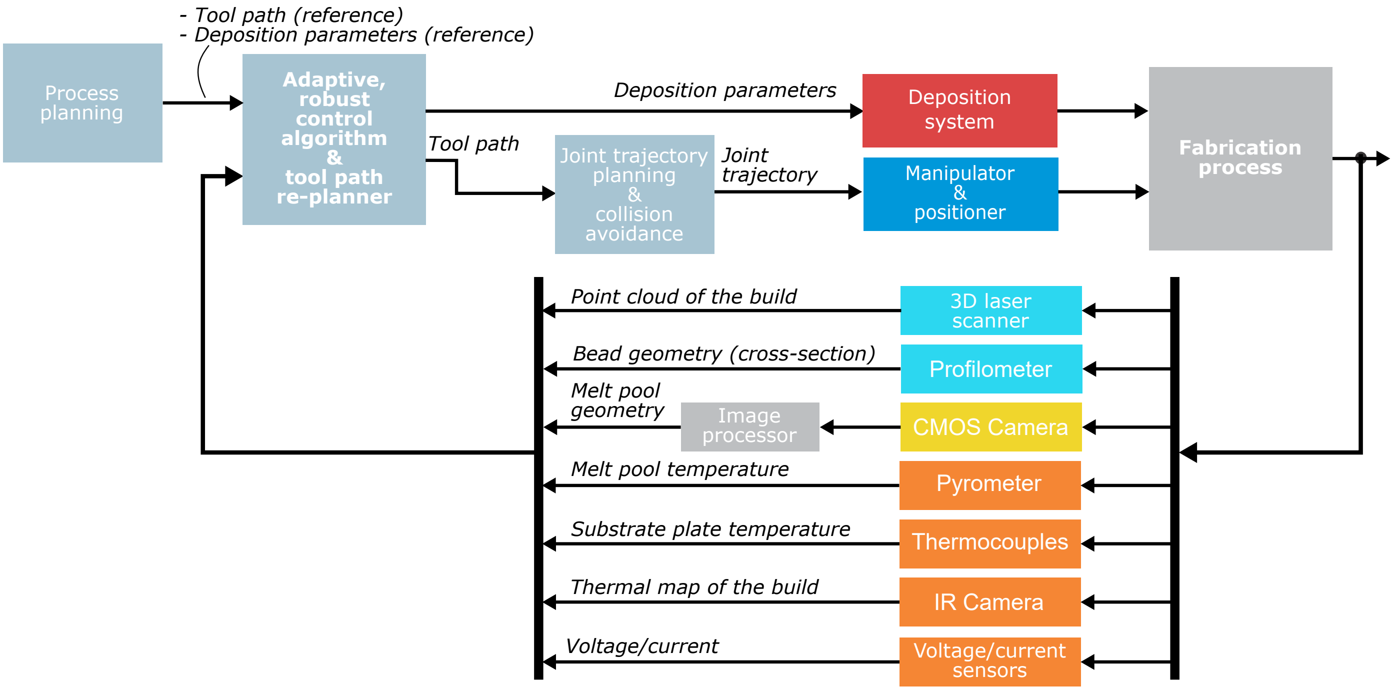

Figure 16: A basic monitoring and control schematic for robotic metal AM processes.

identifying defects and part discontinuities. This highlights the lack of holistic understanding of the implications that various processing conditions have on the metallurgical quality of the deposit, on both the macro and micro scale. Although process understanding is a step in the right direction, the collaboration between the different engineering disciplines involved in AM can extend the capabilities of process monitoring and control modalities to correlate the quantifiable manufacturing conditions to optimize metallurgical and mechanical properties.

This section will review how monitoring technologies are used in AM to provide feedback to the control algorithms that adjust bead geometry, melt pool temperature, and the layer surface geometry. More specifically, the physical monitoring systems and control algorithms proposed for wire-and-arc-based, plasma-based, and laser-based deposition technologies will be outlined and discussed. This will be followed by the work that has been done on the mathematical and physical models of these systems and how the two fields are coupled. It should be noted that due to differences in the physical nature of the different heat sources, not all of the sensor and optical systems are compatible with both laser and arc deposition systems.

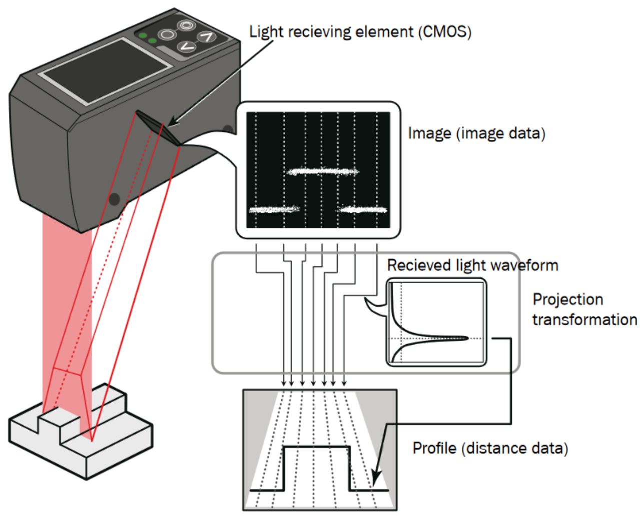

Figure 17: The operating principle of a laser line scanner (profilometer). (Image source: [350])

5.1. *Bead geometry*

When joining two components using welding, the need for in-situ inspection of the welding bead geometry arises from the need to detect weld defects, as these typically lead to topological variations on the surface of the bead. This need to monitor and control the shape of the weld bead also extends to metal AM as an important means to ensure the quality of an additively manufactured component during fabrication. Observing and controlling the bead's adherence to the desired geometry (width, height, and curvature) determined during process planning is essential to avoiding voids, porosity, and geometrical inaccuracy of the final build. Bead height is also important to maintain a constant distance between the deposition head nozzle and the melt pool, known as the stand-off distance. For welding techniques, the stand-off distance dictates the voltage of the system.

One of the most common sensing methods used for detecting weld defects is based on laser line scanners (also referred

Table 7: Materials used in the various pieces of work discussed in Section 5

Steel	Ti	Al	Ni	Mg	Cu	Co-Cr	W	Non-metals	Not Mentioned
[293, 47, 49, 48, 70, 317, 318] [319, 320, 321, 322, 323, 324, 325] [326, 327, 328, 329, 330, 331, 332] [333, 334, 335, 336, 337, 338, 339]	[293, 69, 317, 318, 319, 340, 341, 342]	[293, 317, 318, 319, 343, 337]	[293, 317, 318, 319]	[293, 317, 318]	[317, 318]	[317, 318]	[317, 318]	[344, 345]	[346, 347, 348, 349]

to as profilometers) that are mounted on the deposition head and observe the cross-section of the bead's geometry (height, width, curvature) almost directly after deposition [346, 347]. Profilometers are now standard equipment in the manufacturing industry for various inspection tasks due to their high accuracy ($\sim$0.02 mm), high sampling rate ($\sim$1kHz), and ability to obtain the complete geometry of the bead cross-section, thus giving direct feedback on deviations from the desired bead geometry. Moreover, as the profilometer is moved along the bead while continuously measuring the cross-section, a 3D profile of the bead can be reconstructed to analyze surface defects, voids, and gaps. The working principle of a commercially available profilometer is illustrated in Figure 17. In the following paragraphs, contributions to weld bead inspections using laser line scanning systems are reviewed.

Early work on a method for in-situ measurement of bead geometry during wire-and-arc welding using a profilometer with multiple deposited layers was introduced by Doumanidis and Kwak [320]. The bead profile obtained from the profilometer is used to validate a real-time analytical deposition model and provide feedback to a closed-loop control system for bead surface geometry control. Li *et al.* designed a scanning system and algorithms for feature extraction and dimension measurements to measure the dimensional properties of the weld, including groove width, bead width, filling depth, and reinforcement height, in root- pass and cap welding [346]. Flaws such as plate displacement, weld bead misalignment, and undercut were detected via the proposed feature extraction method. Huang and Kovacevic also designed a scanning system for monitoring the weld joint [347]. Furthermore, a computer-vision-based seam tracking controller and a feature tracking algorithm were developed for tracking weld bead features such as the width and height of the bead.

Many methods for bead geometry control utilize the above-introduced monitoring modality. However, there are also camera-based monitoring methods used for control feedback. In the following paragraphs, the literature on bead geometry modeling and control methods and algorithms is reviewed. It should be noted that the optical vision system required some neural and narrow-band filtering to remove the intensity of the arc and allow for the observation of the weld pool [348].

Iravani-Tabrizipour and Toyserkani proposed a vision-based system for in-situ measurement of clad height during LDED [321]. A trinocular arrangement of three cameras pointed at the melt pool at an angle of 120° allows for a measurement of the melt pool from all directions. In order to infer the clad height, the melt pool shape is extracted from the raw image, followed by a perspective transformation. Then, detected elliptical features are provided as inputs to a neural network, which maps the shape of the elliptical features to the clad height. Experimental results show that the authors can obtain in-situ measurements at a rate of 10 Hz and with an accuracy of $\pm$0.15 mm.

Xiong and Zhang developed a passive-vision-based method for measuring the bead geometry in-situ during multi-layer, single-track GMAW-deposition of a thin wall [348]. A schematic of the experimental setup is shown in Figure 18a. The vision system captures a side and top view of the weld pool and the solidification area after the weld pool. Basic image processing techniques such as edge detection combined with Hough transform are used to find the bead width and height. Images with overlaid bead geometry detection are shown in Figure 18b and Figure 18c. Validation experiments indicate a relative error of 5.7% between the ground truth and the vision-based measurement, which would be an error of 0.171 mm for a bead height of 3 mm. The passive-vision-based bead geometry measurement method proposed in [348] is then used by Xiong *et al.* for in-situ feedback control of the bead width [322]. The control algorithm–a segmented neuron self-learning Proportional Summational Differential (PSD) controller–takes the measured bead width as feedback and adjusts the torch travel speed to keep the bead width constant across layers. Disturbances in the bead width are due to variations in the shape of the previous bead and the slumping of subsequent layers caused by accumulating heat. The experimental results show that better consistency in the bead width can be achieved across layers.

In a further application of the vision-based bead geometry measurement method introduced in [348], Xiong and Zhang propose a controller for layer height control [323]. This control algorithm–an adaptive, model-based controller–takes the measured bead height as feedback and adjusts the deposition rate to achieve a constant nozzle standoff distance and, by extension, a constant bead height. The adaptive component of the controller is based on a delayed first-order model and a controlled autoregressive moving average model to describe the relationship between deposition rate as input and nozzle standoff distance as output. The control system is comprised of two loops: an inner loop for conventional feedback control of the nozzle standoff distance and an outer loop for online identification of the process parameters and adjustment of the inner loop controller parameters. Noted bead height disturbances result from inter-layer temperature and shape fluctuations of previous layers due to heat accumulation. It is shown experimentally that the control algorithm maintains an accuracy of $\pm$0.5 mm.

In a further study, Xiong *et al.* used their previously developed vision-based bead geometry sensing system combined with their previously proposed segmented neuron self-learning PSD controller for adjusting the layer width [324]. The control variable in their scheme is the torch travel speed, and a first-order process model is considered. The experimentally verified range of layer width was 6 to 9 mm and a mean absolute error

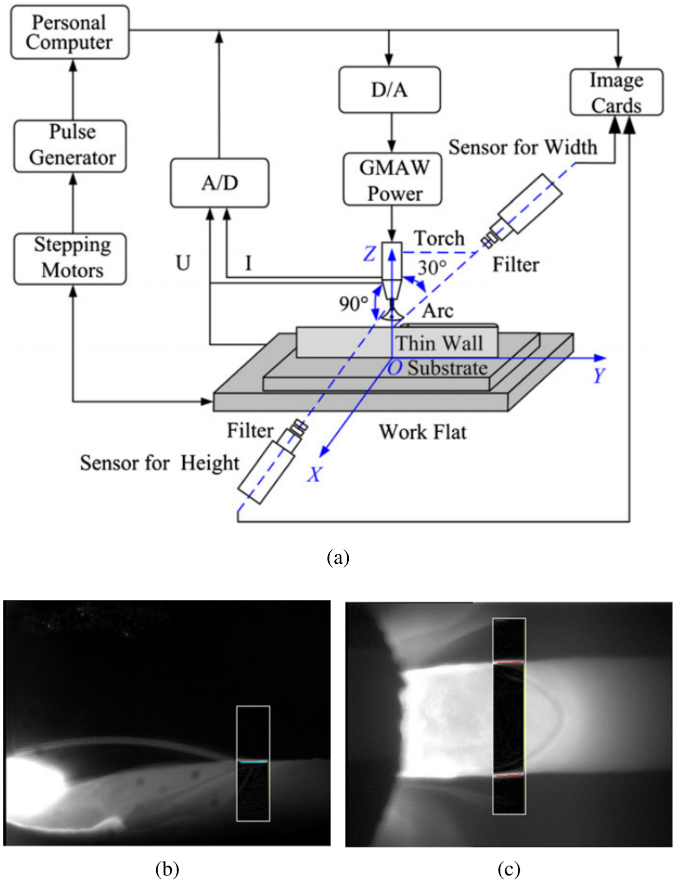

Figure 18: The vision-based method of bead width and height measurement as proposed by Xiong *et al.* [348] with a) a schematic representation of the experimental setup, b) detected bead height and c) detected bead width. (Image source: [348])

of 0.5 mm.

In order to address the issue of poor accuracy when depositing beads with sharp corners, Li *et al.* also proposed an adaptive process control scheme capable of guaranteeing a uniform bead morphology during WAAM. In their scheme, the tool path is divided into several segments at sharp corners [285]. For each segment, a permissible travel speed, subjected to the dynamic constraint, is selected, and the wire-feed speed is set beforehand according to a process model. In this method, matching the travel speed and the wire-feed rate leads to a uniform bead morphology among different segments.

Many of the above-reviewed control schemes use models for adaptive control of the various geometric features of the bead. Models that can be used in real-time to predict the bead geometry and related factors are important for adaptive and robust control schemes. As a requirement, these models must supply prediction updates at high sampling rates. Some suitable modeling methods for real-time control are reviewed next. Pal *et al.* developed models for the prediction of the bead geometry using a Back Propagation Neural Network (BPNN) model, a Radial Basis Function Network (RBFN) model, as well as a regression model [325]. The bead width and height were predicted as a function of process parameters, including pulse voltage, back-ground voltage, pulse duration, pulse frequency, wire feed rate, and RMS welding voltage and current. Akkas *et al.* designed an Artificial Neural Network (ANN) and neuro-fuzzy system for predicting the bead thickness and penetration area while providing the three welding parameters of voltage, current, and speed [326]. Ding *et al.* trained an ANN model to specify welding parameters according to the bead width and height during WAAM applications [343]. Li *et al.* proposed a predictive ANN for specifying the offset distance of the beads in order to control the real center distance of the side-by-side beads according to the desired values of bead width, height, and the center distance between the beads for the WAAM process [327]. Ríos *et al.* presented an analytical process model which correlates layer width and height with the WAAM process parameters [340].

The limitation of camera systems such as the one introduced in [348] is that the measurements are obtained at a low sampling rate due to the need for computationally intensive image data processing. A further drawback caused by the increased processing time is a significant measurement time delay, which is not feasible for fast-response control algorithms. Profilometers are much more suitable for bead geometry measurement since the bead geometry is detected directly and does not have to be extracted from the pixel data of an image, thus increasing the sampling rate. They can also provide a 3D profile of the bead at higher resolution, which improves the accuracy of prediction algorithms that use historical data to make predictions. Many of the reviewed control algorithms that use cameras for feedback (e.g., [322, 323]) could obtain the same feedback information from profilometers at a higher sampling rate, possibly resulting in a more responsive and accurate controller design.

5.2. *Layer surface geometry*

As each layer is typically comprised of deposited beads, defects can be caused by inadequate process planning, such as inaccuracies in the overlapping model, voids caused by the path planning algorithm, parameter uncertainty, and deviations in deposition caused by the dynamics of the robotic system. Therefore, besides measuring and controlling the bead geometry, it is important to monitor the adherence of each printed layer surface geometry to the desired geometry determined during process planning and to ensure that voids and other defects are mitigated by modification of the subsequent layer's tool path. A 3D laser scanner can obtain a point cloud of the surface geometry of a deposited layer.

In order to mitigate accumulating deviations of layer surface geometry during a print using a wire-fed LDED system, Heralic *et al.* developed a method for obtaining a 3D point-cloud of the layer surface geometry by moving a profilometer across the part after the completion of each layer [341]. 3D point cloud data was used to control the layer height during the print using an iterative learning controller (ILC). A comparison between an open-loop (without deviation feedback) and closed-loop (with deviation feedback) part print shows that the ILC can suppress deviations that would lead to a failed print during open-loop printing. The authors acknowledge that some issues exist with their used profilometer model as it was not designed for welding applications.

Also, to detect deviations from a desired layer surface geometry, Preissler *et al.* devised a stereoscopic camera system using the pattern projection method for polymer AM to obtain a 3D point cloud from a top-down perspective of the layer surface geometry after the completion of each layer [344]. Although the system is developed for polymer AM, the same proposed method is also fundamentally suitable for metal AM. Preissler *et al.* then used their developed 3D scanner to compare the desired surface geometry of the current layer to the measured layer surface geometry [345]. The 3D point cloud data is sufficiently accurate to detect deviations of 0.5% that can lead to a manufacturing failure.

5.3. Melt pool temperature and geometry

The primary devices used for monitoring the melt pool temperature and geometry are pyrometers, IR, CCD, and CMOS cameras. The temperature and geometrical features of the melt pool could be used as inputs to a predictive system, such as an artificial neural network, to specify bead width and height, providing predictions for model-based predictive controllers. In addition, thermal maps obtained from IR cameras may be used for monitoring thermal dissipation, temperature gradients, and thermal cycles throughout the build and the melt pool geometry [69, 48, 70]. In this section, various proposed measurement systems and control methods that use thermal and geometrical measurements for feedback are reviewed for the various deposition technologies. First, the literature on LDED is reviewed, followed by the literature on arc-based deposition methods (e.g., GMAW, GTAW).

A method for the temperature-based measurement of the melt pool size in powder-fed LDED using a CCD camera equipped with a narrow-band IR filter was introduced by Hu, and Kovacevic [328]. The laser power and, therefore, the melt pool temperature was controlled in order to control the bead width by adjusting the size of the melt pool. Experimental results showed that it is possible to effectively control the temperature of the processing zone by adjusting the width of the melt pool by controlling the heat input and metal powder feed.

Bi *et al.* proposed in 2006 the first thorough study on the feasibility of various in-situ measurement systems for LDED, such as a photodiode and quotient pyrometer temperature control system (TCS) to measure the temperature [329]. The deposition head is shown in Figure 19. Moreover, a CCD camera, which was coaxially aligned with the laser beam through mirrors, measured the size of the melt pool during powder-fed LDED. The introduced methods were verified experimentally to be suitable for temperature control. Furthermore, the influence of process parameters such as laser power on the temperature signal was investigated. Through adjusting multiple process parameters such as deposition head travel speed, material (powder) feed rate, and laser power, it was found that the laser power shows the strongest influence on the IR temperature signal. Based on the results obtained in the previous work, Bi *et al.* then proposed a closed-loop proportional-integral-derivative (PID) controller taking temperature feedback from a pyrometer

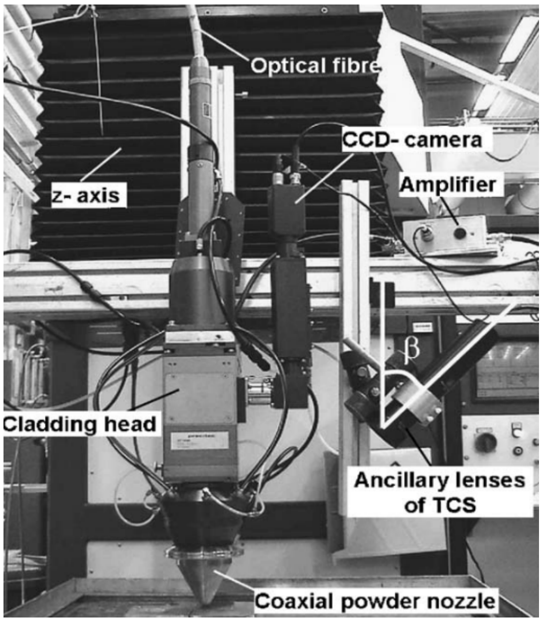

Figure 19: The experimental setup for temperature monitoring as proposed by Bi *et al.* [329]. (Image source: [329])

to control the melt pool temperature [330]. The proposed controller was able to increase the dimensional accuracy of single-track, multi-layered walls. Bi *et al.* then further proposed a compact laser cladding head with integrated temperature sensors as previously proposed in [329] including a Germanium (Ge) photodiode for measuring the melt pool temperature and a CCD camera for monitoring the melt pool geometry [331]. A PID controller was used to keep the melt pool temperature constant by adjusting the laser power. The authors were able to significantly improve the quality of an additively manufactured airfoil by minimizing the accumulated temperature through their temperature control system. Tang and Landers proposed a melt pool model based on a first-order transfer function for LDED [332]. It was found that previously proposed models were not suitable for online temperature control due to their complexity. A digital tracking controller was designed to control the process quality via a *Kalman-filtered* feedback of a temperature sensor. However, it was concluded that the controller might not perform well with multi-layer depositions due to heat transfer issues. To further improve the laser cladding process to facilitate adoption in the industry, Bi *et al.* identified key factors influencing process monitoring and control in laser-based DED [333]. A single-color pyrometer was integrated with a powder feeding nozzle to monitor melt pool temperature to identify influencing factors. Geometry, power density, and oxidation were identified as affecting the process control performance. Nassar *et al.* presented a closed-loop control architecture for controlling the path plan during LDED to optimize the build microstructure. A temperature-based controller was implemented [342]. An application of in-situ temperature sensing for control of the solidification rate and, therefore, the microstructure during powder-fed LDED was proposed by Farshidianfar *et al.* [334]. Using a CCD camera equipped with an IR filter to observe the melt pool and solidification area, the temperature gradient of the solidification area after the melt pool was obtained. The authors then proposed a PID-based controller for regulating the cooling rate, and therefore the microstructure, via adjustment of the deposition head travel speed. It was shown experimentally that the microstructure remained consistent due to the controlled cooling rate.

Doumanidis and Hardt proposed a multi-variable adaptive closed-loop controller using temperature feedback of heat affected zone in arc welding [335]. They considered a structured heat model with uncertain parameters. In addition to the layer geometry sensing via profilometer described in Section 5.1 for wire-and-arc welding, Doumanidis and Kwak also used an infrared camera to measure the temperature and geometry of the melt pool [320]. The in-situ melt pool measurements were then used to identify the parameters of a lumped-parameter model for the melt pool that models the relationship between its geometrical and thermal properties and the process parameters, including torch power, material feed, torch angle, and motion. This model was then utilized for real-time bead geometry control. In order to overcome sensory delay, a Smith predictor was used. The overall RMS error between the desired and achieved layer geometry was 0.23 mm. Wu et al. also utilized a CCD camera in combination with a narrow-band IR filter to construct a passive vision sensing system for imaging the weld pool during constant-current GTAW [336]. The images were then processed to obtain the melt pool size. Lü *et al.* proposed a multiple-input single-output (MISO) adaptive controller for adjusting the width of the weld pool during GTAW utilizing feedback of wire feed rate, welding current, and topside image of the weld pool [349]. A backpropagation neural network (BPNN) model was used to estimate the backside pool width and compared it with the desired value. Xu *et al.* focused on two issues in their study on GTAW and GMAW: capturing a clear weld image and developing an image processing technique for feature extraction [337]. For the former, a novel passive vision system taking advantage of a CCD camera with a moveable motorized filter, which could cross out disturbances of the arc light during seam tracking, was proposed. For the latter, image processing algorithms encompassing restoration, smoothing, edge detection, false edge removal, and edge scan were developed. Babkin and Gladkov introduced a new graphical method for GMAW welding parameter determination [338]. The influence of the workpiece temperature control over the geometrical preciseness of the deposited layer was highlighted. Feng *et al.* used a CCD camera to monitor the weld pool surface in GTAW [339]. The contribution was to compute the height of the mirror-like bead surface via processing of the reflection image of the reversed electrode on the bead surface, knowing its constant tip-to-workpiece distance.

6. Post-processing

As mentioned above, the microstructure is highly dependent on the local cooling rate the part experiences during deposition. Processing parameters, such as travel speed, dwell time, material feed rate, and travel direction, affect the solidification velocity and the resulting crystalline morphology [351]. The layer-by-layer variance in processing conditions results in non-uniform and transient temperature gradients throughout the build, leading to an anisotropic microstructure [110]. Thus, the mechanical properties have a directional dependency, which is undesirable for many applications. Heat treatment is used to manipulate and control the final microstructure, ensuring optimum performance when the final part is placed in service.

One of the more important heat-treating processes for AM is annealing, where the material is held at elevated temperatures for extended periods of time and then cooled at various rates. The different annealing treatments for AM deposits are shown in Figure 20. Residual stresses result from the unique thermal cycling that occurs during the AM deposition process [352]. Low-temperature annealing (T1 in Figure 20) improves atomic diffusion, allowing for dislocation motion and annihilation, relieving some of the induced thermal stresses. The significant strain induced by residual stresses can provide the driving force for the nucleation and growth of stress-free equiaxed grains, further reducing the internal stress. This phenomenon is known as recrystallization and has also been observed when stress relieving AM deposits [353]. Increasing the annealing temperature (T2 in Figure 20) to a point where all elemental constituents are dissolved in a single solid phase is known as a solution annealing heat treatment. The deposit is then quenched to prevent any diffusion or phase formation, resulting in a supersaturated solid phase. This is followed by a precipitation heat treatment, also referred to as aging, where the deposit is heated to a temperature (T3 in Figure 20) where diffusion is energetically favorable. This results in the nucleation of finely dispersed precipitates, or the formation of desirable secondary phases, improving the mechanical performance [354]. This section will outline the different heat treatments that are common for the materials discussed in 2.4. First, the conventional heat treatments will be discussed where applicable to outline each heat treatment step's purpose and give insights on how heat-treating AM parts may result in different microstructures with the same heat treatment. This will lead to the as-built microstructure for each material when using different heat sources. Then a general overview on what heat treatments have been done by other researchers, and how it changes the as-built microstructure and corresponding performance will be discussed. It should be noted that the scope of this section is limited to studies on DED. The materials that require further investigation will be identified. Furthermore, the heat treatments presented are generalized to highlight the effects the different heat treatments have on microstructure and mechanical performance. Thus, details including temperature, hold times, and cooling rates may not be mentioned. Finally, any mention of an aging process is done post solutionizing and not to the as-built structure due to the limited researchers utilizing a direct aging process directly after printing. This is thought to be attributed to the anisotropic microstructure of the as-built parts. Although there is an extended solid solution due to the rapid solidification, the nucleation of precipitates would not be homogeneously distributed throughout the part. Therefore, the mechanical properties would still

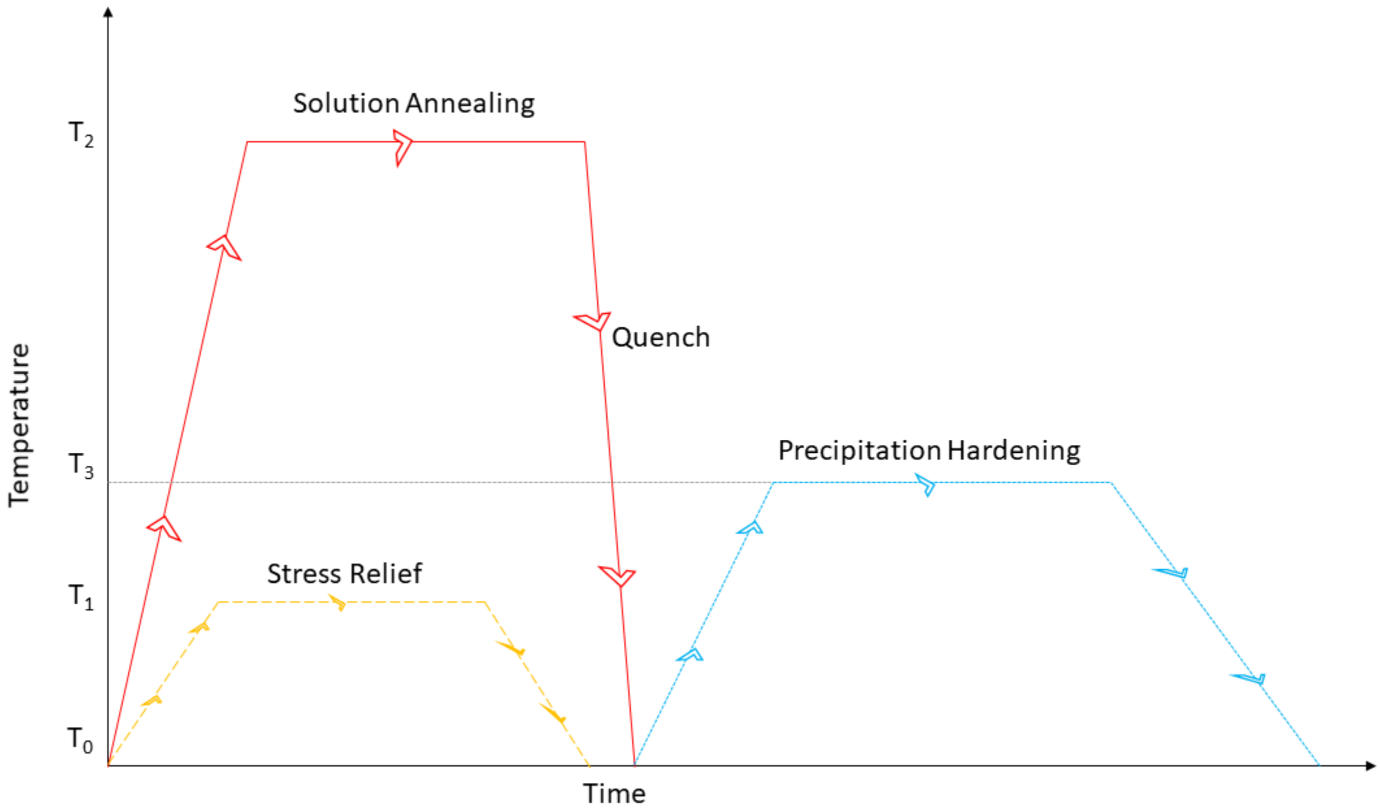

Figure 20: A re-imagining from [354]. The different thermal cycles for the heat treatments typically conducted on AM deposits, where the red solid line represents the solution annealing, the blue dotted line represents precipitation hardening, and the yellow dashed line represents stress relieving heat treatments. Note that T1, T2, and T3, as well as the hold times, heating and cooling rates are material specific, and the depicted plots are not accurate representations.

be directionally dependent.

6.1. Titanium Alloys

The scope of this section is limited to Ti-6Al-4V (Ti64) due to the abundance of studies conducted on this material system. There are other Ti alloys that are being studied, such as TC21 [355, 356, 237, 235, 357, 111], near β Ti alloys [358, 359, 360, 361] and near α Ti alloys [362], but they will not specifically be mentioned.

The heat treatment of Ti64 typically includes solution annealing and aging at a range of temperatures depending on the desired mechanical properties. Typically, the solution temperature is below the β transus temperature [363]. Lower annealing temperatures result in mostly α, with some β at the grain boundaries. The higher the annealing temperature, the higher the fraction of β that will form upon cooling. However, there is a decrease in solubility of V as the temperature increases, causing the β phase to turn to α' with quenching. If any β is retained after solution treatment at higher temperatures, a martensitic transformation to α' will be induced when plastically deformed [364]. Higher cooling rates are more desirable for Ti64 to maximize the amount of supersaturated β or α', which can be decomposed to α precipitates during aging [363, 365].

Laser-based AM techniques result in a mix of columnar and equiaxed grain morphologies, depending on the thermal history of the part. Equiaxed grains tend to form closer to the edges due to the higher thermal gradient achieved at these locations [110, 236, 111, 109]. The microstructure consists of primary β with α lamellae, which form in colonies, Widmanstätten or basketweave morphology. These colonies are more prevalent along prior β grain boundaries and close to the β transus lines from the interlayer passes.This microstructure has been seen for both powder and wire fed processes [76, 75, 145, 111, 112, 144, 146, 109, 113]. Electron beam and plasma techniques have also shown to have similar microstructures, with martensitic α' and α laths in a Widmanstätten or basketweave morphology, and a small amount of acicular α [196, 163, 161, 160, 195, 203, 202]. Defects such as pores are also prevalent in the as-built parts that cannot be removed with standard heat treatment methods [366, 113, 367, 368]. Lower annealing temperatures tend to lead to coarsening of the α laths to more plate-like morphology, with interplate transformed β [144, 146]. The α plates transform into "crab-like" morphology closer to the β transus temperature [111]. Furthermore, recrystallization of β grains begins at higher solution temperatures, while the primary α laths increase in aspect ratio and decrease in volume percent. The formation of β with solution treatment has been shown to increase the corrosion resistance of AM Ti64 parts. The coarsening of the α laths decreases strength while increasing the elongation [112, 369]. Increasing the annealing time decreases the aspect ratio of the α phase while also inducing a higher amount of precipitation of secondary α in the retained β phase [109, 203]. This causes an initial spike in strength, but this decreases as the secondary α coarsens. Increasing aging times decreases the volume fraction and aspect ratios of primary α laths while increasing the volume fraction of fine secondary α. Increasing aging time slightly coarsens the secondary α but decreases the width of the primary α, causing slight increases in the strength and ductility. Aging times over 8h will result in the globularization of the α laths. These precipitates tend to coarsen with higher subsequent aging temperatures [112]. Heat treatment has shown to reduce hardness due to grain coarsening and dislocation annihilation [111]. Under dynamic loading, heat treatment may reduce strain rate sensitivity while increasing the risks of adiabatic shear localization [109].

6.2. Ni Alloys

This section will discuss the heat treatment protocols of both Inconel 718 and Inconel 625. A summary of the standard heat treatment and corresponding microstructure will be presented for each material, followed by a tabular summary of the effects of heat treatment on mechanical performance.

6.2.1. Inconel 718

Heat treatments for industrial casting and forging operations of In718 follow solution treatment and age protocol outlined in AMS-5383D [370], and a solution treatment and aging protocol discussed in AMS-5662M [371], respectively. The high-temperature mechanical properties of In718 are attributed to the precipitation of the γ"(Ni_3Nb) and γ' ($Ni_3(Al,Ti)$), which forms in the γ matrix [372, 373]. The elements with large atomic radius are rejected from the γ phase during solidification. This causes the formation of a Nb-rich laves phase ($(Ni,Cr,Fe)_2(Nb,Mo,Ti)$) that depletes the γ matrix of Nb, preventing the formation of γ" and γ' [374]. This diminishes the ductility, fracture toughness, fatigue, and creep-rupture properties of the alloy [375]. Thus a proper heat treatment protocol must be followed to redistribute the Nb and control the cooling rate to maximize the formation of γ" and γ'. Preforming solid solutionizing alone at 980°C does not alleviate the Nb segregation in AM deposits, like that of wrought In718 alloys [168]. The partial dissolution of the laves phase promotes the formation of acicular δ phase, reducing the formation of γ" and γ'[168]. There are limited publications discussing the effects of different heat treatment protocols on the microstructure and corresponding mechanical properties of DED additive manufactured In718. Thus, this is an area of research that requires more investigation. Some of the heat treatment steps being utilized are homogenization, solutionizing, and aging [168]. Homogenization alleviates residual stress, increases grain boundary strengthening, and eliminates segregation of Nb [130, 376, 133, 377, 378, 379]. Solutionizing results in needle-shaped δ precipitation, which pins the grain boundaries impeding grain growth [168], while aging is done to precipitation harden In718 by forming γ" precipitates [379, 380]. A summary of the mechanical properties comparing conventional manufacturing methods to AM was presented by Hosseini *et al.* and is shown below in Figure 21 [381].

6.2.2. Inconel 625

The macrostructure of as-built In625 produced by AM is a range between cellular and columnar dendrites, depending on the specific thermal history of that region [170, 382]. The columnar dendritic structure has been seen to be stable up in heat treatments up to 1000°C, which becomes fully equiaxed at 1200°C [383, 384]. The high solidification rate and temperature gradient achieved during additive manufacturing are problematic for In625 due to the segregation of Nb and Mo in the interdendritic regions [385]. This causes the formation of M_6C, $M_{23}C_6$, and eutectic γ + Laves phases forming between the primary γ dendrites. There are also trace amounts of FCC γ' ($Ni_3(Nb,Al,Ti)$), BCT γ" ($Ni_3(Nb,Al,Ti)$), and orthorhombic δ ($Ni_3(Nb,Mo)$) when subject to the rapid solidification conditions experienced during laser-based AM techniques [386]. Plasma-based techniques have been shown to lead to course pockets of Laves phases, MC, and larger needle-like δ precipitates in the as-built condition [197, 387, 79]. Dinda *et al* found that solutionizing at temperatures above 1000°C cause the precipitation of γ" (Ni_3Nb) in the γ matrix, increasing the microhardness [383]. Xu *et al.* found that a solution treatment followed by aging results in partial dissolution of the Laves eutectic, resulting in the redistribution of Nb for the precipitation of the γ" and γ' precipitation improving the tensile and yield properties [387]. Hu *et al.* found that the dissolution of the Laves phase is proportional to the solutionizing temperature, causing an increase in ductility but a decrease in the tensile strength of the alloy [384].

6.3. Steels

This section will discuss the post-processing of 316L and 17-4 stainless steel. This will include the microstructural changes from the as-built condition with heat treatment and the corresponding changes to the mechanical properties.

6.3.1. 316L Stainless Steel

AM of 316L typically results in an ultra-fine and cellular columnar dendritic grain structure due to the rapid cooling rates experienced during the building process [388, 389]. There have also been reports of large amounts of anisotropic crystal orientations and grain sizes in 316L deposits from the complex thermal cycling seen in all AM techniques [390, 391]. A common defect is silicide, and oxide inclusions, which is attributed to possible oxygen contamination in the feedstock, or during the building process [390, 388, 392]. Pores are also a common defect found in AM deposits of 316L, which are detrimental to the mechanical properties and corrosion resistance [389, 393]. Saeidi *et al.* found when using a laser-based AM technique that the single-phase FCC austenitic structure seen in the powdered feedstock is mostly conserved in the as-built condition, with varying amounts of BCC ferrite. Sub-grain boundaries were found to be enriched in alloying elements such as Ni and Mo

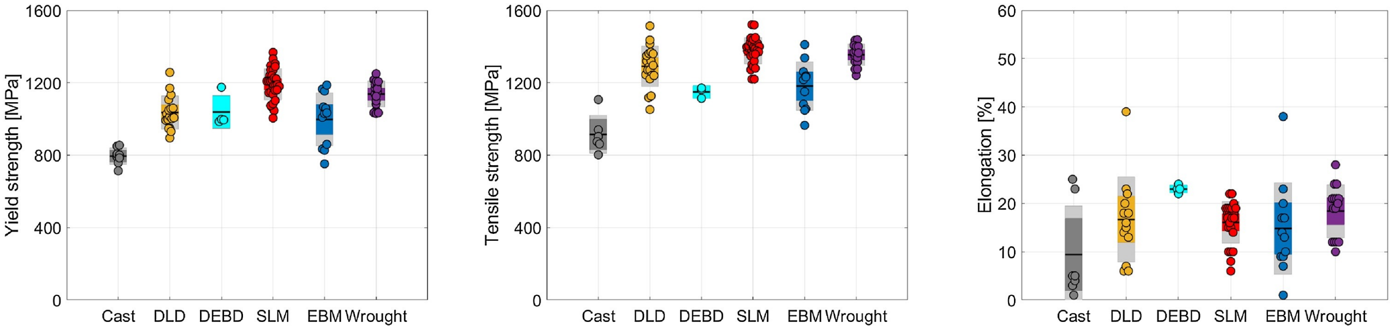

(a) (b) (c)

Figure 21: A comparison of the mechanical properties (a) yield strength, b) Ultimate tensile strength and c) elongation) of heat treated In718 alloys produced by conventional manufacturing methods (wrought and cast) and AM methods (DLD, DEBD, SLM, and EBM) [381]

[390, 391, 393, 394]. Plasma AM methods typically resulted in columnar structures of austenite (γ) of varying coarseness depending upon the location with respect to the fusion line. The inter-columnar area consisted of vermicular δ ferrite and σ (FeCr)intermetallic at the γ/δ interface [155, 159, 395]. The formation of the σ phase has also been reported in EBM, and LMD of 316L [396, 394]. The brittle σ phase acts as a crack nucleation site that could lead to decreased ductility, while both the δ and σ drastically reduce the corrosion resistance of the part [397, 398, 395]. Thus, heat treatment is typically used to increase the ductility and decrease the susceptibility to corrosion [399]. The effects of heat treatment of additively manufactured 316L using DED have not been thoroughly investigated and is an area that requires further research. It has been seen that heat treatments up to 800°C provide no apparent changes in the microstructure, but mechanical properties, such as tensile strength and hardness, tend to decrease when compared to the as-built deposit [393, 389]. This has been attributed to dislocation annihilation at the sub-grain boundaries post-heat treatment [390, 389]. Performing a homogenization heat treatment has been shown to decrease the amount of BCC δ ferrite and helps eliminate the anisotropic grain structure seen in the as-built condition [389]. However, exposure to high temperature for a prolonged period increases the average grain size, which decreases the strength while increasing the elongation of the deposit [391]. Chen *et al.* found that the σ phase can be eliminated with heat treatment of 1100°C for 1h, while the delta phase can be eliminated at 1200°C for 4h, resulting in a decrease in strength and increase in ductility and corrosion resistance [395].

6.3.2. 17-4 PH Stainless Steel

The industrial standard heat treatment of 17-4 PH hot-rolled and cold-finished bars and shapes follows ASTM A564/A564M. This standard outlines a solution treatment of 1040± 15°C for 30min, followed by several different options for age-hardening treatments [400]. The goal of the solution treatment is to control the amount of retained austenite due to its higher solubility of Cu, decreasing the amount of precipitation during the aging process [401, 402]. The solution treatment results in a martensitic phase with a lath-like morphology that is supersaturated with Cu and Cr [403]. There is also a trace amount of δ ferrite that contains some Cu precipitates [404]. The steel is then quenched and aged to cause the precipitation of Cu in the supersaturated martensitic laths [403]. The peaked age condition (H900 in ASTM A564/A564M) yields the highest hardness after aging at 480°C for 1hour, due to the coherency of the Cu particles and the retention of the large amounts of dislocations found in the martensite [405, 403, 400]. However, peak age condition is not suitable for all applications, thus implementing an overaged microstructure (H1100 in ASTM A564/A564M), with courser copper precipitates and slightly tempered martensite, is more desirable [406, 407]. The as-built structure of 17-4 produced using laser-based AM results in a fine martensitic lath microstructure, with some retained austenite in the inter-lath regions, due to the re-heating of previously deposited material during the deposition process [408, 409, 143]. Arc heat sources result in dendritic martensite, with δ ferrite in the inter-dendritic regions and small amounts of retained austenite [156, 56]. Solution treatment has been shown to convert the retained austenite to nearly 100% lath martensite [156]. Any retained austenite is attributed to the ultrafine austenite grains suppressing the transformation of austenite to martensite [410, 409]. Peak aging following the solution treatment allows for the formation of fine Cu precipitates with small amounts of retained austenite, while over aging results in an increase in the retained austenite concentration. The diffusion of austenite stabilizing elements like Cu and Ni to form precipitates decreases the martensitic transformation temperature below room temperature, resulting in an increase in retained austenite [411, 403]. Furthermore, dissolved nitrogen from the building atmosphere can drastically increase retained austenite, requiring longer aging times to achieve peak performance [226]. Many researchers have also found Mn, Si, and O inclusions that form at the grain boundaries [408, 409]. The mechanical properties after solution and aging treatment typically increase in all facets compared to the as-deposited conditions. It is also found to eliminate the anisotropic properties, typically seen in the AM deposits [156, 143]. The mechanical properties after solution and aging heat treatment have been shown to be comparable to conventional manufacturing techniques [156]. However, there is a need for further investigation on whether this is true for all DED technologies and whether this statement holds true for fatigue and corrosion properties for 17-4 PH.

6.4. Al Alloys

The post-fabrication heat treatment discussed in this section will be limited to the hypo-eutectic alloy AlSi10Mg, as it is the most studied of the Al alloys. An outline of the standard heat treatment will be reviewed, followed by the as-built and post heat treatment microstructure, and the corresponding effect on mechanical properties.

The typical heat treatment for Al-Si alloys is a T6 treatment, which is a solution heat treatment at 535°C, quench and artificial age hardening protocol at 158°C for 10h, outlined in the ASM Metal Handbook vol. 2 [412]. The solution treatment is done close to the eutectic temperature of the alloy to ensure the dissolution of Mg-containing phases, homogenize the alloying elements, and create spherical eutectic Si particles. The quench is done to preserve the vacancy and solute concentration, while aging is done to form a uniform distribution of particles, increasing the strength [413, 414]. The microstructure of as-built AlSi10Mg can consist of a columnar or a rod-like dendritic structure, depending on the heat input of the energy source [125]. However, the cellular structures can vary in coarseness depending on the spatial thermal history of the sample [123]. LMD of AlSi10Mg has also shown to form cellular and divergent dendrites [249, 120]. The dendrites are α-Al, while the interdendritic regions are eutectic Si [125, 120, 121]. There are also cases of Mg_2Si precipitates in the interdendritic regions [123, 125, 121, 415]. Laser-based techniques have shown to result in deposits that are not fully dense [121, 126, 120] and heat treatment has not been shown to alleviate this issue [125]. Heat treatment of AlSi10Mg has shown to decrease the solubility of Si in the primary α dendrites, suggesting that Si is rejected from the primary dendrites to form Mg_2Si [120]. This is due to the supersaturation of α-Al resulting from the rapid solidification and undercooling of Mg_2Si. Increasing the solution temperature or time tends to coarsen the Si particles while also decreasing the number of particles due to particle coalescence and Oswald ripening [416, 120]. Lv *et al.* studied heat treatment of LMD AlSi10Mg and found that the tensile properties increase with a T6 heat treatment[120]. The formation of a fine cellular α-Al dendrites supersaturated with Si, and the localization of Mg at the grain boundaries of the as-built samples, increase the hardness of the primary dendrites. However, the T6 heat treatment allows for the diffusion of Si, which causes a slight reduction in hardness [120]. Most publications on DED AM of AlSi10Mg use L-DED; thus, more investigation using other DED methods with AlSi10Mg needs to be done. Furthermore, additional work is required to determine the optimal heat treatment protocol for AlSi10Mg using all types of DED technologies.

6.5. Co-Cr Alloys

This section will discuss the heat treatment of AM deposited Co-Cr alloys. The focus will be on Stellite 21, and Stellite 6 Co-Cr-Mo alloys, as they are the most studied. An outline of the standard heat treatment will be reviewed, followed by the as-built and post heat treatment microstructure, and the corresponding effect on mechanical properties.

For cast Co-Cr-Mo alloys complying with ASTM F75, no standard heat treatment is included [417]. The as-cast condition of this composition typically consists of FCC γ Co, a σ intermetallic, and $M_{2}6C_{6}$ interdendritic carbides [418]. The goal of heat treatment is to homogenize the microstructure, remove cast defects and improve mechanical properties through precipitation dissolution [419, 420, 421]. The most common treatment consists of a solution treatment at temperatures of approximately 1200°C for a range of times from 1-4 hours [422, 420, 423]. However, for pin-on-disk and hardness tests, increased performance has been shown when aging is included in the heat treatment [424, 425]. Laser deposited Stellite 21 typically consists of a range between columnar and equiaxed dendrites, with a σ intermetallic, and $M_{26}C_{6}$ in the interdendritic regions [140]. WAAM of Stellite 6 results in a dendritic structure with Co-rich FCC γ primary dendrites, and eutectic γ-Co with M_yC_3 carbides [190]. Porosity has also been found in laser deposited Co-Cr-Mo deposits [426]. For LENS of Co-Cr-Mo, increasing the solution treatment time leads to decreases in size and amount of carbides due to improved kinetics for carbide dissolution at higher temperatures. This is opposite to increasing the aging time, which increases the precipitation concentration, due to decreases in solid solubility of carbide forming elements at higher temperatures [138]. Depending on the particular application of the part, the resulting microstructure from the heat treatment will yield different performance results. Longer solutionizing times with no aging may increase corrosion resistance due to high Cr contents in the matrix [425]. Variations in temperature and hold times will result in different carbide sizes, morphologies, and distributions, which will result in a range of properties [138, 427].

6.6. Mg Alloys

The use of Mg alloys for AM has not been explored in as much depth as the other alloys presented in this work. Thus, no work has been published on the effects of heat treatment on the microstructure and corresponding properties of Mg deposits.

6.7. Copper Alloys

The majority of the work on Cu alloys for DED technologies has been on WAAM of nickel aluminum bronze. Shen *et al.* deposited nickel aluminum bronze using WAAM and found that the as-built microstructure mainly consisted of Widmanstätten α phase and martensitic β phase [174, 55, 428]. Dharmendra *et al* found no retained β, but instead found κ_{II-IV} precipitates in the interdendritic regions[429, 430]. Homogenization at 900°C and quenching transformed the microstructure to equiaxed and columnar α with some retained β' and κ phases. This tends to decrease the strength and hardness but increases the elongation to failure, which is attributed to the absorption of some of the previously formed κ phases [430]. With post quench tempering, it was found that the equiaxed grains disintegrated to columnar grains, while the already formed columnar grains coarsened. Increasing the tempering temperature resulted in the elimination of the retained β and κ lamellae, and particles begin to form [174, 55]. This causes the mechanical properties to increase closer to the as-built condition. However, the distribution of κ phases becomes more uniform, decreasing the spatial variation in properties [430]. However, further increasing the tempering temperature results in significant coarsening of the κ phase, causing a decrease in performance [174].

6.8. *Tungsten Alloys*

As mentioned previously, some work has been done on DED of pure W [431], W-Ni alloys [142], W-Fe alloys [432], and tungsten heavy alloys [141]. However, no work has been conducted on how post-processing affects the microstructure and the corresponding properties.

7. Challenges & future perspectives

This work provides a holistic overview of the current state of the art in large scale robotic AM, from process planning to the microstructure and performance of the final component. Although the contributions made by the many researchers in progressing this field have been substantial in the last few decades, the technology is still in its infancy. Dr. Hannes Gostner compared AM to celestial observation at the 2019 Holistic Innovation in Additive Manufacturing (HI-AM) conference in Vancouver. He stated that AM is currently in the technological stage of Galileo's telescope and that the capabilities have the potential to be as revolutionary as the Hubble telescope. However, the boulder has a long way to be pushed before the innovative pinnacle can be crested. The lack of the field's maturity is also evident from the lack of finalized qualification and certification standards (see Table 1). The majority of the standards listed in Table 1 are currently still in draft status. Robotic large-scale AM as a sub-category within AM as a whole is highly interdisciplinary–like any other groundbreaking and paradigm-shifting endeavor. The major engineering and science disciplines involved in large-scale robotic metal AM include computer science, electrical engineering (mechatronics-, control- and systems engineering), materials engineering, and mechanical engineering. In addition, each of the process workflow stages as outlined in Figure 3 are also highly coupled. For example, a process plan consisting of a deposition system motion sequence and parameters generated by the process planning stage will affect the thermal distribution, which will affect the amount of residual stress and heat accumulation, and microstructure and corresponding mechanical properties.

Naturally, computer scientists, mechatronics-, control- and systems engineers are predominantly concerned with issues relating to their particular domains and can not necessarily appreciate the coupled challenges faced by materials-, and mechanical engineers. Therefore, a close and direct collaboration between diverse research groups is required to progress this technology further. Extensive collaboration and sharing of information will result in more holistic studies on, for example, how different path planning strategies affect the surface roughness and microstructure of an as-built component. This will give rise to new information on the different strategies that can be implemented to solve the current challenges, such as residual stress, porosity, and anisotropic microstructures. This need for collaboration has already been recognized, which has resulted in the creation of networks such as the NSERC Holistic Innovation in Additive Manufacturing (HI-AM), America Makes, and others. However, the lack of research-level fabrication of large-scale parts makes it hard to fully understand the challenges that will need to be overcome to make this a viable commercial process. It is currently speculated that overcoming the current challenges of fabricating lab-scale coupons will translate to large-scale parts. The true challenges that lie ahead for large-scale AM will not be revealed until more researchers begin to fabricate parts outside of a lab setting.

This section summarizes and discusses the largest knowledge gaps in the topics outlined in Section 2 to Section 6, followed by a holistic view of the challenges that must be overcome to commercialize large scale AM. The subsections will be structured where the challenges of each topic will be addressed, followed by the authors' suggestions on the future of research areas pertaining to the topic.

7.1. *Process planning*

Current path planning methods are generally limited to 2.5 DOF, with few systems available for 3-5 DOF path planning. 2.5 DOF systems are inherently inefficient due to support structures, requiring post-processing as well as design limitations. For large-scale parts, this entails additional manufacturing costs (such as labor and delivery time). 5 DOF path planning overcomes these challenges to a large extent but has limited industrial integration. A number of algorithms have been reviewed in this paper. While the algorithms are fundamentally suitable for metal AM, work is still required on non-planar tool path planning for metal AM where the generated tool path must satisfy the requirements identified in Section 4.2. Adaptive slicing offers an advantage in terms of reducing both the layer height and variation in material properties. This necessitates a fundamental understanding of bead deposition geometry, microstructure, and solidification modeling. Combining this knowledge with adaptive slicing will allow efficient manufacturing of high-quality parts, but this requires a significant multidisciplinary effort in material science and mechanical and manufacturing engineering. Path planning, which is a function of part geometry, directly affects heat transfer and conduction through the part being made. This results in varying amounts of additional heat in the part at any given time and build location, resulting in varying solidification rates, thereby affecting the geometry of the build and the resultant microstructure. Therefore, it is necessary to include heat transfer modeling at an earlier stage concurrent to the path planning. Current models suffer from long simulation times, inherent assumptions to reduce computational time, and a limited set of manufacturing systems and material system availability which need to be improved through further research.

Incorporation of multi-degree of freedom path planning along with considerations of the aspects mentioned above will enable in-situ modification of material metallurgy and its mechanical and geometric properties during deposition. This will truly unleash the potential freedom of design and complexity that AM processes have to offer.

Prior to fabrication, it is also necessary in many cases to calibrate the workpiece with the fabrication platform. This is especially important when the build requires coordinated motion between the workpiece and deposition system–as is always the case during multi-directional deposition. Workpiece calibration can be automated by using a 3D or line scanner mounted on the deposition head.

7.2. *Deposition Technologies*

An area where considerable research potential can be found in the powder delivery during multi-axis DED (e.g., using an 8 DOF robotic LDED platform). Currently, the LDED deposition head must always remain vertical and thus align with the gravity vector to provide ideal powder delivery. Developing methods to loosen these constraints on the deposition head orientation is necessary to utilize the full potential of an 8 DOF robotic LDED platform. Several challenges need to be overcome to enable this, including, but not limited to, modeling of powder flow at different angles to the build surface and the effect of shielding gas dispersion in the build area at non-vertical angles.

While in contrast to LDED, deposition at varying orientations is intrinsically possible with fewer limitations using GMAW-based deposition technologies. However, they are at a stage of lower maturity regarding monitoring the melt pool temperature and geometry and energy input. Sensing the melt pool in a GMAW-based deposition system is also challenging due to the rapidly and drastically changing lighting conditions due to the presence of the arc.

Work is also ongoing on the minimization of the energy input during GMAW-based deposition, where CMT technology plays a significant role. Owing to the highly controlled CMT process where it is possible to fine-tune the deposition process, significant potential for the optimization and adaptation to particular material considerations is possible. For example, in recent years, Fronius International GmbH has been developing custom synergic lines to further reduce the heat input during WAAM using CMT technology [L. Hudson and M. Zablocki, personal email and oral communications, March 2020]. Further potential for advanced research on optimizing the deposition process exists and should be considered. This necessitates in-situ and high-speed sensing of the welding current and voltage, providing important insight into the energy input into the build during fabrication. It can also provide valuable insight into the process, and the measurements themselves can be used as feedback for temperature control systems. Moreover, tremendous potential for robust sensor-fusion-based technologies exists.

7.3. *In-situ monitoring, modeling, and control*

The control algorithms reviewed in Section 5.1 for bead geometry control are relatively basic and have only been developed for and tested with single-track walls. Significant research is required to advance process monitoring and control towards the objective of robust, adaptive, and intelligent control methods that provide a sufficient degree of autonomy and robustness to unanticipated conditions during fabrication. Moreover, bead profile sensing and feature extraction have only been done for simple beads. The sensing and feature extraction capabilities need to be expanded and combined with modeling to provide accurate predictions of single beads and overlapping regions of multi-track deposition.

Substantial research potential is also apparent for advancing the area of layer geometry sensing and tool path re-planning during fabrication. The fact that during fabrication, a component is built layer by layer provides a unique insight into the current state of the build through the methods reviewed in Section 5.2. Impending catastrophic build failures can be detected, and the tool path for the following layer can be re-planned to mitigate and correct potential build failures.

Most work on temperature monitoring, and control has been done for LDED, as is apparent from Section 5.3. Particularly melt pool temperature sensing needs substantial work for arc-based deposition technologies. Heat accumulation is coupled with the deposition system travel speed and the material feed rate, which influence the bead and layer geometry. This means that if the bead geometry is adjusted (which is necessary), the heat input changes, which can modify the material composition.

Similarly, as for the layer geometry monitoring, IR cameras can also monitor the overall surface temperature of the component during the build to adjust dwell times and cooling rate of the substrate plate. This is especially important for maintaining consistent metallurgical properties.

7.4. *Materials*

Many challenges still need to be addressed in regards to materials for AM. One of the more apparent areas of exploration is expanding the number of materials available in AM. This is clearly highlighted by the chart presented in Figure 22 [433]. Although many of the materials used in conventional manufacturing are ill-suited for AM, there are still important contributions that can be made through failed experimentation. Increasing the amount of data on what materials may or may not be compatible with AM, allows for significant deductions to be made on the essential material properties a material must have to be used in AM.

Another future avenue of interest is using AM to achieve manufacturing feats that are outside the realm of possibility with conventional manufacturing. Although metals toughness far exceeds any other type of material, this comes with a poor strength to weight ratio. However, with AM, the internal structure can be altered to a lattice type, drastically increasing the strength to weight ratio. Additionally, polymer-based AM techniques could be used to fabricate these structures, which can be converted to a mold, and then cast, known as hybrid investment casting. This allows for the use of well-understood material systems in the way they were originally designed.

One of the challenges that is starting to be addressed is the current material selection for AM [434]. The current materials

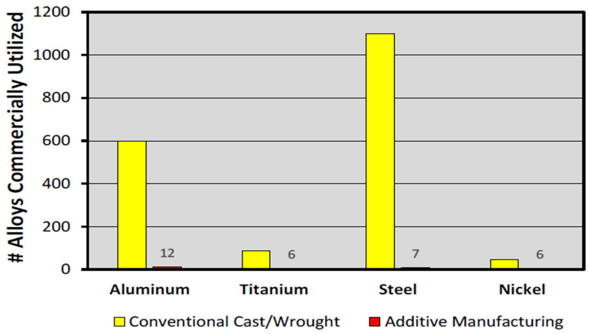

Figure 22: The comparison of materials used in conventional manufacturing to the materials used in AM [433]. (Image source: [433])

landscape for AM is dominated by materials that were successful with conventional manufacturing techniques. These materials were not designed for the complex thermal cycling inherent to AM, which result in material defects and anisotropic microstructures. Thus, the development of new materials created explicitly for AM could allow for more control over phase transformations, elemental segregation, and the resulting microstructure. This is especially crucial for large components, where heat treatment procedures incur a financial cost that make them unfeasible compared to conventional manufacturing. Furthermore, microstructural control will allow for predictions in how the part will perform when in service, which is imperative for on-site fabrication. Some promising alternative methodologies are being explored to prevent the epitaxial growth of large columnar grains. The addition of inoculants to aid in the nucleation of equiaxed grains would eliminate anisotropic mechanical properties prevalent in a lot of AM deposits [435]. The addition of boron to Ti64 has been shown to form TiB, which allows for the nucleation of α-grains, resulting in an isotropic grain structure [436]. A similar phenomenon has been reported with the addition of Ti to 5356 Al [253]. Furthermore, the addition of carbon to Ti64's hypoeutectic composition decreases the solidification temperature, causing grain growth restriction through constitutional supercooling. Although a different mechanism, a similar isotropic grain structure occurred[437]. These studies highlight that the development of materials better suited for AM is going to involve understanding the fundamental material paradigms involved in grain growth and solidification, and how these can be used to manipulate the thermodynamics of the system, to mitigate some of the microstructural challenges that researchers are currently faced with. Large amounts of data can be compiled by completing the aforementioned experiments on increasing the materials being trialed for AM, trying completely new material compositions, and in-situ grain control, which can then be used as input for artificial neural networks, to synthesize new materials specifically for AM. This would also incorporate all the data from the published process planning and monitoring and control strategies, allowing the network to develop the appropriate deposition strategy for the new material. The seed to the network would be a material of known composition, as-built microstructure, and mechanical properties. The network would have the ability to simulate the deposition of the material and then predict its as-built microstructure and mechanical properties. The model would employ reinforcement learning strategies to iterate over various compositions of the material, based on the data acquired from the research, to optimize the microstructure and mechanical properties based on the part's specifications. This could completely reinvent how material selection is done and produce materials specifically tailored to the additive manufacturing of that specific part.

The materials available for large-scale robotic AM are currently limited to current alloys in either the welding or coating processes. Material development for various processes used in AM is in its infancy and will yield significant opportunities as the processes mature.

7.5. Post Processing

The complex thermal cycling of AM leads to microstructures that are not found in conventional casting and forging operations. Using design guidelines of traditional heat treatment protocols can result in poorer mechanical properties in some materials. This is attributed to the varying degrees of segregation or the novel grain structure that occurs during deposition [438]. Furthermore, many post-processing operations rely on HIPing to reduce internal porosity. This is problematic for large-scale AM due to the inherent cost of this procedure and the size of the processing chamber needed to contain the large part. Thus, developing techniques to reduce porosity in situ will be an essential future contribution to AM. Furthermore, the poor geometric tolerance obtained from parts manufactured using particular metal DED systems will need to be improved to reduce the manufacturing costs. This problem currently necessitates hybrid manufacturing systems or some combination of additive and subtractive technologies. This requires developing frameworks that unify positioning, referencing, and planning software to negate the need to detach the part from the build plate and any post-processing. The framework would also need to include localized heat treatment and a means to control the whole part's thermal cycle to ensure the promised mechanical performance. Thus, it is speculated that the next generation of large-scale AM systems will appear more similar to traditional manufacturing approaches than powder bed fusion systems. There will be some modularity, where the part will be fabricated and machined in one module and then transferred automatically to a separate heat treatment module, similar to what is seen in traditional manufacturing. It is clear that an integrated automation system will increase productivity for this type of manufacturing. However, this manufacturing system would offer the geometrical freedom and the multi-meter scalability that both traditional and PBF are unable to provide.

The challenge remains to identify the raw materials, process conditions, and process control to maximize product quality using the AM processes and minimize subsequent post-processing requirements. The novel solutions will only be met through multidisciplinary and cross-functional teams closely collaborating. For example, this paper could not have been written without the close collaboration between mechanical, process control, mechatronics, electrical, and materials engineers.

The future young engineers trained in AM will require a holistic knowledge base and the ability to work cooperatively with other disciplines in engineering, sciences, design, and visual arts. This paper has intentionally not addressed the redesign of components from both an engineering or artistic design approach. However, the possibilities using AM technologies will reveal new opportunities that are currently not imaginable.

8. Acknowledgements

This work would not be possible without the financial aid from the Syncrude-NSERC CRD (CRDPJ 514752-17), Mitacs (MITACS MA IT11329) and HI-AM (NSERC HI-AM NETGP 494158), as well as the in-kind contribution and resources given by Innotech Alberta. The authors would like to thank Stefano Chiovelli for his support and adding an industrial perspective to the paper.

References

[1] T. D. Ngo, A. Kashani, G. Imbalzano, K. T. Nguyen, and D. Hui, "Additive manufacturing (3D printing): A review of materials, methods, applications and challenges," *Composites Part B: Engineering*, vol. 143, pp. 172–196, jun 2018.

[2] ASTM International, "Additive Manufacturing - ASTM International," p. 1, 2017. [Online]. Available: https://www.astm.org/industry/additive-manufacturing-overview.html

[3] B. P. Conner, G. P. Manogharan, A. N. Martof, L. M. Rodomsky, C. M. Rodomsky, D. C. Jordan, and J. W. Limperos, "Making sense of 3-D printing: Creating a map of additive manufacturing products and services," *Additive Manufacturing*, vol. 1, pp. 64–76, oct 2014.

[4] E. Herderick, "Additive manufacturing of metals: A review," *Materials Science and Technology Conference*, vol. 2, no. 176252, pp. 1413–1425, 2011.

[5] J. Bard, D. Cupkova, N. Washburn, and G. Zeglin, "Robotic concrete surface finishing: a moldless approach to creating thermally tuned surface geometry for architectural building components using Profile-3D-Printing," *Construction Robotics*, vol. 2, no. 1, pp. 53–65, 2018.

[6] "ISO 17296-2 - Additive manufacturing - General principles - Part 2: Overview of process categories and feedstock - First Edition," pp. 1–16, 2015.

[7] "Aurora Labs," 2014. [Online]. Available: http://auroralabs3d.com/

[8] "Additive Manufacturing Machines & Materials | GE Additive." [Online]. Available: https://www.ge.com/additive/

[9] "Xact Metal: Accessible, High-Caliber 3D Metal Printing is Here." [Online]. Available: https://www.xactmetal.com/

[10] J. Dumas, J. Hergel, and S. Lefebvre, "Bridging the gap: Automated steady scaffoldings for 3D printing," *ACM Transactions on Graphics*, vol. 33, no. 4, pp. 1–10, jul 2014.

[11] K. Hu, S. Jin, and C. C. Wang, "Support slimming for single material based additive manufacturing," *CAD Computer Aided Design*, vol. 65, pp. 1–10, aug 2015.

[12] D. Wang, Y. Yang, R. Liu, D. Xiao, and J. Sun, "Study on the designing rules and processability of porous structure based on selective laser melting (SLM)," *Journal of Materials Processing Technology*, vol. 213, no. 10, pp. 1734–1742, oct 2013.

[13] D. Thomas, H. Computer, and A. Product, *The Development of Design Rules for Selective Laser Melting The Development of Design Rules for Selective Laser Melting*. Universiy of Wales Institute Cardiff, 2010.

[14] F. Calignano, "Design optimization of supports for overhanging structures in aluminum and titanium alloys by selective laser melting," *Materials and Design*, vol. 64, pp. 203–213, dec 2014.

[15] R. plc, "Educational article - Design for metal AM - A beginner ' s guide," pp. 1–7, 2017. [Online]. Available: http://www.renishaw.com/en/design-for-metal-am-a-beginners-guide-feature--43333

[16] Y. Ding, R. Dwivedi, and R. Kovacevic, "Process planning for 8-axis robotized laser-based direct metal deposition system: A case on building revolved part," *Robotics and Computer-Integrated Manufacturing*, vol. 44, pp. 67–76, apr 2017.

[17] P. Singh and D. Dutta, "Multi-direction slicing for layered manufacturing," *Journal of Computing and Information Science in Engineering*, vol. 1, no. 2, pp. 129–142, jun 2001.

[18] R. Dwivedi and R. Kovacevic, "An expert system for generation of machine inputs for laser-based multi-directional metal deposition," *International Journal of Machine Tools and Manufacture*, vol. 46, no. 14, pp. 1811–1822, nov 2006.

[19] ——, "Automated torch path planning using polygon subdivision for solid freeform fabrication based on welding," *Journal of Manufacturing Systems*, vol. 23, no. 4, pp. 278–291, jan 2004.

[20] J. L. Prado-Cerqueira, J. L. Diéguez, and A. M. Camacho, "Preliminary development of a Wire and Arc Additive Manufacturing system (WAAM)," *Procedia Manufacturing*, vol. 13, pp. 895–902, jan 2017.

[21] T. Artaza, A. Alberdi, M. Murua, J. Gorrotxategi, J. Frías, G. Puertas, M. A. Melchor, D. Mugica, and A. Suárez, "Design and integration of WAAM technology and in situ monitoring system in a gantry machine," *Procedia Manufacturing*, vol. 13, pp. 778–785, jan 2017.

[22] J. S. Panchagnula and S. Simhambhatla, "Additive manufacturing of complex shapes through weld-deposition and feature based slicing," in *ASME International Mechanical Engineering Congress and Exposition, Proceedings (IMECE)*, vol. 2A-2015. ASME, nov 2015, p. V02AT02A004.

[23] ——, "Manufacture of complex thin-walled metallic objects using weld-deposition based additive manufacturing," *Robotics and Computer-Integrated Manufacturing*, vol. 49, pp. 194–203, feb 2018.

[24] P. Urhal, A. Weightman, C. Diver, and P. Bartolo, "Robot assisted additive manufacturing: A review," *Robotics and Computer-Integrated Manufacturing*, vol. 59, pp. 335–345, oct 2019.

[25] B. Lauwers, F. Klocke, A. Klink, A. E. Tekkaya, R. Neugebauer, and D. McIntosh, "Hybrid processes in manufacturing," *CIRP Annals - Manufacturing Technology*, vol. 63, no. 2, pp. 561–583, jan 2014.

[26] Z. Zhu, V. G. Dhokia, A. Nassehi, and S. T. Newman, "A review of hybrid manufacturing processes - State of the art and future perspectives," *International Journal of Computer Integrated Manufacturing*, vol. 26, no. 7, pp. 596–615, jul 2013.

[27] A. Nassehi, S. Newman, V. Dhokia, Z. Zhu, and R. I. Asrai, "Using formal methods to model hybrid manufacturing processes," in *Enabling Manufacturing Competitiveness and Economic Sustainability*. Berlin, Heidelberg: Springer Berlin Heidelberg, 2012, pp. 52–56.

[28] S. T. Newman, Z. Zhu, V. Dhokia, and A. Shokrani, "Process planning for additive and subtractive manufacturing technologies," *CIRP Annals - Manufacturing Technology*, vol. 64, no. 1, pp. 467–470, jan 2015.

[29] K. P. Karunakaran, S. Suryakumar, V. Pushpa, and S. Akula, "Low cost integration of additive and subtractive processes for hybrid layered manufacturing," *Robotics and Computer-Integrated Manufacturing*, vol. 26, no. 5, pp. 490–499, oct 2010.

[30] X. Xiong, H. Zhang, and G. Wang, "Metal direct prototyping by using hybrid plasma deposition and milling," *Journal of Materials Processing Technology*, vol. 209, no. 1, pp. 124–130, jan 2009.

[31] L. Ren, T. Sparks, J. Ruan, and F. Liou, "Integrated process planning for a multiaxis hybrid manufacturing system," *Journal of Manufacturing Science and Engineering, Transactions of the ASME*, vol. 132, no. 2, pp. 0 210 061–0 210 067, apr 2010.

[32] Z. Zhu, V. Dhokia, S. T. Newman, and A. Nassehi, "Application of a hybrid process for high precision manufacture of difficult to machine prismatic parts," *International Journal of Advanced Manufacturing Technology*, vol. 74, no. 5-8, pp. 1115–1132, sep 2014.

[33] O. Kerbrat, P. Mognol, and J. Y. Hascoët, "A new DFM approach to combine machining and additive manufacturing," *Computers in Industry*, vol. 62, no. 7, pp. 684–692, sep 2011.

[34] B. Salmi, "The World's Largest 3D Metal Printer Is Churning Out Rockets," 2019. [Online]. Available: https://spectrum.ieee.org/aerospace/space-flight/the-worlds-largest-3d-metal-printer-is-churning-out-rockets

[35] J. Peels, "MX3D Uses Robot Arm to Make 3D Printed Robot Arm, Installs It on Robot," 2020. [Online]. Available: https://3dprint.com/270122/mx3d-uses-robot-arm-to-3d-print-

robot-arm-installs-it-on-robot-d/

[36] Y. Ding and R. Kovacevic, "Feasibility Study on 3-D Printing of Metallic Structural Materials with Robotized Laser-Based Metal Additive Manufacturing," *Jom*, vol. 68, no. 7, pp. 1774–1779, jul 2016.

[37] Y. Ding, J. Warton, and R. Kovacevic, "Development of sensing and control system for robotized laser-based direct metal addition system," *Additive Manufacturing*, vol. 10, pp. 24–35, apr 2016.

[38] H. Zheng, M. Cong, D. Liu, Y. Liu, and Y. Du, "Automatic path and trajectory planning for laser cladding robot based on CAD," in *2016 IEEE International Conference on Mechatronics and Automation, IEEE ICMA 2016*. IEEE, aug 2016, pp. 1338–1343.

[39] G. Ma, G. Zhao, Z. Li, and W. Xiao, "A Path Planning Method for Robotic Wire and Arc Additive Manufacturing of Thin-Walled Structures with Varying Thickness," *IOP Conference Series: Materials Science and Engineering*, vol. 470, no. 1, 2019.

[40] M. Sheetz, "Relativity, a company 3D printing entire rockets, raises $140 million from venture firms Bond, Tribe," 2019. [Online]. Available: https://www.cnbc.com/2019/10/01/rocket-builder-relativity-raises-140-million-from-mary-meeker-others.html

[41] "MX3D," 2020. [Online]. Available: https://mx3d.com/

[42] "AML3D," 2020. [Online]. Available: https://aml3d.com/

[43] AMFG, "Thinking Big: 4 Impressive Applications of Large-Scale 3D Printing," 2019. [Online]. Available: https://amfg.ai/2019/04/02/thinking-big-4-impressive-applications-of-large-scale-3d-printing/

[44] A. H. Maamoun, M. Elbestawi, G. K. Dosbaeva, and S. C. Veldhuis, "Thermal post-processing of AlSi10Mg parts produced by Selective Laser Melting using recycled powder," *Additive Manufacturing*, vol. 21, pp. 234–247, may 2018.

[45] A. M. Paradowska, J. W. H. Price, R. Ibrahim, and T. R. Finlayson, "The effect of heat input on residual stress distribution of steel welds measured by neutron diffraction," *Journal of Achievements in Materials and Manufacturing Engineering*, vol. 17, no. 1, pp. 385–388, 2006.

[46] E. Mirkoohi, J. R. Dobbs, and S. Y. Liang, "Analytical modeling of residual stress in direct metal deposition considering scan strategy," *International Journal of Advanced Manufacturing Technology*, vol. 106, no. 9-10, pp. 4105–4121, feb 2020.

[47] D. Ding, Z. Pan, D. Cuiuri, and H. Li, "A tool-path generation strategy for wire and arc additive manufacturing," *International Journal of Advanced Manufacturing Technology*, vol. 73, no. 1-4, pp. 173–183, jul 2014.

[48] ——, "A practical path planning methodology for wire and arc additive manufacturing of thin-walled structures," *Robotics and Computer-Integrated Manufacturing*, vol. 34, pp. 8–19, aug 2015.

[49] D. Ding, Z. Pan, D. Cuiuri, H. Li, and N. Larkin, "Adaptive path planning for wire-feed additive manufacturing using medial axis transformation," *Journal of Cleaner Production*, vol. 133, pp. 942–952, oct 2016.

[50] S. Yin, P. Cavaliere, B. Aldwell, R. Jenkins, H. Liao, W. Li, and R. Lupoi, "Cold spray additive manufacturing and repair: Fundamentals and applications," *Additive Manufacturing*, vol. 21, pp. 628 – 650, 2018.

[51] Y. Cormier, P. Dupuis, A. Farjam, A. Corbeil, and B. Jodoin, "Additive manufacturing of pyramidal pin fins: Height and fin density effects under forced convection," *International Journal of Heat and Mass Transfer*, vol. 75, pp. 235 – 244, 2014.

[52] P. Dupuis, Y. Cormier, M. Fenech, and B. Jodoin, "Heat transfer and flow structure characterization for pin fins produced by cold spray additive manufacturing," *International Journal of Heat and Mass Transfer*, vol. 98, pp. 650 – 661, 2016.

[53] M. A. Wahab, "Manual Metal Arc Welding and Gas Metal Arc Welding," in *Comprehensive Materials Processing*. Elsevier Ltd, may 2014, vol. 6, pp. 49–76.

[54] S. W. Williams, F. Martina, A. C. Addison, J. Ding, G. Pardal, and P. Colegrove, "Wire + Arc additive manufacturing," *Materials Science and Technology (United Kingdom)*, vol. 32, no. 7, pp. 641–647, may 2016.

[55] D. Ding, Z. Pan, S. van Duin, H. Li, and C. Shen, "Fabricating superior NiAl bronze components through wire arc additive manufacturing," *Materials*, vol. 9, no. 8, aug 2016.

[56] F. Martina, J. Ding, S. Williams, A. Caballero, G. Pardal, and L. Quintino, "Tandem metal inert gas process for high productivity wire arc additive manufacturing in stainless steel," *Additive Manufacturing*, vol. 25, pp. 545–550, jan 2019.

[57] R. Singh, "Welding and Joining Processes," in *American Society of Mechanical Engineers, Production Engineering Division (Publication) PED*, 2nd ed., R. Singh, Ed. Butterworth-Heinemann, 1991, vol. 51, pp. 163–195.

[58] P. M. Sequeira Almeida and S. Williams, "Innovative process model of Ti-6Al-4V additive layer manufacturing using cold metal transfer (CMT)," in *21st Annual International Solid Freeform Fabrication Symposium - An Additive Manufacturing Conference, SFF 2010*, 2010, pp. 25–36.

[59] J. Feng, H. Zhang, and P. He, "The CMT short-circuiting metal transfer process and its use in thin aluminium sheets welding," *Materials and Design*, vol. 30, no. 5, pp. 1850–1852, may 2009.

[60] C. G. Pickin and K. Young, "Evaluation of cold metal transfer (CMT) process for welding aluminium alloy," *Science and Technology of Welding and Joining*, vol. 11, no. 5, pp. 583–585, sep 2006.

[61] J. Gu, J. Ding, S. W. Williams, H. Gu, J. Bai, Y. Zhai, and P. Ma, "The strengthening effect of inter-layer cold working and post-deposition heat treatment on the additively manufactured Al-6.3Cu alloy," *Materials Science and Engineering A*, vol. 651, pp. 18–26, jan 2016.

[62] T. Lehmann, A. Jain, Y. Jain, H. Stainer, T. Wolfe, H. Henein, and A. J. Qureshi, "Concurrent Geometry- and Material-based Process Identification and Optimization for Robotic CMT-based Wire Arc Additive Manufacturing," *Materials & Design*, vol. In press, 2020.

[63] C. Zhang, Y. Li, M. Gao, and X. Zeng, "Wire arc additive manufacturing of Al-6Mg alloy using variable polarity cold metal transfer arc as power source," *Materials Science and Engineering A*, vol. 711, no. August 2017, pp. 415–423, jan 2018.

[64] F. Wang, S. Williams, and M. Rush, "Morphology investigation on direct current pulsed gas tungsten arc welded additive layer manufactured Ti6Al4V alloy," *International Journal of Advanced Manufacturing Technology*, vol. 57, no. 5-8, pp. 597–603, nov 2011.

[65] K. Oyama, S. Diplas, M. M'hamdi, A. E. Gunnæs, and A. S. Azar, "Heat source management in wire-arc additive manufacturing process for Al-Mg and Al-Si alloys," *Additive Manufacturing*, vol. 26, pp. 180–192, mar 2019.

[66] D. Jafari, T. H. J. Vaneker, and I. Gibson, "Wire and arc additive manufacturing: Opportunities and challenges to control the quality and accuracy of manufactured parts," *Materials & Design*, vol. 202, p. 109471, 2021.

[67] P. M. Dickens, M. S. Pridham, R. C. Cobb, I. Gibson, and G. Dixon, "Rapid prototyping using 3-D welding," in *Solid Freeform Fabrication Proceedings*, 1992, pp. 280–290.

[68] R. Singh, "Chapter 3 - Welding and Joining Processes BT - Applied Welding Engineering," in *Applied Welding Engineering*, R. Singh, Ed. Boston: Butterworth-Heinemann, 2012, pp. 147–170.

[69] F. Xu, V. Dhokia, P. Colegrove, A. McAndrew, S. Williams, A. Henstridge, and S. T. Newman, "Realisation of a multi-sensor framework for process monitoring of the wire arc additive manufacturing in producing Ti-6Al-4V parts," *International Journal of Computer Integrated Manufacturing*, vol. 31, no. 8, pp. 785–798, 2018.

[70] Z. Pan, D. Ding, B. Wu, D. Cuiuri, H. Li, and J. Norrish, "Arc Welding Processes for Additive Manufacturing: A Review," in *Transactions on Intelligent Welding Manufacturing*. Springer, Singapore, 2018, pp. 3–24.

[71] Y. Ma, D. Cuiuri, N. Hoye, H. Li, and Z. Pan, "The effect of location on the microstructure and mechanical properties of titanium aluminides produced by additive layer manufacturing using in-situ alloying and gas tungsten arc welding," *Materials Science and Engineering A*, vol. 631, pp. 230–240, apr 2015.

[72] C. Shen, Z. Pan, D. Cuiuri, J. Roberts, and H. Li, "Fabrication of Fe-FeAl Functionally Graded Material Using the Wire-Arc Additive Manufacturing Process," *Metallurgical and Materials Transactions B: Process Metallurgy and Materials Processing Science*, vol. 47, no. 1, pp. 763–772, feb 2016.

[73] C. Shen, Z. Pan, Y. Ma, D. Cuiuri, and H. Li, "Fabrication of iron-rich Fe-Al intermetallics using the wire-arc additive manufacturing process," *Additive Manufacturing*, vol. 7, pp. 20–26, jul 2015.

[74] F. Wang, S. Williams, P. Colegrove, and A. A. Antonysamy, "Microstructure and mechanical properties of wire and arc additive manufactured Ti-6Al-4V," *Metallurgical and Materials Transactions A: Physical

Metallurgy and Materials Science, vol. 44, no. 2, pp. 968–977, feb 2013.

[75] B. Baufeld, O. V. der Biest, and R. Gault, “Additive manufacturing of Ti-6Al-4V components by shaped metal deposition: Microstructure and mechanical properties,” *Materials and Design*, vol. 31, no. SUPPL. 1, pp. S106–S111, jun 2010.

[76] B. Baufeld, E. Brandl, and O. Van Der Biest, “Wire based additive layer manufacturing: Comparison of microstructure and mechanical properties of Ti-6Al-4V components fabricated by laser-beam deposition and shaped metal deposition,” *Journal of Materials Processing Technology*, vol. 211, no. 6, pp. 1146–1158, 2011.

[77] E. Brandl, B. Baufeld, C. Leyens, and R. Gault, “Additive manufactured Ti-6A1-4V using welding wire: Comparison of laser and arc beam deposition and evaluation with respect to aerospace material specifications,” in *Physics Procedia*, vol. 5, no. PART 2. Elsevier B.V., jan 2010, pp. 595–606.

[78] A. K. Lakshminarayanan, V. Balasubramanian, and K. Elangovan, “Effect of welding processes on tensile properties of AA6061 aluminium alloy joints,” *International Journal of Advanced Manufacturing Technology*, vol. 40, no. 3-4, pp. 286–296, jan 2009.

[79] J. F. Wang, Q. J. Sun, H. Wang, J. P. Liu, and J. C. Feng, “Effect of location on microstructure and mechanical properties of additive layer manufactured Inconel 625 using gas tungsten arc welding,” *Materials Science and Engineering A*, vol. 676, pp. 395–405, oct 2016.

[80] D. Ding, Z. Pan, D. Cuiuri, and H. Li, “Wire-feed additive manufacturing of metal components: technologies, developments and future interests,” *International Journal of Advanced Manufacturing Technology*, vol. 81, no. 1-4, pp. 465–481, oct 2015.

[81] Z. Feng, *Processes and Mechanisms of Welding Residual Stress and Distortion*. Elsevier Ltd., oct 2005.

[82] F. Martina, J. Mehnen, S. W. Williams, P. Colegrove, and F. Wang, “Investigation of the benefits of plasma deposition for the additive layer manufacture of Ti-6Al-4V,” *Journal of Materials Processing Technology*, vol. 212, no. 6, pp. 1377–1386, jun 2012.

[83] T. Wolfe, “Homogeneity of Metal Matrix Composites Deposited by Plamsa Transferred Arc Welding,” Ph.D. dissertation, University of Alberta, Edmonton, 2010.

[84] M. Yarmuch, *Effect of Welding Parameters on the Plasma Transferred Arc Welding (PTAW) Process for Autogenous Beads and 410SS-WC Overlays*. University of Alberta, 2006.

[85] E. A. Alberti, B. M. Bueno, and A. S. D’Oliveira, “Additive manufacturing using plasma transferred arc,” *International Journal of Advanced Manufacturing Technology*, vol. 83, no. 9-12, pp. 1861–1871, apr 2016.

[86] E. A. Alberti, B. M. P. Bueno, and A. S. C. D’Oliveira, “Processamento de ligas de níquel com técnica de manufatura aditiva utilizando plasma por arco transferido,” *Soldagem e Inspecao*, vol. 20, no. 2, pp. 137–147, 2015.

[87] E. P. Cardozo, S. Ríos, S. Ganguly, and A. S. C. D’Oliveira, “Assessment of the effect of different forms of Inconel 625 alloy feedstock in Plasma Transferred Arc (PTA) additive manufacturing,” *International Journal of Advanced Manufacturing Technology*, vol. 98, no. 5-8, pp. 1695–1705, sep 2018.

[88] E. M. Perez-Soriano, E. Ariza, C. Arevalo, I. Montealegre-Melendez, M. Kitzmantel, and E. Neubauer, “Processing by additive manufacturing based on plasma transferred arc of hastelloy in air and argon atmosphere,” *Metals*, vol. 10, no. 2, p. 200, jan 2020.

[89] J. G. Mercado Rojas, T. Wolfe, B. A. Fleck, and A. J. Qureshi, “Plasma transferred arc additive manufacturing of Nickel metal matrix composites,” *Manufacturing Letters*, vol. 18, pp. 31–34, oct 2018.

[90] K. Hoefer and P. Mayr, “Additive manufacturing of titanium parts using 3d plasma metal deposition,” *Materials Science Forum*, vol. 941 MSF, pp. 2137–2141, 2018.

[91] K. Hoefer, J. Rodriguez, A. Haelsig, K. G. Abstoss, and P. Mayr, “Fabrication of SS316L to Ni80Cr20 graded structures by 3D plasma metal deposition,” *Welding in the World*, pp. 1–5, mar 2020.

[92] J. Rodriguez, K. Hoefer, A. Haelsig, and P. Mayr, “Functionally graded SS 316l to ni-based structures produced by 3D plasma metal deposition,” *Metals*, vol. 9, no. 6, p. 620, may 2019.

[93] K. Hoefer, A. Nitsche, K. G. Abstoss, G. Ertugrul, A. Haelsig, and P. Mayr, “Multi-material Additive Manufacturing by 3D Plasma Metal Deposition for Graded Structures of Super Duplex Alloy 1.4410 and the Austenitic Corrosion Resistant Alloy 1.4404,” *Jom*, vol. 71, no. 4, pp. 1554–1559, apr 2019.

[94] K. Hoefer, A. Haelsig, and P. Mayr, “Arc-based additive manufacturing of steel components–comparison of wire- and powder-based variants,” *Welding in the World*, vol. 62, no. 2, pp. 243–247, mar 2018.

[95] R. P. Mudge and N. R. Wald, “Laser engineered net shaping advances additive manufacturing and repair,” *Welding Journal (Miami, Fla)*, vol. 86, no. 1, pp. 44–48, 2007.

[96] A. Saboori, A. Aversa, G. Marchese, S. Biamino, M. Lombardi, and P. Fino, “Application of directed energy deposition-based additive manufacturing in repair,” *Applied Sciences (Switzerland)*, vol. 9, no. 16, p. 3316, aug 2019.

[97] R. Liu, Z. Wang, T. Sparks, F. Liou, and J. Newkirk, “13 - aerospace applications of laser additive manufacturing,” in *Laser Additive Manufacturing*, ser. Woodhead Publishing Series in Electronic and Optical Materials, M. Brandt, Ed. Woodhead Publishing, 2017, pp. 351 – 371.

[98] Y. F. Lu and Y. Aoyagi, “Temperature rise and heat flux induced by laser beam with double-gaussian intensity distribution,” *Japanese Journal of Applied Physics*, vol. 34, no. 7R, pp. 3759–3763, 1995.

[99] W. Piekarska and M. Kubiak, “Theoretical investigations into heat transfer in laser-welded steel sheets,” in *Journal of Thermal Analysis and Calorimetry*, vol. 110, no. 1. Springer, oct 2012, pp. 159–166.

[100] A. Marmołowski and W. Kiełczyński, “Modelling of the heat flux density distribution for laser beam welding,” in *Solid State Phenomena*, ser. Solid State Phenomena, vol. 183. Trans Tech Publications Ltd, 2012, pp. 241–248.

[101] A. M. Fudolig, H. Nogami, and J. I. Yagi, “Numerical analysis of the flow characteristics and temperature distribution in metal beads subjected to transferred arc plasma impingement,” *ISIJ International*, vol. 37, no. 6, pp. 630–636, jun 1997.

[102] J. D. Majumdar, A. Pinkerton, Z. Liu, I. Manna, and L. Li, “Microstructure characterisation and process optimization of laser assisted rapid fabrication of 316L stainless steel,” *Applied Surface Science*, vol. 247, no. 1-4, pp. 320–327, jul 2005.

[103] A. A. Adeyemi, E. Akinlabi, R. M. Mahamood, K. O. Sanusi, S. Pityana, and M. Tlotleng, “Influence of laser power on microstructure of laser metal deposited 17-4 ph stainless steel,” *IOP Conference Series: Materials Science and Engineering*, vol. 225, p. 012028, aug 2017.

[104] S. L. Campanelli, A. Angelastro, C. G. Signorile, and G. Casalino, “Investigation on direct laser powder deposition of 18 Ni (300) marage steel using mathematical model and experimental characterisation,” *International Journal of Advanced Manufacturing Technology*, vol. 89, no. 1-4, pp. 885–895, mar 2017.

[105] N. Yang, J. Yee, B. Zheng, K. Gaiser, T. Reynolds, L. Clemon, W. Y. Lu, J. M. Schoenung, and E. J. Lavernia, “Process-Structure-Property Relationships for 316L Stainless Steel Fabricated by Additive Manufacturing and Its Implication for Component Engineering,” *Journal of Thermal Spray Technology*, vol. 26, no. 4, pp. 610–626, apr 2017.

[106] K. Zhang, S. Wang, W. Liu, and X. Shang, “Characterization of stainless steel parts by Laser Metal Deposition Shaping,” *Materials and Design*, vol. 55, pp. 104–119, mar 2014.

[107] M. L. Griffith, M. T. Ensz, J. D. Puskar, C. V. Robino, J. A. Brooks, J. A. Philliber, J. E. Smugeresky, and W. H. Hofmeister, “Understanding the microstructure and properties of components fabricated by Laser Engineered Net Shaping (LENS),” *Materials Research Society Symposium - Proceedings*, vol. 625, no. 1, pp. 9–20, nov 2000.

[108] J. Yu, M. Rombouts, and G. Maes, “Cracking behavior and mechanical properties of austenitic stainless steel parts produced by laser metal deposition,” *Materials and Design*, vol. 45, pp. 228–235, mar 2013.

[109] J. Yao, T. Suo, S. Zhang, F. Zhao, H. Wang, J. Liu, Y. Chen, and Y. Li, “Influence of heat-treatment on the dynamic behavior of 3D laser-deposited Ti-6Al-4V alloy,” *Materials Science and Engineering A*, vol. 677, pp. 153–162, nov 2016.

[110] A. J. Sterling, B. Torries, N. Shamsaei, S. M. Thompson, and D. W. Seely, “Fatigue behavior and failure mechanisms of direct laser deposited Ti-6Al-4V,” *Materials Science and Engineering A*, vol. 655, pp. 100–112, 2016.

[111] Y. Lu, H. B. Tang, Y. L. Fang, D. Liu, and H. M. Wang, “Microstructure evolution of sub-critical annealed laser deposited Ti-6Al-4V alloy,” *Materials and Design*, vol. 37, pp. 56–63, 2012.

[112] S. Zhang, X. Lin, J. Chen, and W. Huang, “Heat-treated microstructure and mechanical properties of laser solid forming Ti-6Al-4V alloy,” *Rare*

Metals, vol. 28, no. 6, pp. 537–544, dec 2009.

[113] P. H. Li, W. G. Guo, W. D. Huang, Y. Su, X. Lin, and K. B. Yuan, "Thermomechanical response of 3D laser-deposited Ti-6Al-4V alloy over a wide range of strain rates and temperatures," *Materials Science and Engineering A*, vol. 647, pp. 34–42, oct 2015.

[114] B. E. Carroll, T. A. Palmer, and A. M. Beese, "Anisotropic tensile behavior of Ti-6Al-4V components fabricated with directed energy deposition additive manufacturing," *Acta Materialia*, vol. 87, pp. 309–320, apr 2015.

[115] C. Qiu, G. A. Ravi, C. Dance, A. Ranson, S. Dilworth, and M. M. Attallah, "Fabrication of large Ti-6Al-4V structures by direct laser deposition," *Journal of Alloys and Compounds*, vol. 629, pp. 351–361, apr 2015.

[116] A. Bagheri, N. Shamsaei, and S. M. Thompson, "Microstructure and mechanical properties of ti-6al-4v parts fabricated by laser engineered net shaping," in *ASME International Mechanical Engineering Congress and Exposition, Proceedings (IMECE)*, vol. 2A-2015. American Society of Mechanical Engineers, nov 2015.

[117] Y. Zhai, H. Galarraga, and D. A. Lados, "Microstructure, static properties, and fatigue crack growth mechanisms in Ti-6Al-4V fabricated by additive manufacturing: LENS and EBM," *Engineering Failure Analysis*, vol. 69, pp. 3–14, nov 2016.

[118] Y. Zhai, D. A. Lados, E. J. Brown, and G. N. Vigilante, "Understanding the microstructure and mechanical properties of Ti-6Al-4V and Inconel 718 alloys manufactured by Laser Engineered Net Shaping," *Additive Manufacturing*, vol. 27, pp. 334–344, 2019.

[119] T. Wang, Y. Y. Zhu, S. Q. Zhang, H. B. Tang, and H. M. Wang, "Grain morphology evolution behavior of titanium alloy components during laser melting deposition additive manufacturing," *Journal of Alloys and Compounds*, vol. 632, pp. 505–513, may 2015.

[120] F. Lv, L. Shen, H. Liang, D. Xie, C. Wang, and Z. Tian, "Mechanical properties of AlSi10Mg alloy fabricated by laser melting deposition and improvements via heat treatment," *Optik*, vol. 179, pp. 8–18, feb 2019.

[121] P. Kiani, A. D. Dupuy, K. Ma, and J. M. Schoenung, "Directed energy deposition of AlSi10Mg: Single track nonscalability and bulk properties," *Materials & Design*, vol. 194, p. 108847, 2020.

[122] F. Caiazzo, V. Alfieri, P. Argenio, and V. Sergi, "Additive manufacturing by means of laser-aided directed metal deposition of 2024 aluminium powder: Investigation and optimization," *Advances in Mechanical Engineering*, vol. 9, no. 8, pp. 1–12, aug 2017.

[123] B. Chen, Y. Yao, X. Song, C. Tan, L. Cao, and J. Feng, "Microstructure and mechanical properties of additive manufacturing AlSi10Mg alloy using direct metal deposition," *Ferroelectrics*, vol. 523, no. 1, pp. 153–166, jan 2018.

[124] Y. Liu, C. Liu, W. Liu, Y. Ma, S. Tang, C. Liang, Q. Cai, and C. Zhang, "Optimization of parameters in laser powder deposition AlSi10Mg alloy using Taguchi method," *Optics and Laser Technology*, vol. 111, no. October 2018, pp. 470–480, 2019.

[125] X. Wang, L. Li, J. Qu, and W. Tao, "Microstructure and mechanical properties of laser metal deposited AlSi10Mg alloys," *Materials Science and Technology (United Kingdom)*, vol. 35, no. 18, pp. 2284–2293, dec 2019.

[126] T. Gu, B. Chen, C. Tan, and J. Feng, "Microstructure evolution and mechanical properties of laser additive manufacturing of high strength Al-Cu-Mg alloy," *Optics and Laser Technology*, vol. 112, pp. 140–150, apr 2019.

[127] P. Ganesh, R. Kaul, C. P. Paul, P. Tiwari, S. K. Rai, R. C. Prasad, and L. M. Kukreja, "Fatigue and fracture toughness characteristics of laser rapid manufactured Inconel 625 structures," *Materials Science and Engineering A*, vol. 527, no. 29-30, pp. 7490–7497, nov 2010.

[128] C. Zhong, J. Kittel, A. Gasser, and J. H. Schleifenbaum, "Study of nickel-based super-alloys Inconel 718 and Inconel 625 in high-deposition-rate laser metal deposition," *Optics and Laser Technology*, vol. 109, pp. 352–360, jan 2019.

[129] Y. L. Hu, Y. L. Li, S. Y. Zhang, X. Lin, Z. H. Wang, and W. D. Huang, "Effect of solution temperature on static recrystallization and ductility of Inconel 625 superalloy fabricated by directed energy deposition," *Materials Science and Engineering: A*, vol. 772, p. 138711, 2020.

[130] H. Qi, M. Azer, and A. Ritter, "Studies of standard heat treatment effects on microstructure and mechanical properties of laser net shape manufactured INCONEL 718," *Metallurgical and Materials Transactions A: Physical Metallurgy and Materials Science*, vol. 40, no. 10, pp. 2410–2422, 2009.

[131] Z. Li, J. Chen, S. Sui, C. Zhong, X. Lu, and X. Lin, "The microstructure evolution and tensile properties of Inconel 718 fabricated by high-deposition-rate laser directed energy deposition," *Additive Manufacturing*, vol. 31, p. 100941, 2020.

[132] M. Ma, Z. Wang, and X. Zeng, "Effect of energy input on microstructural evolution of direct laser fabricated IN718 alloy," *Materials Characterization*, vol. 106, pp. 420–427, jul 2015.

[133] X. Zhao, J. Chen, X. Lin, and W. Huang, "Study on microstructure and mechanical properties of laser rapid forming Inconel 718," *Materials Science and Engineering A*, vol. 478, no. 1-2, pp. 119–124, apr 2008.

[134] C. Zhong, A. Gasser, J. Kittel, K. Wissenbach, and R. Poprawe, "Improvement of material performance of Inconel 718 formed by high deposition-rate laser metal deposition," *Materials and Design*, vol. 98, pp. 128–134, may 2016.

[135] Y. Wang and J. Shi, "Recrystallization behavior and tensile properties of laser metal deposited Inconel 718 upon in-situ ultrasonic impact peening and heat treatment," *Materials Science and Engineering: A*, vol. 786, p. 139434, 2020.

[136] P. D. Nezhadfar, A. S. Johnson, and N. Shamsaei, "Fatigue behavior and microstructural evolution of additively manufactured Inconel 718 under cyclic loading at elevated temperature," *International Journal of Fatigue*, vol. 136, p. 105598, 2020.

[137] K. D. Traxel and A. Bandyopadhyay, "First Demonstration of Additive Manufacturing of Cutting Tools using Directed Energy Deposition System: StelliteâĎć-Based Cutting Tools," *Additive Manufacturing*, vol. 25, pp. 460–468, jan 2019.

[138] K. M. Mantrala, M. Das, V. K. Balla, C. S. Rao, and V. V. S. Kesava Rao, "Additive Manufacturing of Co-Cr-Mo Alloy: Influence of Heat Treatment on Microstructure, Tribological, and Electrochemical Properties," *Frontiers in Mechanical Engineering*, vol. 1, mar 2015.

[139] Z. Smoqi, J. Toddy, H. S. Halliday, J. E. Shield, and P. Rao, "Process-structure relationship in the directed energy deposition of cobalt-chromium alloy (Stellite 21) coatings," *Materials and Design*, vol. 197, p. 109229, 2021.

[140] G. D. Janaki Ram, C. K. Esplin, and B. E. Stucker, "Microstructure and wear properties of LENS® deposited medical grade CoCrMo," *Journal of Materials Science: Materials in Medicine*, vol. 19, no. 5, pp. 2105–2111, may 2008.

[141] G. Y. Wang, S. N. Gu, and S. Yang, "Microstructure and properties of tungsten heavy alloys fabricated by laser direct deposition," *Materials Science and Technology (United Kingdom)*, vol. 33, no. 4, pp. 415–420, mar 2017.

[142] M. Zhong, W. Liu, G. Ning, L. Yang, and Y. Chen, "Laser direct manufacturing of tungsten nickel collimation component," *Journal of Materials Processing Technology*, vol. 147, no. 2, pp. 167–173, apr 2004.

[143] S. Moghazi, T. Wolfe, D. Ivey, and H. Henein, "Plasma Transfer Arc Additive Manufacturing of 17-4 PH: Assessment of Defects," *The International Journal of Advanced Manufacturing Technology*, vol. In press, 2020.

[144] N. Chekir, Y. Tian, J. J. Sixsmith, and M. Brochu, "Effect of travel speed and sub-β transus post deposition heat treatments on thin Ti-6Al-4V laser wire deposits," *Materials Science and Engineering A*, vol. 724, pp. 376–384, may 2018.

[145] E. Brandl, F. Palm, V. Michailov, B. Viehweger, and C. Leyens, "Mechanical properties of additive manufactured titanium (Ti-6Al-4V) blocks deposited by a solid-state laser and wire," *Materials and Design*, vol. 32, no. 10, pp. 4665–4675, 2011.

[146] N. Chekir, Y. Tian, R. Gauvin, N. Brodusch, J. J. Sixsmith, and M. Brochu, "Laser Wire Deposition of Thick Ti-6Al-4V Buildups: Heat Transfer Model, Microstructure, and Mechanical Properties Evaluations," *Metallurgical and Materials Transactions A: Physical Metallurgy and Materials Science*, vol. 49, no. 12, pp. 6490–6508, dec 2018.

[147] Y. N. Zhang, X. Cao, P. Wanjara, and M. Medraj, "Oxide films in laser additive manufactured Inconel 718," *Acta Materialia*, vol. 61, no. 17, pp. 6562–6576, oct 2013.

[148] C. V. Haden, G. Zeng, F. M. Carter, C. Ruhl, B. A. Krick, and D. G. Harlow, "Wire and arc additive manufactured steel: Tensile and wear properties," *Additive Manufacturing*, vol. 16, pp. 115–123, aug 2017.

[149] V. Laghi, M. Palermo, L. Tonelli, G. Gasparini, L. Ceschini, and

T. Trombetti, "Tensile properties and microstructural features of 304L austenitic stainless steel produced by wire-and-arc additive manufacturing," *International Journal of Advanced Manufacturing Technology*, vol. 106, no. 9-10, pp. 3693–3705, feb 2020.

[150] M. Rafieazad, M. Ghaffari, A. Vahedi Nemani, and A. Nasiri, "Microstructural evolution and mechanical properties of a low-carbon low-alloy steel produced by wire arc additive manufacturing," *International Journal of Advanced Manufacturing Technology*, vol. 105, no. 5-6, pp. 2121–2134, dec 2019.

[151] M. Liberini, A. Astarita, G. Campatelli, A. Scippa, F. Montevecchi, G. Venturini, M. Durante, L. Boccarusso, F. M. C. Minutolo, and A. Squillace, "Selection of Optimal Process Parameters for Wire Arc Additive Manufacturing," in *Procedia CIRP*, vol. 62. Elsevier B.V., jan 2017, pp. 470–474.

[152] V. T. Le and D. S. Mai, "Microstructural and mechanical characteristics of 308L stainless steel manufactured by gas metal arc welding-based additive manufacturing," *Materials Letters*, vol. 271, p. 127791, jul 2020.

[153] J. W. Elmer and G. Gibbs, "The effect of atmosphere on the composition of wire arc additive manufactured metal components," *Science and Technology of Welding and Joining*, vol. 24, no. 5, pp. 367–374, jul 2019.

[154] J. Lunde, M. Kazemipour, S. Salahi, and A. Nasiri, "Microstructure and Mechanical Properties of AISI 420 Stainless Steel Produced by Wire Arc Additive Manufacturing," in *Minerals, Metals and Materials Series*. Springer, 2020, pp. 413–424.

[155] L. Wang, J. Xue, and Q. Wang, "Correlation between arc mode, microstructure, and mechanical properties during wire arc additive manufacturing of 316L stainless steel," *Materials Science and Engineering A*, vol. 751, pp. 183–190, mar 2019.

[156] A. Caballero, J. Ding, S. Ganguly, and S. Williams, "Wire + Arc Additive Manufacture of 17-4 PH stainless steel: Effect of different processing conditions on microstructure, hardness, and tensile strength," *Journal of Materials Processing Technology*, vol. 268, pp. 54–62, jun 2019.

[157] W. Wu, J. Xue, L. Wang, Z. Zhang, Y. Hu, and C. Dong, "Forming Process, Microstructure, and Mechanical Properties of Thin-Walled 316L Stainless Steel Using Speed-Cold-Welding Additive Manufacturing," *Metals*, vol. 9, no. 1, p. 109, jan 2019.

[158] T. Wang, Y. Zhang, Z. Wu, and C. Shi, "Microstructure and properties of die steel fabricated by WAAM using H13 wire," *Vacuum*, vol. 149, pp. 185–189, mar 2018.

[159] X. Chen, J. Li, X. Cheng, B. He, H. Wang, and Z. Huang, "Microstructure and mechanical properties of the austenitic stainless steel 316L fabricated by gas metal arc additive manufacturing," *Materials Science and Engineering A*, vol. 703, pp. 567–577, aug 2017.

[160] B. Wu, Z. Pan, D. Ding, D. Cuiuri, H. Li, and Z. Fei, "The effects of forced interpass cooling on the material properties of wire arc additively manufactured Ti6Al4V alloy," *Journal of Materials Processing Technology*, vol. 258, pp. 97–105, aug 2018.

[161] J. R. Hönnige, P. A. Colegrove, B. Ahmad, M. E. Fitzpatrick, S. Ganguly, T. L. Lee, and S. W. Williams, "Residual stress and texture control in Ti-6Al-4V wire + arc additively manufactured intersections by stress relief and rolling," *Materials and Design*, vol. 150, pp. 193–205, jul 2018.

[162] J. Gou, J. Shen, S. Hu, Y. Tian, and Y. Liang, "Microstructure and mechanical properties of as-built and heat-treated Ti-6Al-4V alloy prepared by cold metal transfer additive manufacturing," *Journal of Manufacturing Processes*, vol. 42, pp. 41–50, jun 2019.

[163] Y. Tian, J. Shen, S. Hu, Z. Wang, and J. Gou, "Microstructure and mechanical properties of wire and arc additive manufactured Ti-6Al-4V and AlSi5 dissimilar alloys using cold metal transfer welding," *Journal of Manufacturing Processes*, vol. 46, pp. 337–344, oct 2019.

[164] A. Horgar, H. Fostervoll, B. Nyhus, X. Ren, M. Eriksson, and O. M. Akselsen, "Additive manufacturing using WAAM with AA5183 wire," *Journal of Materials Processing Technology*, vol. 259, pp. 68–74, sep 2018.

[165] B. Cong, J. Ding, and S. Williams, "Effect of arc mode in cold metal transfer process on porosity of additively manufactured Al-6.3%Cu alloy," *International Journal of Advanced Manufacturing Technology*, vol. 76, no. 9-12, pp. 1593–1606, feb 2015.

[166] X. Xu, J. Ding, S. Ganguly, and S. Williams, "Investigation of process factors affecting mechanical properties of INCONEL 718 superalloy in wire + arc additive manufacture process," *Journal of Materials Processing Technology*, vol. 265, pp. 201–209, mar 2019.

[167] D. Clark, M. R. Bache, and M. T. Whittaker, "Shaped metal deposition of a nickel alloy for aero engine applications," *Journal of Materials Processing Technology*, vol. 203, no. 1-3, pp. 439–448, jul 2008.

[168] C. E. Seow, H. E. Coules, G. Wu, R. H. Khan, X. Xu, and S. Williams, "Wire + Arc Additively Manufactured Inconel 718: Effect of post-deposition heat treatments on microstructure and tensile properties," *Materials and Design*, vol. 183, p. 108157, dec 2019.

[169] I. Jurić, I. Garašić, M. Bušić, and Z. Kožuh, "Influence of Shielding Gas Composition on Structure and Mechanical Properties of Wire and Arc Additive Manufactured Inconel 625," *Jom*, vol. 71, no. 2, pp. 703–708, feb 2019.

[170] W. Yangfan, C. Xizhang, and S. Chuanchu, "Microstructure and mechanical properties of Inconel 625 fabricated by wire-arc additive manufacturing," *Surface and Coatings Technology*, vol. 374, pp. 116–123, sep 2019.

[171] H. Takagi, H. Sasahara, T. Abe, H. Sannomiya, S. Nishiyama, S. Ohta, and K. Nakamura, "Material-property evaluation of magnesium alloys fabricated using wire-and-arc-based additive manufacturing," *Additive Manufacturing*, vol. 24, pp. 498–507, dec 2018.

[172] T. Klein, A. Arnoldt, M. Schnall, and S. Gneiger, "Microstructure Formation and Mechanical Properties of a Wire-Arc Additive Manufactured Magnesium Alloy," *JOM*, vol. 73, no. 4, pp. 1126–1134, 2021.

[173] J. Bi, J. Shen, S. Hu, Y. Zhen, F. Yin, and X. Bu, "Microstructure and mechanical properties of AZ91 Mg alloy fabricated by cold metal transfer additive manufacturing," *Materials Letters*, vol. 276, pp. 10–13, 2020.

[174] C. Shen, Z. Pan, D. Ding, L. Yuan, N. Nie, Y. Wang, D. Luo, D. Cuiuri, S. van Duin, and H. Li, "The influence of post-production heat treatment on the multi-directional properties of nickel-aluminum bronze alloy fabricated using wire-arc additive manufacturing process," *Additive Manufacturing*, vol. 23, pp. 411–421, oct 2018.

[175] G. P. Rajeev, M. R. Rahul, M. Kamaraj, and S. R. Bakshi, "Microstructure and high temperature mechanical properties of wire arc additively deposited Stellite 6 alloy," *Materialia*, vol. 12, no. January, p. 100724, 2020.

[176] L. Ji, J. Lu, C. Liu, C. Jing, H. Fan, and S. Ma, "Microstructure and mechanical properties of 304L steel fabricated by arc additive manufacturing," *MATEC Web of Conferences*, vol. 128, p. 03006, oct 2017.

[177] O. Yilmaz and A. A. Ugla, "Microstructure characterization of SS308LSi components manufactured by GTAW-based additive manufacturing: shaped metal deposition using pulsed current arc," *International Journal of Advanced Manufacturing Technology*, vol. 89, no. 1-4, pp. 13–25, mar 2017.

[178] B. Silwal and M. Santangelo, "Effect of vibration and hot-wire gas tungsten arc (GTA) on the geometric shape," *Journal of Materials Processing Technology*, vol. 251, pp. 138–145, jan 2018.

[179] J. Wang, X. Lin, J. Li, A. Xue, F. Liu, W. Huang, and E. Liang, "A study on obtaining equiaxed prior-β grains of wire and arc additive manufactured Ti-6Al-4V," *Materials Science and Engineering A*, vol. 772, p. 138703, jan 2020.

[180] J. Donoghue, A. A. Antonysamy, F. Martina, P. A. Colegrove, S. W. Williams, and P. B. Prangnell, "The effectiveness of combining rolling deformation with Wire-Arc Additive Manufacture on β-grain refinement and texture modification in Ti-6Al-4V," *Materials Characterization*, vol. 114, pp. 103–114, apr 2016.

[181] F. Martina, P. A. Colegrove, S. W. Williams, and J. Meyer, "Microstructure of Interpass Rolled Wire + Arc Additive Manufacturing Ti-6Al-4V Components," *Metallurgical and Materials Transactions A: Physical Metallurgy and Materials Science*, vol. 46, no. 12, pp. 6103–6118, oct 2015.

[182] J. Y. Bai, C. L. Fan, S. Lin, C. L. Yang, and B. L. Dong, "Effects of thermal cycles on microstructure evolution of 2219-Al during GTA-additive manufacturing," *International Journal of Advanced Manufacturing Technology*, vol. 87, no. 9-12, pp. 2615–2623, dec 2016.

[183] J. H. Ouyang, H. Wang, and R. Kovacevic, "Rapid prototyping of 5356-aluminum alloy based on variable polarity gas tungsten arc welding: process control and microstructure," *Materials and Manufacturing Processes*, vol. 17, no. 1, pp. 103–124, apr 2002.

[184] B. Baufeld, "Mechanical properties of INCONEL 718 parts manufac-

tured by shaped metal deposition (SMD)," *Journal of Materials Engineering and Performance*, vol. 21, no. 7, pp. 1416–1421, jul 2012.

[185] D. Clark, M. R. Bache, and M. T. Whittaker, "Microstructural characterization of a polycrystalline nickel-based superalloy processed via tungsten-intert-gas-shaped metal deposition," *Metallurgical and Materials Transactions B: Process Metallurgy and Materials Processing Science*, vol. 41, no. 6, pp. 1346–1353, jul 2010.

[186] J. Guo, Y. Zhou, C. Liu, Q. Wu, X. Chen, and J. Lu, "Wire arc additive manufacturing of AZ31 magnesium alloy: Grain refinement by adjusting pulse frequency," *Materials*, vol. 9, no. 10, oct 2016.

[187] Y. Guo, H. Pan, L. Ren, and G. Quan, "Microstructure and mechanical properties of wire arc additively manufactured AZ80M magnesium alloy," *Materials Letters*, vol. 247, pp. 4–6, jul 2019.

[188] Y. Guo, G. Quan, Y. Jiang, L. Ren, L. Fan, and H. Pan, "Formability, microstructure evolution and mechanical properties of wire arc additively manufactured AZ80M magnesium alloy using gas tungsten arc welding," *Journal of Magnesium and Alloys*, vol. 9, no. 1, pp. 192–201, 2021.

[189] B. Dong, Z. Pan, C. Shen, Y. Ma, and H. Li, "Fabrication of Copper-Rich Cu-Al Alloy Using the Wire-Arc Additive Manufacturing Process," *Metallurgical and Materials Transactions B: Process Metallurgy and Materials Processing Science*, vol. 48, no. 6, pp. 3143–3151, dec 2017.

[190] Z. Li, Y. Cui, J. Wang, C. Liu, J. Wang, T. Xu, T. Lu, H. Zhang, J. Lu, S. Ma, H. Fan, and S. Tang, "Characterization of microstructure and mechanical properties of stellite 6 part fabricated by wire arc additive manufacturing," *Metals*, vol. 9, no. 4, p. 474, apr 2019.

[191] G. Marinelli, F. Martina, S. Ganguly, and S. Williams, "Development of Wire + Arc additive manufacture for the production of large-scale unalloyed tungsten components," *International Journal of Refractory Metals and Hard Materials*, vol. 82, pp. 329–335, aug 2019.

[192] S. Jhavar, N. K. Jain, and C. P. Paul, "Development of micro-plasma transferred arc (μ-PTA) wire deposition process for additive layer manufacturing applications," *Journal of Materials Processing Technology*, vol. 214, no. 5, pp. 1102–1110, may 2014.

[193] X. Ren, C. Yu, and W. Zhang, "The Microstructure and Mechanical Properties of 308L Alloy Fabricated by Micro-plasma Arc Additive Manufacturing," *Journal of Physics: Conference Series*, vol. 1347, p. 12070, 2019.

[194] Y. Feng, B. Zhan, J. He, and K. Wang, "The double-wire feed and plasma arc additive manufacturing process for deposition in Cr-Ni stainless steel," *Journal of Materials Processing Technology*, vol. 259, pp. 206–215, sep 2018.

[195] J. J. Lin, Y. H. Lv, Y. X. Liu, B. S. Xu, Z. Sun, Z. G. Li, and Y. X. Wu, "Microstructural evolution and mechanical properties of Ti-6Al-4V wall deposited by pulsed plasma arc additive manufacturing," *Materials and Design*, vol. 102, pp. 30–40, jul 2016.

[196] J. Lin, Y. Lv, Y. Liu, Z. Sun, K. Wang, Z. Li, Y. Wu, and B. Xu, "Microstructural evolution and mechanical property of Ti-6Al-4V wall deposited by continuous plasma arc additive manufacturing without post heat treatment," *Journal of the Mechanical Behavior of Biomedical Materials*, vol. 69, pp. 19–29, may 2017.

[197] F. Xu, Y. Lv, Y. Liu, F. Shu, P. He, and B. Xu, "Microstructural Evolution and Mechanical Properties of Inconel 625 Alloy during Pulsed Plasma Arc Deposition Process," *Journal of Materials Science and Technology*, vol. 29, no. 5, pp. 480–488, may 2013.

[198] J. Gockel, J. Beuth, and K. Taminger, "Integrated control of solidification microstructure and melt pool dimensions in electron beam wire feed additive manufacturing of ti-6al-4v," *Additive Manufacturing*, vol. 1, pp. 119–126, 2014.

[199] H. Suo, Z. Chen, J. Liu, S. Gong, and J. Xiao, "Microstructure and Mechanical Properties of Ti-6Al-4V by Electron Beam Rapid Manufacturing," *Rare Metal Materials and Engineering*, vol. 43, no. 4, pp. 780–785, 2014.

[200] Z. Liu, Z. B. Zhao, J. R. Liu, L. Wang, S. X. Zhu, G. Yang, S. L. Gong, Q. J. Wang, and R. Yang, "Deformation behaviors of as-built and hot isostatically pressed Ti-6Al-4V alloys fabricated via electron beam rapid manufacturing," *Journal of Materials Science and Technology*, vol. 35, no. 11, pp. 2552–2558, 2019.

[201] Z. Liu, Z. Zhao, J. Liu, L. Wang, G. Yang, S. Gong, Q. Wang, and R. Yang, "Effect of α texture on the tensile deformation behavior of TiâĂŞ6AlâĂŞ4V alloy produced via electron beam rapid manufacturing," *Materials Science and Engineering A*, vol. 742, no. September 2018, pp. 508–516, 2019.

[202] Z. Liu, Z. Zhao, J. Liu, Q. Wang, Z. Guo, Z. Liu, Y. Zeng, G. Yang, and S. Gong, "Effects of solution-aging treatments on microstructure features, mechanical properties and damage behaviors of additive manufactured TiâĂŞ6AlâĂŞ4V alloy," *Materials Science and Engineering: A*, vol. 800, p. 140380, 2021.

[203] X. Tao, Z. Yao, S. Zhang, Z. Li, and Y. Xu, "Correlation Between Heat-Treated Microstructure and Mechanical and Fretting Wear Behavior of Electron Beam Freeform-Fabricated Ti6Al4V Alloy," *JOM*, vol. 71, no. 7, pp. 2313–2320, jul 2019.

[204] Q. Tang, S. Pang, B. Chen, H. Suo, and J. Zhou, "A three dimensional transient model for heat transfer and fluid flow of weld pool during electron beam freeform fabrication of Ti-6-Al-4-V alloy," *International Journal of Heat and Mass Transfer*, vol. 78, pp. 203–215, 2014.

[205] A. Manjunath, V. Anandakrishnan, S. Ramachandra, and K. Parthiban, "Experimental investigations on the effect of pre-positioned wire electron beam additive manufacturing process parameters on the layer geometry of titanium 6Al4V," *Materials Today: Proceedings*, vol. 21, pp. 766–772, 2020.

[206] F. Pixner, F. Warchomicka, P. Peter, A. Steuwer, M. H. Colliander, R. Pederson, and N. Enzinger, "Wire-based additive manufacturing of ti-6al-4v using electron beam technique," *Materials*, vol. 13, no. 15, 2020.

[207] F. Pixner, R. Buzolin, S. Schönfelder, D. Theuermann, F. Warchomicka, and N. Enzinger, "Contactless temperature measurement in wire-based electron beam additive manufacturing Ti-6Al-4V," *Welding in the World*, 2021.

[208] K. N. Kalashnikov, V. E. Rubtsov, N. L. Savchenko, T. A. Kalashnikova, K. S. Osipovich, A. A. Eliseev, and A. V. Chumaevskii, "The effect of wire feed geometry on electron beam freeform 3D printing of complex-shaped samples from Ti-6Al-4V alloy," *The International Journal of Advanced Manufacturing Technology*, vol. 105, no. 7, pp. 3147–3156, 2019.

[209] B. J. Hayes, B. W. Martin, B. Welk, S. J. Kuhr, T. K. Ales, D. A. Brice, I. Ghamarian, A. H. Baker, C. V. Haden, D. G. Harlow, H. L. Fraser, and P. C. Collins, "Predicting tensile properties of Ti-6Al-4V produced via directed energy deposition," *Acta Materialia*, vol. 133, pp. 120–133, jul 2017.

[210] R. W. Bush and C. A. Brice, "Elevated temperature characterization of electron beam freeform fabricated Ti-6Al-4V and dispersion strengthened Ti-8Al-1Er," *Materials Science and Engineering A*, vol. 554, pp. 12–21, 2012.

[211] D. Xu, H. Wang, X. Tao, Z. Yao, S. Zhang, and M. Oleksander, "Investigation on Microstructure, Hardness and Wear Resistance of Electron Beam Wire-Feeding Deposited Inconel 718 Alloy Coatings," *Metals and Materials International*, 2019.

[212] J. Wang, Z. Pan, D. Cuiuri, and H. Li, "Phase constituent control and correlated properties of titanium aluminide intermetallic alloys through dual-wire arc additive manufacturing," *Materials Letters*, vol. 242, pp. 111–114, may 2019.

[213] T. E. Abioye, P. K. Farayibi, and A. T. Clare, "A comparative study of Inconel 625 laser cladding by wire and powder feedstock," *Materials and Manufacturing Processes*, vol. 32, no. 14, pp. 1653–1659, oct 2017.

[214] A. Simchi, "The role of particle size on the laser sintering of iron powder," *Metallurgical and Materials Transactions B: Process Metallurgy and Materials Processing Science*, vol. 35, no. 5, pp. 937–948, oct 2004.

[215] V. Murav'ev, R. Krupskii, R. Fizulakov, and P. Demyshev, "Effect of the quality of filler wire on the formation of pores in welding of titanium alloys," *Welding International*, vol. 22, no. 12, pp. 853–858, 2008.

[216] G. Langelandsvik, M. Grandcolas, K. G. Skorpen, T. Furu, O. M. Akselsen, and H. J. Roven, "Development of al-tic wire feedstock for additive manufacturing by metal screw extrusion," *Metals*, vol. 10, no. 11, 2020.

[217] E. Ryan, T. Sabin, J. Watts, and M. Whiting, "The influence of build parameters and wire batch on porosity of wire and arc additive manufactured aluminium alloy 2319," *Journal of Materials Processing Technology*, vol. 262, pp. 577–584, 2018.

[218] J. L. Gu, J. L. Ding, B. Q. Cong, J. Bai, H. M. Gu, S. W. Williams, and Y. C. Zhai, "The influence of wire properties on the quality and performance of wire+arc additive manufactured aluminium parts," in *Materials Science and Advanced Technologies in Manufacturing II*, ser. Ad-

vanced Materials Research, vol. 1081. Trans Tech Publications Ltd, 2 2015, pp. 210–214.
[219] N. V. Muravyev, K. A. Monogarov, U. Schaller, I. V. Fomenkov, and A. N. Pivkina, "Progress in Additive Manufacturing of Energetic Materials: Creating the Reactive Microstructures with High Potential of Applications," *Propellants, Explosives, Pyrotechnics*, vol. 44, no. 8, pp. 941–969, aug 2019.
[220] F. Montevecchi, G. Venturini, N. Grossi, A. Scippa, and G. Campatelli, "Heat accumulation prevention in Wire-Arc-Additive-Manufacturing using air jet impingement," *Manufacturing Letters*, vol. 17, pp. 14–18, aug 2018.
[221] J. V. Gordon, C. V. Haden, H. F. Nied, R. P. Vinci, and D. G. Harlow, "Fatigue crack growth anisotropy, texture and residual stress in austenitic steel made by wire and arc additive manufacturing," *Materials Science and Engineering A*, vol. 724, pp. 431–438, may 2018.
[222] A. Yadollahi, N. Shamsaei, S. M. Thompson, A. Elwany, and L. Bian, "Mechanical and microstructural properties of selective laser melted 17-4 ph stainless steel," in *ASME International Mechanical Engineering Congress and Exposition, Proceedings (IMECE)*, vol. 2A-2015. American Society of Mechanical Engineers (ASME), mar 2015.
[223] R. Rashid, S. H. Masood, D. Ruan, S. Palanisamy, R. A. Rahman Rashid, and M. Brandt, "Effect of scan strategy on density and metallurgical properties of 17-4PH parts printed by Selective Laser Melting (SLM)," *Journal of Materials Processing Technology*, vol. 249, pp. 502–511, nov 2017.
[224] Z. Hu, H. Zhu, H. Zhang, and X. Zeng, "Experimental investigation on selective laser melting of 17-4PH stainless steel," *Optics and Laser Technology*, vol. 87, pp. 17–25, jan 2017.
[225] S. Pasebani, M. Ghayoor, S. Badwe, H. Irrinki, and S. V. Atre, "Effects of atomizing media and post processing on mechanical properties of 17-4 PH stainless steel manufactured via selective laser melting," *Additive Manufacturing*, vol. 22, pp. 127–137, aug 2018.
[226] S. D. Meredith, J. S. Zuback, J. S. Keist, and T. A. Palmer, "Impact of composition on the heat treatment response of additively manufactured 17âĂŞ4 PH grade stainless steel," *Materials Science and Engineering A*, vol. 738, pp. 44–56, dec 2018.
[227] B. C. Salzbrenner, J. M. Rodelas, J. D. Madison, B. H. Jared, L. P. Swiler, Y. L. Shen, and B. L. Boyce, "High-throughput stochastic tensile performance of additively manufactured stainless steel," *Journal of Materials Processing Technology*, vol. 241, pp. 1–12, mar 2017.
[228] A. Bayode, S. Pityana, E. T. Akinlabi, and M. B. Shongwe, "Effect of scanning speed on laser deposited 17-4PH stainless steel," in *Proceedings of 2017 8th International Conference on Mechanical and Intelligent Manufacturing Technologies, ICMIMT 2017*. Institute of Electrical and Electronics Engineers Inc., may 2017, pp. 1–5.
[229] I. Mathoho, E. T. Akinlabi, N. Arthur, M. Tlotleng, and B. Masina, "Metallurgical Characteristics of Laser Peened 17-4 PH SS Processed by LENS Technique," in *Minerals, Metals and Materials Series*. Springer International Publishing, 2019, pp. 279–285.
[230] Y. Fu, H. Zhang, G. Wang, and H. Wang, "Investigation of mechanical properties for hybrid deposition and micro-rolling of bainite steel," *Journal of Materials Processing Technology*, vol. 250, pp. 220–227, dec 2017.
[231] E. Uhlmann, R. Kersting, T. B. Klein, M. F. Cruz, and A. V. Borille, "Additive Manufacturing of Titanium Alloy for Aircraft Components," in *Procedia CIRP*, vol. 35. Elsevier B.V., jan 2015, pp. 55–60.
[232] D. Banerjee and J. C. Williams, "Perspectives on titanium science and technology," *Acta Materialia*, vol. 61, no. 3, pp. 844–879, feb 2013.
[233] M. Kikuchi, "The use of cutting temperature to evaluate the machinability of titanium alloys," *Acta Biomaterialia*, vol. 5, no. 2, pp. 770–775, feb 2009.
[234] Y. Zhu, X. Tian, J. Li, and H. Wang, "The anisotropy of laser melting deposition additive manufacturing Ti-6.5Al-3.5Mo-1.5Zr-0.3Si titanium alloy," *Materials and Design*, vol. 67, pp. 538–542, feb 2015.
[235] Q. Zhang, J. Chen, Z. Zhao, H. Tan, X. Lin, and W. Huang, "Microstructure and anisotropic tensile behavior of laser additive manufactured TC21 titanium alloy," *Materials Science and Engineering A*, vol. 673, pp. 204–212, 2016.
[236] J. Alcisto, A. Enriquez, H. Garcia, S. Hinkson, T. Steelman, E. Silverman, P. Valdovino, H. Gigerenzer, J. Foyos, J. Ogren, J. Dorey, K. Karg, T. McDonald, and O. S. Es-Said, "Tensile properties and microstructures of laser-formed Ti-6Al-4V," *Journal of Materials Engineering and Performance*, vol. 20, no. 2, pp. 203–212, 2011.
[237] Q. Zhang, J. Chen, L. Wang, H. Tan, X. Lin, and W. Huang, "Solidification Microstructure of Laser Additive Manufactured Ti-6Al-2Zr-2Sn-3Mo-1.5Cr-2Nb Titanium Alloy," *Journal of Materials Science and Technology*, vol. 32, no. 4, pp. 381–386, 2016.
[238] M. Rizwan, J. Lu, F. Chen, R. Chai, R. Ullah, Y. Zhang, and Z. Zhang, "Microstructure Evolution and Mechanical Behavior of Laser Melting Deposited TA15 Alloy at 500ÂăÂřC under In-Situ Tension in SEM," *Acta Metallurgica Sinica (English Letters)*, pp. 1–12, mar 2021.
[239] M. J. Bermingham, D. H. StJohn, J. Krynen, S. Tedman-Jones, and M. S. Dargusch, "Promoting the columnar to equiaxed transition and grain refinement of titanium alloys during additive manufacturing," *Acta Materialia*, vol. 168, pp. 261–274, apr 2019.
[240] Q. Zhang, J. Chen, X. Lin, H. Tan, and W. D. Huang, "Grain morphology control and texture characterization of laser solid formed Ti6Al2Sn2Zr3Mo1.5Cr2Nb titanium alloy," *Journal of Materials Processing Technology*, vol. 238, pp. 202–211, dec 2016.
[241] E. Brandl and D. Greitemeier, "Microstructure of additive layer manufactured Ti-6Al-4V after exceptional post heat treatments," *Materials Letters*, vol. 81, pp. 84–87, 2012.
[242] V. Alfieri, F. Caiazzo, and V. Sergi, "Autogenous laser welding of AA 2024 aluminium alloy: Process issues and bead features," in *Procedia CIRP*, vol. 33. Elsevier B.V., jan 2015, pp. 406–411.
[243] A. Haboudou, P. Peyre, A. B. Vannes, and G. Peix, "Reduction of porosity content generated during Nd: YAG laser welding of A356 and AA5083 aluminium alloys," *Materials Science and Engineering A*, vol. 363, no. 1-2, pp. 40–52, dec 2003.
[244] R. Xiao and X. Zhang, "Problems and issues in laser beam welding of aluminum-lithium alloys," pp. 166–175, apr 2014.
[245] C. Borsellino, G. Di Bella, and V. F. Ruisi, "Adhesive joining of aluminium AA6082: The effects of resin and surface treatment," *International Journal of Adhesion and Adhesives*, vol. 29, no. 1, pp. 36–44, jan 2009.
[246] S. Thapliyal, "Challenges associated with the wire arc additive manufacturing (WAAM) of aluminum alloys," *Materials Research Express*, vol. 6, no. 11, p. 112006, 2019.
[247] J. Hatch, *Aluminum: Properties and Physical Metallurgy (Livre numérique Google)*. American Society for Metals, 1984, vol. 1984.
[248] M. Kristoffersen, M. Costas, T. Koenis, V. Brøtan, C. O. Paulsen, and T. Børvik, "On the ballistic perforation resistance of additive manufactured AlSi10Mg aluminium plates," *International Journal of Impact Engineering*, vol. 137, p. 103476, mar 2020.
[249] M. Javidani, J. Arreguin-Zavala, J. Danovitch, Y. Tian, and M. Brochu, "Additive Manufacturing of AlSi10Mg Alloy Using Direct Energy Deposition: Microstructure and Hardness Characterization," *Journal of Thermal Spray Technology*, vol. 26, no. 4, pp. 587–597, apr 2017.
[250] S. Li, L. J. Zhang, J. Ning, X. Wang, G. F. Zhang, J. X. Zhang, S. J. Na, and B. Fatemeh, "Comparative study on the microstructures and properties of wire+arc additively manufactured 5356 aluminium alloy with argon and nitrogen as the shielding gas," *Additive Manufacturing*, vol. 34, p. 101206, aug 2020.
[251] M. Köhler, S. Fiebig, J. Hensel, and K. Dilger, "Wire and Arc Additive Manufacturing of Aluminum Components," *Metals*, vol. 9, no. 5, p. 608, may 2019.
[252] L. Wahsh, M. Azzam, M. Turky, H. Salem, F. Hamdy, A. Mansour, and A. ElShater, "Parameter selection for wire arc additive manufacturing (waam) process," 01 2018, pp. 78–85.
[253] L. Wang, Y. Suo, Z. Liang, D. Wang, and Q. Wang, "Effect of titanium powder on microstructure and mechanical properties of wire + arc additively manufactured Al-Mg alloy," *Materials Letters*, vol. 241, pp. 231–234, apr 2019.
[254] H. Wang, W. Jiang, J. Ouyang, and R. Kovacevic, "Rapid prototyping of 4043 Al-alloy parts by VP-GTAW," *Journal of Materials Processing Technology*, vol. 148, no. 1, pp. 93–102, may 2004.
[255] Y. Nie, P. Zhang, X. Wu, G. Li, H. Yan, and Z. Yu, "Rapid prototyping of 4043 Al-alloy parts by cold metal transfer," *Science and Technology of Welding and Joining*, vol. 23, no. 6, pp. 527–535, aug 2018.
[256] A. G. Ortega, L. Corona Galvan, M. Salem, K. Moussaoui, S. Segonds, S. Rouquette, and F. Deschaux-Beaume, "Characterisation of 4043 aluminium alloy deposits obtained by wire and arc additive manufacturing

using a Cold Metal Transfer process," *Science and Technology of Welding and Joining*, vol. 24, no. 6, pp. 538–547, aug 2019.

[257] Q. Miao, D. Wu, D. Chai, Y. Zhan, G. Bi, F. Niu, and G. Ma, "Comparative study of microstructure evaluation and mechanical properties of 4043 aluminum alloy fabricated by wire-based additive manufacturing," *Materials and Design*, vol. 186, p. 108205, jan 2020.

[258] C. H. Cáceres, C. J. Davidson, and J. R. Griffiths, "The deformation and fracture behaviour of an AlSiMg casting alloy," *Materials Science and Engineering A*, vol. 197, no. 2, pp. 171–179, jul 1995.

[259] C. H. Cáceres and Q. G. Wang, "Dendrite cell size and ductility of Al-Si-Mg casting alloys: Spear and Gardner revisited," pp. 157–162, 1996.

[260] C. H. Caceres, C. J. Davidson, J. R. Griffiths, and Q. G. Wang, "The effect of Mg on the microstructure and mechanical behavior of Al-Si-Mg casting alloys," *Metallurgical and Materials Transactions A: Physical Metallurgy and Materials Science*, vol. 30, no. 10, pp. 2611–2618, oct 1999.

[261] G. D. Bhasale, A. Sood, S. R. Singh, A. Pandey, and A. Shrivastava, "High Temperature Corrosion of Additively Manufactured Inconel 625," in *Minerals, Metals and Materials Series*. Springer, 2020, pp. 1329–1338.

[262] B. Dubiel and J. Sieniawski, "Precipitates in additively manufactured inconel 625 superalloy," *Materials*, vol. 12, no. 7, p. 1144, apr 2019.

[263] L. C. Valle, A. I. Santana, M. C. Rezende, J. Dille, O. R. Mattos, and L. H. de Almeida, "The influence of heat treatments on the corrosion behaviour of nickel-based alloy 718," *Journal of Alloys and Compounds*, vol. 809, p. 151781, nov 2019.

[264] C. V. Mikler, V. Chaudhary, T. Borkar, V. Soni, D. Choudhuri, R. V. Ramanujan, and R. Banerjee, "Laser additive processing of Ni-Fe-V and Ni-Fe-Mo Permalloys: Microstructure and magnetic properties," *Materials Letters*, vol. 192, pp. 9–11, apr 2017.

[265] C. V. Mikler, V. Chaudhary, T. Borkar, V. Soni, D. Jaeger, X. Chen, R. Contieri, R. V. Ramanujan, and R. Banerjee, "Laser Additive Manufacturing of Magnetic Materials," *Jom*, vol. 69, no. 3, pp. 532–543, mar 2017.

[266] G. L. Makar and J. Kruger, "Corrosion of magnesium," *International Materials Reviews*, vol. 38, no. 3, pp. 138–153, 1993.

[267] Y. Wan, G. Xiong, H. Luo, F. He, Y. Huang, and X. Zhou, "Preparation and characterization of a new biomedical magnesium-calcium alloy," *Materials and Design*, vol. 29, no. 10, pp. 2034–2037, dec 2008.

[268] M. Murphy, M. Turski, W. Warfield, and P. Lyon, "The effect of changes in hydraulic fracking fluid chemistries on the dissolution rate of dissolvable magnesium frack plug components," in *Proceedings - SPE Annual Technical Conference and Exhibition*, vol. 2019-Septe. Society of Petroleum Engineers, sep 2019.

[269] Y. Cai, L. Wan, Z. H. Guo, C. Y. Sun, D. J. Yang, Q. D. Zhang, and Y. L. Li, "Hot deformation characteristics of AZ80 magnesium alloy: Work hardening effect and processing parameter sensitivities," *Materials Science and Engineering A*, vol. 687, pp. 113–122, feb 2017.

[270] P. Frigola, R. Agustsson, S. Boucher, a. Murokh, H. Badakov, a. Fukasawa, P. Musumeci, J. Rosenzweig, G. Travish, L. Faillace, R. La, D. Cormier, and T. Mahale, "Development of Solid Freeform Fabrication (Sff) for the Production of Rf Photoinjectors Ebm Fabrication Process," in *Proceedings of the 23rd Particle Accelerator Conference*, 2009, pp. 2015–2017.

[271] A. Röttger, K. Geenen, M. Windmann, F. Binner, and W. Theisen, "Comparison of microstructure and mechanical properties of 316 L austenitic steel processed by selective laser melting with hot-isostatic pressed and cast material," *Materials Science and Engineering A*, vol. 678, pp. 365–376, dec 2016.

[272] Z. Xu, J. W. Murray, C. J. Hyde, and A. T. Clare, "Effect of post processing on the creep performance of laser powder bed fused Inconel 718," *Additive Manufacturing*, vol. 24, pp. 486–497, dec 2018.

[273] M. E. Aydinöz, F. Brenne, M. Schaper, C. Schaak, W. Tillmann, J. Nellesen, and T. Niendorf, "On the microstructural and mechanical properties of post-treated additively manufactured Inconel 718 superalloy under quasi-static and cyclic loading," *Materials Science and Engineering A*, vol. 669, pp. 246–258, jul 2016.

[274] Y. Tian, J. Shen, S. Hu, J. Han, Q. Wang, and Y. Cai, "Effects of ultrasonic peening treatment layer by layer on microstructure of components fabricated by wire and arc additive manufacturing," *Materials Letters*, vol. 284, p. 128917, 2021.

[275] B. Parvaresh, R. Salehan, and R. Miresmaeili, "Investigating Isotropy of Mechanical and Wear Properties in As-Deposited and Inter-Layer Cold Worked Specimens Manufactured by Wire Arc Additive Manufacturing," *Metals and Materials International*, vol. 27, no. 1, pp. 92–105, 2021.

[276] I. Tabernero, A. Calleja, A. Lamikiz, and L. N. López De Lacalle, "Optimal parameters for 5-axis Laser cladding," *Procedia Engineering*, vol. 63, pp. 45–52, jan 2013.

[277] A. Calleja, I. Tabernero, A. Fernández, A. Celaya, A. Lamikiz, and L. N. López De Lacalle, "Improvement of strategies and parameters for multi-axis laser cladding operations," *Optics and Lasers in Engineering*, vol. 56, pp. 113–120, may 2014.

[278] Yamazaki Mazak Corporation, "INTEGREX i-400AM." [Online]. Available: https://www.mazakusa.com/machines/integrex-i-400am/

[279] Uk.dmgmori.com, "LASERTEC 65 3D hybrid - ADDITIVE MANUFACTURING Machines by DMG MORI," 2018. [Online]. Available: https://uk.dmgmori.com/products/machines/advanced-technology/additive-manufacturing/powder-nozzle/lasertec-65-3d-hybrid

[280] G. C. Anzalone, C. Zhang, B. Wijnen, P. G. Sanders, and J. M. Pearce, "A low-cost open-source metal 3-D printer," *IEEE Access*, vol. 1, pp. 803–810, 2013.

[281] Y. Nilsiam, A. Haselhuhn, B. Wijnen, P. Sanders, and J. M. Pearce, "Integrated voltage-current monitoring and control of gas metal arc weld magnetic ball-jointed open source 3-D printer," *Machines*, vol. 3, no. 4, pp. 339–351, nov 2015.

[282] X. Lu, Y. F. Zhou, X. L. Xing, L. Y. Shao, Q. X. Yang, and S. Y. Gao, "Open-source wire and arc additive manufacturing system: formability, microstructures, and mechanical properties," *International Journal of Advanced Manufacturing Technology*, vol. 93, no. 5-8, pp. 2145–2154, nov 2017.

[283] C. Wu, C. Dai, G. Fang, Y. J. Liu, and C. C. Wang, "RoboFDM: A robotic system for support-free fabrication using FDM," in *Proceedings - IEEE International Conference on Robotics and Automation*. IEEE, may 2017, pp. 1175–1180.

[284] C. Dai, C. C. Wang, C. Wu, S. Lefebvre, G. Fang, and Y. J. Liu, "Support-free volume printing by multi-axis motion," *ACM Transactions on Graphics*, vol. 37, no. 4, pp. 1–14, jul 2018.

[285] F. Li, S. Chen, Z. Wu, and Z. Yan, "Adaptive process control of wire and arc additive manufacturing for fabricating complex-shaped components," *International Journal of Advanced Manufacturing Technology*, vol. 96, no. 1-4, pp. 871–879, apr 2018.

[286] X. Zhang, M. Li, J. H. Lim, Y. Weng, Y. W. D. Tay, H. Pham, and Q. C. Pham, "Large-scale 3D printing by a team of mobile robots," *Automation in Construction*, vol. 95, pp. 98–106, nov 2018.

[287] M. K. Jouaneh, Z. Wang, and D. A. Dornfeld, "Trajectory Planning for Coordinated Motion of a Robot and a Positioning Table: Part 1âĂŤPath Specification," *IEEE Transactions on Robotics and Automation*, vol. 6, no. 6, pp. 735–745, 1990.

[288] M. Chalvin, S. Campocasso, T. Baizeau, and V. Hugel, "Automatic multi-axis path planning for thinwall tubing through robotized wire deposition," *Procedia CIRP*, vol. 79, pp. 89–94, jan 2019.

[289] D. Ding, Z. Pan, D. Cuiuri, H. Li, N. Larkin, and S. Van Duin, "Automatic multi-direction slicing algorithms for wire based additive manufacturing," *Robotics and Computer-Integrated Manufacturing*, vol. 37, pp. 139–150, feb 2016.

[290] L. Ren, T. Sparks, J. Ruan, and F. Liou, "Process planning strategies for solid freeform fabrication of metal parts," *Journal of Manufacturing Systems*, vol. 27, no. 4, pp. 158–165, oct 2008.

[291] J. Ruan, T. E. Sparks, A. Panackal, F. W. Liou, K. Eiamsa-Ard, K. Slattery, H. N. Chou, and M. Kinsella, "Automated slicing for a multiaxis metal deposition system," *Journal of Manufacturing Science and Engineering, Transactions of the ASME*, vol. 129, no. 2, pp. 303–310, apr 2007.

[292] R. Dwivedi, S. Zekovic, and R. Kovacevic, "A novel approach to fabricate uni-directional and branching slender structures using laser-based direct metal deposition," *International Journal of Machine Tools and Manufacture*, vol. 47, no. 7-8, pp. 1246–1256, jun 2007.

[293] T. A. Rodrigues, V. Duarte, R. M. Miranda, T. G. Santos, and J. P. Oliveira, "Current status and perspectives on wire and arc additive manufacturing (WAAM)," *Materials*, vol. 12, no. 7, p. 1121, apr 2019.

[294] Y. M. Zhang, Y. Chen, P. Li, and A. T. Male, "Weld deposition-based

rapid prototyping: A preliminary study," *Journal of Materials Processing Technology*, vol. 135, no. 2-3 SPEC., pp. 347–357, apr 2003.

[295] D. Ding, Z. Pan, D. Cuiuri, H. Li, S. Van Duin, and N. Larkin, "Bead modelling and implementation of adaptive MAT path in wire and arc additive manufacturing," *Robotics and Computer-Integrated Manufacturing*, vol. 39, pp. 32–42, jun 2016.

[296] H. Zhao, F. Gu, Q. X. Huang, J. Garcia, Y. Chen, C. Tu, B. Benes, H. Zhang, D. Cohen-Or, and B. Chen, "Connected fermat spirals for layered fabrication," in *ACM Transactions on Graphics*, vol. 35, no. 4. Association for Computing Machinery, jul 2016, pp. 1–10.

[297] F. Ren, Y. Sun, and D. Guo, "Combined reparameterization-based spiral toolpath generation for five-axis sculptured surface machining," *International Journal of Advanced Manufacturing Technology*, vol. 40, no. 7-8, pp. 760–768, feb 2009.

[298] M. Bertoldi, M. Yardimci, C. M. Pistor, and S. I. Guceri, "Domain Decomposition and Space Filling Curves in Toolpath Planning and Generation," in *1998 International Solid Freeform Fabrication Symposium*. Austin, Texas: The University of Texas at Austin, 1998, pp. 267–276.

[299] W. K. Chiu, Y. C. Yeung, and K. M. Yu, "Toolpath generation for layer manufacturing of fractal objects," *Rapid Prototyping Journal*, vol. 12, no. 4, pp. 214–221, 2006.

[300] T. Wasser, A. D. Jayal, and C. Pistor, "Implementation and Evaluation of Novel Buildstyles in Fused Deposition Modeling (FDM)," in *1999 International Solid Freeform Fabrication Symposium*. Austin, Texas: The University of Texas at Austin, 1999, pp. 95–102.

[301] P. Singh and D. Dutta, "Offset slices for multidirection layered deposition," *Journal of Manufacturing Science and Engineering, Transactions of the ASME*, vol. 130, no. 1, feb 2008.

[302] L. Shapira, A. Shamir, and D. Cohen-Or, "Consistent mesh partitioning and skeletonisation using the shape diameter function," *Visual Computer*, vol. 24, no. 4, pp. 249–259, apr 2008.

[303] M. R. Dunlavey, "Efficient Polygon-Filling Algorithms for Raster Displays," *ACM Transactions on Graphics (TOG)*, vol. 2, no. 4, pp. 264–273, jan 1983.

[304] S. C. Park and B. K. Choi, "Tool-path planning for direction-parallel area milling," *CAD Computer Aided Design*, vol. 32, no. 1, pp. 17–25, jan 2000.

[305] V. T. Rajan, V. Srinivasan, and K. A. Tarabanis, "The optimal zigzag direction for filling a two-dimensional region," *Rapid Prototyping Journal*, vol. 7, no. 5, pp. 231–241, dec 2001.

[306] H. Li, Z. Dong, and G. W. Vickers, "Optimal toolpath pattern identification for single island, sculptured part rough machining using fuzzy pattern analysis," *Computer-Aided Design*, vol. 26, no. 11, pp. 787–795, nov 1994.

[307] R. T. Farouki, T. Koenig, K. A. Tarabanis, J. U. Korein, and J. S. Batchelder, "Path planning with offset curves for layered fabrication processes," *Journal of Manufacturing Systems*, vol. 14, no. 5, pp. 355–368, jan 1995.

[308] Y. Yang, H. T. Loh, J. Y. Fuh, and Y. G. Wang, "Equidistant path generation for improving scanning efficiency in layered manufacturing," *Rapid Prototyping Journal*, vol. 8, no. 1, pp. 30–37, 2002.

[309] H. Wang, P. Jang, and J. A. Stori, "A metric-based approach to two-dimensional (2D) tool-path optimization for high-speed machining," *Journal of Manufacturing Science and Engineering, Transactions of the ASME*, vol. 127, no. 1, pp. 33–48, feb 2005.

[310] P. Kulkarni, A. Marsan, and D. Dutta, "Review of process planning techniques in layered manufacturing," *Rapid Prototyping Journal*, vol. 6, no. 1, pp. 18–35, 2000.

[311] H. Blum, "A Transformation for Extracting New Descriptors of Shape," in *Models for the Perception of Speech and Visual Form*, W. Wathen-Dunn, Ed. Cambridge: MIT Press, 1967, pp. 362–380.

[312] E. Berger, K. Conley, J. Faust, T. Foote, B. Gerkey, J. Leibs, M. Quigley, and R. Wheeler, "ROS - Introduction." [Online]. Available: https://wiki.ros.org/ROS/Introduction

[313] S. Edwards, J. Nicho, and J. Meyer, "The Descartes Planning Library for Semi-constrained Cartesian Trajectories," 2015. [Online]. Available: https://wiki.ros.org/descartes

[314] L. Armstrong, "Optimization Motion Planning with Tesseract and TrajOpt for Industrial Applications," 2018. [Online]. Available: https://rosindustrial.org/news/2018/7/5/optimization-motion-planning-with-tesseract-and-trajopt-for-industrial-applications

[315] V. Lamoine, "ROS Additive Manufacturing," 2017. [Online]. Available: https://rosindustrial.org/news/2017/9/12/ros-additive-manufacturing

[316] C. Meola, S. Boccardi, and G. maria Carlomagno, "Chapter 3 - Infrared Thermography Basics," C. Meola, S. Boccardi, and G. m. B. T. I. T. i. t. E. o. A. C. M. Carlomagno, Eds. Woodhead Publishing, 2017, pp. 57–83.

[317] G. Tapia and A. Elwany, "A Review on Process Monitoring and Control in Metal-Based Additive Manufacturing," *Journal of Manufacturing Science and Engineering*, vol. 136, no. 6, p. 060801, oct 2014.

[318] T. Purtonen, A. Kalliosaari, and A. Salminen, "Monitoring and adaptive control of laser processes," *Physics Procedia*, vol. 56, no. C, pp. 1218–1231, jan 2014.

[319] S. K. Everton, M. Hirsch, P. I. Stavroulakis, R. K. Leach, and A. T. Clare, "Review of in-situ process monitoring and in-situ metrology for metal additive manufacturing," *Materials and Design*, vol. 95, pp. 431–445, apr 2016.

[320] C. Doumanidis and Y. M. Kwak, "Geometry modeling and control by infrared and laser sensing in thermal manufacturing with material deposition," *Journal of Manufacturing Science and Engineering, Transactions of the ASME*, vol. 123, no. 1, pp. 45–52, feb 2001.

[321] M. Iravani-Tabrizipour and E. Toyserkani, "An image-based feature tracking algorithm for real-time measurement of clad height," *Machine Vision and Applications*, vol. 18, no. 6, pp. 343–354, nov 2007.

[322] J. Xiong, G. Zhang, Z. Qiu, and Y. Li, "Vision-sensing and bead width control of a single-bead multi-layer part: Material and energy savings in GMAW-based rapid manufacturing," *Journal of Cleaner Production*, vol. 41, pp. 82–88, feb 2013.

[323] J. Xiong and G. Zhang, "Adaptive control of deposited height in GMAW-based layer additive manufacturing," *Journal of Materials Processing Technology*, vol. 214, no. 4, pp. 962–968, apr 2014.

[324] J. Xiong, Z. Yin, and W. Zhang, "Closed-loop control of variable layer width for thin-walled parts in wire and arc additive manufacturing," *Journal of Materials Processing Technology*, vol. 233, pp. 100–106, jul 2016.

[325] S. Pal, S. K. Pal, and A. K. Samantaray, "Sensor based weld bead geometry prediction in pulsed metal inert gas welding process through artificial neural networks," *International Journal of Knowledge-Based and Intelligent Engineering Systems*, vol. 12, no. 2, pp. 101–114, 2008.

[326] N. Akkas, D. Karayel, S. S. Ozkan, A. OÇğur, and B. Topal, "Modeling and analysis of the weld bead geometry in submerged arc welding by using adaptive neurofuzzy inference system," *Mathematical Problems in Engineering*, vol. 2013, pp. 1–10, oct 2013.

[327] Y. Li, Y. Sun, Q. Han, G. Zhang, and I. Horváth, "Enhanced beads overlapping model for wire and arc additive manufacturing of multi-layer multi-bead metallic parts," *Journal of Materials Processing Technology*, vol. 252, pp. 838–848, feb 2018.

[328] D. Hu and R. Kovacevic, "Sensing, modeling and control for laser-based additive manufacturing," *International Journal of Machine Tools and Manufacture*, vol. 43, no. 1, pp. 51–60, jan 2003.

[329] G. Bi, A. Gasser, K. Wissenbach, A. Drenker, and R. Poprawe, "Identification and qualification of temperature signal for monitoring and control in laser cladding," *Optics and Lasers in Engineering*, vol. 44, no. 12, pp. 1348–1359, dec 2006.

[330] ——, "Characterization of the process control for the direct laser metallic powder deposition," *Surface and Coatings Technology*, vol. 201, no. 6, pp. 2676–2683, 2006.

[331] G. Bi, B. Schürmann, A. Gasser, K. Wissenbach, and R. Poprawe, "Development and qualification of a novel laser-cladding head with integrated sensors," *International Journal of Machine Tools and Manufacture*, vol. 47, no. 3-4, pp. 555–561, mar 2007.

[332] L. Tang and R. G. Landers, "Melt pool temperature control for laser metal deposition processes-part I: Online temperature control," *Journal of Manufacturing Science and Engineering, Transactions of the ASME*, vol. 132, no. 1, pp. 0 110 101–0 110 109, feb 2010.

[333] G. Bi, C. N. Sun, and A. Gasser, "Study on influential factors for process monitoring and control in laser aided additive manufacturing," *Journal of Materials Processing Technology*, vol. 213, no. 3, pp. 463–468, mar 2013.

[334] M. H. Farshidianfar, A. Khajepour, and A. Gerlich, "Real-time control of microstructure in laser additive manufacturing," *International Journal of Advanced Manufacturing Technology*, vol. 82, no. 5-8, pp. 1173–1186,

feb 2016.

[335] C. Doumanidis and D. Hardt, "Simultaneous in-process control of heat affected zone and cooling rate during arc welding," *Welding Journal*, vol. 69, no. 5, pp. 186s–196s, may 1990.

[336] C. S. Wu, J. Q. Gao, X. F. Liu, and Y. H. Zhao, "Vision-based measurement of weld pool geometry in constant-current gas tungsten arc welding," *Proceedings of the Institution of Mechanical Engineers, Part B: Journal of Engineering Manufacture*, vol. 217, no. 6, pp. 879–882, jun 2003.

[337] Y. Xu, G. Fang, N. Lv, S. Chen, and J. Jia Zou, "Computer vision technology for seam tracking in robotic GTAW and GMAW," *Robotics and Computer-Integrated Manufacturing*, vol. 32, pp. 25–36, apr 2015.

[338] A. S. Babkin and E. A. Gladkov, "Identification of welding parameters for quality welds in GMAW," *Welding Journal*, vol. 95, no. 1, pp. 37s–46s, 2016.

[339] Z. Feng, J. Chen, and Z. Chen, "Monitoring weld pool surface and penetration using reversed electrode images," *Welding Journal*, vol. 96, no. 10, pp. 367s–375s, 2017.

[340] S. Ríos, P. A. Colegrove, F. Martina, and S. W. Williams, "Analytical process model for wire + arc additive manufacturing," *Additive Manufacturing*, vol. 21, pp. 651–657, may 2018.

[341] A. Heralić, A. K. Christiansson, and B. Lennartson, "Height control of laser metal-wire deposition based on iterative learning control and 3D scanning," *Optics and Lasers in Engineering*, vol. 50, no. 9, pp. 1230–1241, sep 2012.

[342] A. R. Nassar, J. S. Keist, E. W. Reutzel, and T. J. Spurgeon, "Intra-layer closed-loop control of build plan during directed energy additive manufacturing of Ti-6Al-4V," *Additive Manufacturing*, vol. 6, pp. 39–52, apr 2015.

[343] D. Ding, C. Shen, Z. Pan, D. Cuiuri, H. Li, N. Larkin, and S. Van Duin, "Towards an automated robotic arc-welding-based additive manufacturing system from CAD to finished part," *CAD Computer Aided Design*, vol. 73, pp. 66–75, apr 2016.

[344] M. Preissler, C. Zhang, M. Rosenberger, and G. Notni, "Platform for 3D inline process control in additive manufacturing," in *Optical Measurement Systems for Industrial Inspection X*, P. Lehmann, W. Osten, and A. Albertazzi Gonçalves, Eds., vol. 10329. International Society for Optics and Photonics, jun 2017, p. 103290R.

[345] ——, "Approach for Process Control in Additive Manufacturing Through Layer-Wise Analysis with 3-Dimensional Pointcloud Information," in *2018 International Conference on Digital Image Computing: Techniques and Applications, DICTA 2018*. IEEE, dec 2019, pp. 1–6.

[346] Y. Li, Y. F. Li, Q. L. Wang, D. Xu, and M. Tan, "Measurement and defect detection of the weld bead based on online vision inspection," *IEEE Transactions on Instrumentation and Measurement*, vol. 59, no. 7, pp. 1841–1849, jul 2010.

[347] W. Huang and R. Kovacevic, "Development of a real-time laser-based machine vision system to monitor and control welding processes," *International Journal of Advanced Manufacturing Technology*, vol. 63, no. 1-4, pp. 235–248, nov 2012.

[348] J. Xiong and G. Zhang, "Online measurement of bead geometry in GMAW-based additive manufacturing using passive vision," *Measurement Science and Technology*, vol. 24, no. 11, p. 115103, nov 2013.

[349] F. Lü, H. Chen, C. Fan, and S. Chen, "A novel control algorithm for weld pool control," *Industrial Robot*, vol. 37, no. 1, pp. 89–96, jan 2010.

[350] SICK Ltd., "Profiler 2 SHORT RANGE DISTANCE SENSOR OPERATING INSTRUCTIONS," 2019.

[351] S. M. Thompson, L. Bian, N. Shamsaei, and A. Yadollahi, "An overview of Direct Laser Deposition for additive manufacturing; Part I: Transport phenomena, modeling and diagnostics," *Additive Manufacturing*, vol. 8, pp. 36–62, 2015.

[352] C. Li, Z. Y. Liu, X. Y. Fang, and Y. B. Guo, "Residual Stress in Metal Additive Manufacturing," in *Procedia CIRP*, vol. 71. Elsevier B.V., jan 2018, pp. 348–353.

[353] F. Liu, X. Lin, G. Yang, M. Song, J. Chen, and W. Huang, "Recrystallization and its influence on microstructures and mechanical properties of laser solid formed nickel base superalloy Inconel 718," *Rare Metals*, vol. 30, no. SUPPL.1, pp. 433–438, mar 2011.

[354] W. D. Callister and D. G. Rethwisch, *Materials science and engineering : an introduction*, 10th ed. Wiley, 2018.

[355] Q. Zhang, J. Chen, H. Tan, X. Lin, and W. D. Huang, "Influence of solution treatment on microstructure evolution of TC21 titanium alloy with near equiaxed β grains fabricated by laser additive manufacture," *Journal of Alloys and Compounds*, vol. 666, pp. 380–386, 2016.

[356] L. Zhuo, L. Changmeng, L. Dong, and W. Huaming, "Effect of heat treatment on microstructure and tensile properties of laser deposited titanium alloy TC21," *Materials Research Innovations*, vol. 18, no. sup4, pp. S4929–S4932, jul 2014.

[357] Q. Zhang, J. Chen, Z. Qi, X. Lin, H. Tan, and W. Huang, "A Processing Route for Achieving Isotropic Tensile Properties in Laser Solid Formed α+β Titanium Alloy," *Metallurgical and Materials Transactions A: Physical Metallurgy and Materials Science*, vol. 49, no. 8, pp. 3651–3662, 2018.

[358] C. M. Liu, H. M. Wang, X. J. Tian, H. B. Tang, and D. Liu, "Microstructure and tensile properties of laser melting deposited Ti-5Al-5Mo-5V-1Cr-1Fe near β titanium alloy," *Materials Science and Engineering A*, vol. 586, pp. 323–329, 2013.

[359] X. Wu, R. Sharman, J. Mei, and W. Voice, "Microstructure and properties of a laser fabricated burn-resistant Ti alloy," *Materials & Design*, vol. 25, no. 2, pp. 103–109, 2004.

[360] P. L. Blackwell and A. Wisbey, "Laser-aided manufacturing technologies; their application to the near-net shape forming of a high-strength titanium alloy," *Journal of Materials Processing Technology*, vol. 170, no. 1, pp. 268–276, 2005.

[361] H. Deng, L. Chen, W. Qiu, Z. Zheng, Y. Tang, Z. Hu, Y. Wei, Z. Xia, G. Le, J. Tang, and X. Cui, "Microstructure and mechanical properties of as-deposited and heat treated Ti-5Al-5Mo-5V-3Cr-1Zr (Ti-55531) alloy fabricated by laser melting deposition," *Journal of Alloys and Compounds*, vol. 810, p. 151792, 2019.

[362] A. Zhang, D. Liu, X. Wu, and H. Wang, "Effect of heat treatment on microstructure and mechanical properties of laser deposited Ti60A alloy," *Journal of Alloys and Compounds*, vol. 585, pp. 220–228, 2014.

[363] C. Carson, "Heat Treating of Titanium and Titanium Alloys," in *Heat Treating of Nonferrous Alloys*. ASM International, 2016.

[364] F. F. Schmidt and R. A. Wood, "Heat treatment of titanium and titanium alloys," NASA Marshall Space Flight Center, Huntsville, AL, United States, Tech. Rep., 1996.

[365] R. R. Boyer, "Titanium and Its Alloys: Metallurgy, Heat Treatment and Alloy Characteristics," in *Encyclopedia of Aerospace Engineering*. Chichester, UK: John Wiley & Sons, Ltd, dec 2010.

[366] A. Sterling, N. Shamsaei, B. Torries, and S. M. Thompson, "Fatigue Behaviour of Additively Manufactured Ti-6Al-4 v," in *Procedia Engineering*, vol. 133. Elsevier Ltd, jan 2015, pp. 576–589.

[367] S. Leuders, M. Thöne, A. Riemer, T. Niendorf, T. Tröster, H. A. Richard, and H. J. Maier, "On the mechanical behaviour of titanium alloy TiAl6V4 manufactured by selective laser melting: Fatigue resistance and crack growth performance," *International Journal of Fatigue*, vol. 48, pp. 300–307, mar 2013.

[368] P. H. Li, W. G. Guo, K. B. Yuan, Y. Su, J. J. Wang, X. Lin, and Y. P. Li, "Effects of processing defects on the dynamic tensile mechanical behavior of laser-solid-formed Ti-6Al-4 V," *Materials Characterization*, vol. 140, pp. 15–29, jun 2018.

[369] N. Chekir, J. J. Sixsmith, R. Tollett, and M. Brochu, "Laser wire deposition of a large Ti-6AI-4V space component the methodology for creating a functional Ti-6Al-4V satellite part using LWD additive manufacturing is detailed," *Welding Journal*, vol. 98, no. 6, pp. 172S–180S, 2019.

[370] *Nickel Alloy, Corrosion and Heat Resistant, Investment Castings 52.5Ni - 19Cr - 3.0Mo - 5.1(Cb+Ta) - 0.90Ti - 0.60Al - 18Fe Vacuum Melted Homogenization and Solution Heat Treated*, sep 2000.

[371] *Nickel Alloy, Corrosion and Heat-Resistant, Bars, Forgings, and Rings 52.5Ni - 19Cr - 3.0Mo - 5.1Cb (Nb) - 0.90Ti - 0.50Al - 18Fe Consumable Electrode or Vacuum Induction Melted 1775 F (968 C) Solution Heat Treated, Precipitation-Hardenable*, jun 2009.

[372] D. F. Paulonis and J. J. Schirra, "Alloy 718 at Pratt & Whitney: Historical Perspective and Future Challenges," in *Superalloys 718, 625, 706 and Various Derivatives (2001)*, 2001, pp. 13–23.

[373] R. Schafrik, D. Ward, and J. Groh, "Application of Alloy 718 in GE Aircraft Engines: Past, Present and Next Five Years," in *Superalloys 718, 625, 706 and Various Derivatives (2001)*, 2001, pp. 1–11.

[374] J. F. Radavich, "The Physical Metallurgy of Cast and Wrought Alloy 718," in *Superalloys 718 Metallurgy and Applications (1989)*, 1989, pp. 229–240.

[375] G. D. Janaki Ram, A. Venugopal Reddy, K. Prasad Rao, G. M. Reddy, and J. K. Sarin Sundar, "Microstructure and tensile properties of Inconel 718 pulsed Nd-YAG laser welds," *Journal of Materials Processing Technology*, vol. 167, no. 1, pp. 73–82, aug 2005.

[376] J. Lambarri, J. Leunda, V. García Navas, C. Soriano, and C. Sanz, "Microstructural and tensile characterization of Inconel 718 laser coatings for aeronautic components," *Optics and Lasers in Engineering*, vol. 51, no. 7, pp. 813–821, jul 2013.

[377] P. L. Blackwell, "The mechanical and microstructural characteristics of laser-deposited IN718," *Journal of Materials Processing Technology*, vol. 170, no. 1-2, pp. 240–246, dec 2005.

[378] M. Bambach and I. Sizova, "Hot working behavior of selective laser melted and laser metal deposited Inconel 718," in *AIP Conference Proceedings*, vol. 1960, no. 1. American Institute of Physics Inc., may 2018, p. 170001.

[379] Y. Zhang, L. Yang, T. Chen, W. Zhang, X. Huang, and J. Dai, "Investigation on the optimized heat treatment procedure for laser fabricated IN718 alloy," *Optics and Laser Technology*, vol. 97, pp. 172–179, dec 2017.

[380] X. You, Y. Tan, S. Shi, J. M. Yang, Y. Wang, J. Li, and Q. You, "Effect of solution heat treatment on the precipitation behavior and strengthening mechanisms of electron beam smelted Inconel 718 superalloy," *Materials Science and Engineering A*, vol. 689, pp. 257–268, mar 2017.

[381] E. Hosseini and V. A. Popovich, "A review of mechanical properties of additively manufactured Inconel 718," p. 100877, dec 2019.

[382] F. Lia, J. Z. Park, J. S. Keist, S. Joshi, and R. P. Martukanitz, "Thermal and microstructural analysis of laser-based directed energy deposition for Ti-6Al-4V and Inconel 625 deposits," *Materials Science and Engineering A*, vol. 717, pp. 1–10, feb 2018.

[383] G. P. Dinda, A. K. Dasgupta, and J. Mazumder, "Laser aided direct metal deposition of Inconel 625 superalloy: Microstructural evolution and thermal stability," *Materials Science and Engineering A*, vol. 509, no. 1-2, pp. 98–104, may 2009.

[384] Y. L. Hu, X. Lin, S. Y. Zhang, Y. M. Jiang, X. F. Lu, H. O. Yang, and W. D. Huang, "Effect of solution heat treatment on the microstructure and mechanical properties of Inconel 625 superalloy fabricated by laser solid forming," *Journal of Alloys and Compounds*, vol. 767, pp. 330–344, oct 2018.

[385] Y. L. Hu, X. Lin, X. B. Yu, J. J. Xu, M. Lei, and W. D. Huang, "Effect of Ti addition on cracking and microhardness of Inconel 625 during the laser solid forming processing," *Journal of Alloys and Compounds*, vol. 711, pp. 267–277, jul 2017.

[386] M. Rombouts, G. Maes, M. Mertens, and W. Hendrix, "Laser metal deposition of Inconel 625: Microstructure and mechanical properties," *Journal of Laser Applications*, vol. 24, no. 5, p. 052007, nov 2012.

[387] F. J. Xu, Y. H. Lv, B. S. Xu, Y. X. Liu, F. Y. Shu, and P. He, "Effect of deposition strategy on the microstructure and mechanical properties of Inconel 625 superalloy fabricated by pulsed plasma arc deposition," *Materials and Design*, vol. 45, pp. 446–455, mar 2013.

[388] A. Aversa, A. Saboori, E. Librera, M. de Chirico, S. Biamino, M. Lombardi, and P. Fino, "The role of Directed Energy Deposition atmosphere mode on the microstructure and mechanical properties of 316L samples," *Additive Manufacturing*, vol. 34, no. February, p. 101274, 2020.

[389] K. Benarji, Y. Ravi Kumar, A. N. Jinoop, C. P. Paul, and K. S. Bindra, "Effect of Heat-Treatment on the Microstructure, Mechanical Properties and Corrosion Behaviour of SS 316 Structures Built by Laser Directed Energy Deposition Based Additive Manufacturing," *Metals and Materials International*, vol. 27, no. 3, pp. 488–499, 2021.

[390] K. Saeidi, X. Gao, Y. Zhong, and Z. J. Shen, "Hardened austenite steel with columnar sub-grain structure formed by laser melting," *Materials Science and Engineering A*, vol. 625, pp. 221–229, feb 2015.

[391] A. Yadollahi, N. Shamsaei, S. M. Thompson, and D. W. Seely, "Effects of process time interval and heat treatment on the mechanical and microstructural properties of direct laser deposited 316L stainless steel," *Materials Science and Engineering A*, vol. 644, pp. 171–183, sep 2015.

[392] D.-R. Eo, S.-H. Park, and J.-W. Cho, "Inclusion evolution in additive manufactured 316L stainless steel by laser metal deposition process," *Materials & Design*, vol. 155, pp. 212–219, 2018.

[393] K. Saeidi, X. Gao, F. Lofaj, L. Kvetková, and Z. J. Shen, "Transformation of austenite to duplex austenite-ferrite assembly in annealed stainless steel 316L consolidated by laser melting," *Journal of Alloys and Compounds*, vol. 633, pp. 463–469, jun 2015.

[394] M. Ziętala, T. Durejko, M. Polański, I. Kunce, T. Płociński, W. Zieliński, M. Łazińska, W. Stępniowski, T. Czujko, K. J. Kurzydłowski, and Z. Bojar, "The microstructure, mechanical properties and corrosion resistance of 316 L stainless steel fabricated using laser engineered net shaping," *Materials Science and Engineering A*, vol. 677, pp. 1–10, nov 2016.

[395] X. Chen, J. Li, X. Cheng, H. Wang, and Z. Huang, "Effect of heat treatment on microstructure, mechanical and corrosion properties of austenitic stainless steel 316L using arc additive manufacturing," *Materials Science and Engineering A*, vol. 715, pp. 307–314, feb 2018.

[396] C. Wang, X. Tan, E. Liu, and S. B. Tor, "Process parameter optimization and mechanical properties for additively manufactured stainless steel 316L parts by selective electron beam melting," *Materials and Design*, vol. 147, pp. 157–166, jun 2018.

[397] T. P. Gill, V. Shankar, M. G. Pujar, and P. Rodriguez, "Effect of composition on the transformation of δ-ferrite TO σ in type 316 stainless steel weld metals," *Scripta Metallurgica et Materiala*, vol. 32, no. 10, pp. 1595–1600, may 1995.

[398] M. Schwind, J. Källqvist, J. O. Nilsson, J. Ågren, and H. O. Andrén, "σ-phase precipitation in stabilized austenitic stainless steels," *Acta Materialia*, vol. 48, no. 10, pp. 2473–2481, jun 2000.

[399] R. A. Lula, *Stainless steel*, 1985.

[400] "ASTM A564 / A564M - 19A, Standard Specification for Hot-Rolled and Cold-Finished Age-Hardening Stainless Steel Bars and Shapes," West Conshohocken, PA, 2019. [Online]. Available: https://www.astm.org/Standards/A564.htm

[401] H. Nakagawa and T. Miyazaki, "Effect of retained austenite on the microstructure and mechanical properties of martensitic precipitation hardening stainless steel," *Journal of Materials Science*, vol. 34, no. 16, pp. 3901–3908, 1999.

[402] T. LeBrun, T. Nakamoto, K. Horikawa, and H. Kobayashi, "Effect of retained austenite on subsequent thermal processing and resultant mechanical properties of selective laser melted 17-4 PH stainless steel," *Materials and Design*, vol. 81, pp. 44–53, sep 2015.

[403] C. N. Hsiao, C. S. Chiou, and J. R. Yang, "Aging reactions in a 17-4 PH stainless steel," *Materials Chemistry and Physics*, vol. 74, no. 2, pp. 134–142, mar 2002.

[404] M. Murayama, Y. Katayama, and K. Hono, "Microstructural evolution in a 17-4 PH stainless steel after aging at 400 C," *Metallurgical and Materials Transactions A: Physical Metallurgy and Materials Science*, vol. 30, no. 2, pp. 345–353, 1999.

[405] K. C. Hsu and C. K. Lin, "High-temperature fatigue crack growth behavior of 17-4 PH stainless steels," *Metallurgical and Materials Transactions A: Physical Metallurgy and Materials Science*, vol. 35 A, no. 9, pp. 3018–3024, 2004.

[406] C. F. Arisoy, G. Basman, and M. K. Sesen, "Failure of a 17-4 PH stainless steel sailboat propeller shaft," *Engineering Failure Analysis*, vol. 10, no. 6, pp. 711–717, dec 2003.

[407] J. Wang, H. Zou, C. Li, R. Zuo, S. Qiu, and B. Shen, "Relationship of microstructure transformation and hardening behavior of type 17-4 PH stainless steel," *Journal of University of Science and Technology Beijing: Mineral Metallurgy Materials (Eng Ed)*, vol. 13, no. 3, pp. 235–239, jun 2006.

[408] Y. Sun, R. J. Hebert, and M. Aindow, "Effect of heat treatments on microstructural evolution of additively manufactured and wrought 17-4PH stainless steel," *Materials and Design*, vol. 156, pp. 429–440, oct 2018.

[409] D. Wang, C. T. Chi, W. Q. Wang, Y. L. Li, M. S. Wang, X. G. Chen, Z. H. Chen, X. P. Cheng, and Y. J. Xie, "The effects of fabrication atmosphere condition on the microstructural and mechanical properties of laser direct manufactured stainless steel 17-4 PH," *Journal of Materials Science and Technology*, vol. 35, no. 7, pp. 1315–1322, jul 2019.

[410] S. Takaki, K. Fukunaga, J. Syarif, and T. Tsuchiyama, "Effect of Grain Refinement on Thermal Stability of Metastable Austenitic Steel," *MATERIALS TRANSACTIONS*, vol. 45, no. 7, pp. 2245–2251, 2004.

[411] J. Wang, H. Zou, C. Li, S. yu Qiu, and B. luo Shen, "The effect of microstructural evolution on hardening behavior of type 17-4PH stainless steel in long-term aging at 350 C," *Materials Characterization*, vol. 57, no. 4-5, pp. 274–280, dec 2006.

[412] ASM Handbook Committee, *ASM Handbook Volume 2: Properties and Selection: Nonferrous Alloys and Special-Purpose Materials*. ASM International, dec 1990, vol. 2.

[413] E. Sjölander and S. Seifeddine, “The heat treatment of Al-Si-Cu-Mg casting alloys,” pp. 1249–1259, jul 2010.

[414] ——, “Artificial ageing of Al-Si-Cu-Mg casting alloys,” *Materials Science and Engineering A*, vol. 528, no. 24, pp. 7402–7409, sep 2011.

[415] F. Alghamdi and M. Haghshenas, “Microstructural and small-scale characterization of additive manufactured AlSi10Mg alloy,” *SN Applied Sciences*, vol. 1, no. 3, p. 255, 2019.

[416] M. E. Glicksman, *Principles of solidification: An introduction to modern casting and crystal growth concepts*. Springer New York, 2011.

[417] “ASTM F75-18, Standard Specification for Cobalt-28 Chromium-6 Molybdenum Alloy Castings and Casting Alloy for Surgical Implants (UNS R30075),” West Conshohocken, PA, 2018. [Online]. Available: http://www.astm.org/cgi-bin/resolver.cgi?F75-18

[418] T. Kilner, R. M. Pilliar, G. C. Weatherly, and C. Allibert, “Phase identification and incipient melting in a cast Co-Cr surgical implant alloy,” *Journal of Biomedical Materials Research*, vol. 16, no. 1, pp. 63–79, jan 1982.

[419] S. Mineta, S. Namba, T. Yoneda, K. Ueda, and T. Narushima, “Carbide formation and dissolution in biomedical CO-CR-MO alloys with different carbon contents during solution treatment,” *Metallurgical and Materials Transactions A: Physical Metallurgy and Materials Science*, vol. 41, no. 8, pp. 2129–2138, aug 2010.

[420] H. S. Dobbs and J. L. Robertson, “Heat treatment of cast Co-Cr-Mo for orthopaedic implant use,” *Journal of Materials Science*, vol. 18, no. 2, pp. 391–401, feb 1983.

[421] J. Cohen, R. M. Rose, and J. Wulff, “Recommended heat treatment and alloy additions for cast Co-Cr surgical implants,” *Journal of Biomedical Materials Research*, vol. 12, no. 6, pp. 935–937, nov 1978.

[422] M. Caudillo, M. Herrera-Trejo, M. R. Castro, E. Ramírez, C. R. González, and J. I. Juárez, “On carbide dissolution in an as-cast ASTM F-75 alloy,” *Journal of Biomedical Materials Research*, vol. 59, no. 2, pp. 378–385, feb 2002.

[423] M. Herrera, A. Espinoza, J. Méndez, M. Castro, J. López, and J. Rendón, “Effect of C content on the mechanical properties of solution treated as-cast ASTM F-75 alloys,” *Journal of Materials Science: Materials in Medicine*, vol. 16, no. 7, pp. 607–611, jul 2005.

[424] H. R. Lashgari, S. Zangeneh, and M. Ketabchi, “Isothermal aging effect on the microstructure and dry sliding wear behavior of Co-28Cr-5Mo-0.3C alloy,” *Journal of Materials Science*, vol. 46, no. 22, pp. 7262–7274, nov 2011.

[425] M. K. Mallik, C. S. Rao, and V. V. Kesava Rao, “Effect of heat treatment on hardness of Co-Cr-Mo alloy deposited with laser engineered net shaping,” in *Procedia Engineering*, vol. 97. Elsevier Ltd, jan 2014, pp. 1718–1723.

[426] F. A. España, V. K. Balla, S. Bose, and A. Bandyopadhyay, “Design and fabrication of CoCrMo alloy based novel structures for load bearing implants using laser engineered net shaping,” *Materials Science and Engineering C*, vol. 30, no. 1, pp. 50–57, jan 2010.

[427] M. Mantrala, C. Rao, and V. Rao, “Influence of heat Treatment on Tensile Properties of LENS Deposited Co-Cr-Mo alloy,” in *6th International & 27th All India Manufacturing Technology, Design and Research Conference (AIMTDR-2016)*, 2016, pp. 52–54.

[428] C. Dharmendra, A. Hadadzadeh, B. S. Amirkhiz, and M. Mohammadi, “The Morphology, Crystallography, and Chemistry of Phases in Wire-Arc Additively Manufactured Nickel Aluminum Bronze,” in *Minerals, Metals and Materials Series*. Springer International Publishing, 2019, pp. 443–453.

[429] C. Dharmendra, A. Hadadzadeh, B. S. Amirkhiz, G. D. Janaki Ram, and M. Mohammadi, “Microstructural evolution and mechanical behavior of nickel aluminum bronze Cu-9Al-4Fe-4Ni-1Mn fabricated through wire-arc additive manufacturing,” *Additive Manufacturing*, vol. 30, p. 100872, dec 2019.

[430] C. Shen, G. Mu, X. Hua, F. Li, D. Luo, X. Ji, and C. Zhang, “Influences of postproduction heat treatments on the material anisotropy of nickel-aluminum bronze fabricated using wire-arc additive manufacturing process,” *International Journal of Advanced Manufacturing Technology*, vol. 103, no. 5-8, pp. 3199–3209, aug 2019.

[431] W. Jeong, Y. S. Kwon, and D. Kim, “Three-dimensional printing of tungsten structures by directed energy deposition,” *Materials and Manufacturing Processes*, vol. 34, no. 9, pp. 986–992, jul 2019.

[432] C. Li, S. Ma, X. Liu, J. Li, and G. Le, “Microstructures and properties of 80W-20Fe alloys prepared using laser melting deposition process,” *International Journal of Refractory Metals and Hard Materials*, vol. 77, pp. 113–119, dec 2018.

[433] D. Stewart, “3D printing growth accelerates again.” [Online]. Available: https://www2.deloitte.com/us/en/insights/industry/technology/technology-media-and-telecom-predictions/3d-printing-market.html

[434] N. Li, S. Huang, G. Zhang, R. Qin, W. Liu, H. Xiong, G. Shi, and J. Blackburn, “Progress in additive manufacturing on new materials: A review,” pp. 242–269, feb 2019.

[435] M. A. Easton, M. Qian, A. Prasad, and D. H. StJohn, “Recent advances in grain refinement of light metals and alloys,” *Current Opinion in Solid State and Materials Science*, vol. 20, no. 1, pp. 13–24, feb 2016.

[436] M. J. Bermingham, D. Kent, H. Zhan, D. H. Stjohn, and M. S. Dargusch, “Controlling the microstructure and properties of wire arc additive manufactured Ti-6Al-4V with trace boron additions,” *Acta Materialia*, vol. 91, pp. 289–303, jun 2015.

[437] S. Mereddy, M. J. Bermingham, D. Kent, A. Dehghan-Manshadi, D. H. StJohn, and M. S. Dargusch, “Trace Carbon Addition to Refine Microstructure and Enhance Properties of Additive-Manufactured Ti-6Al-4V,” *JOM*, vol. 70, no. 9, pp. 1670–1676, sep 2018.

[438] N. T. Aboulkhair, I. Maskery, C. Tuck, I. Ashcroft, and N. M. Everitt, “The microstructure and mechanical properties of selectively laser melted AlSi10Mg: The effect of a conventional T6-like heat treatment,” *Materials Science and Engineering A*, vol. 667, pp. 139–146, jun 2016.